6-27-2022

Study of the Etaprimepi0 System in GlueX

Rupesh Dotel
Florida International University, rdote001@fiu.edu

FLORIDA INTERNATIONAL UNIVERSITY

Miami, Florida

STUDY OF THE $\eta'\pi^0$ SYSTEM IN GLUEX

A dissertation submitted in partial fulfillment of the

requirements for the degree of

DOCTOR OF PHILOSOPHY

in

PHYSICS

by

Rupesh Dotel

2022

To: Dean Michael R. Heithaus
College of Arts, Science and Education

This dissertation, written by Rupesh Dotel, and entitled Study of the $\eta'\pi^0$ System in GlueX, having been approved in respect to style and intellectual content, is referred to you for judgment.

We have read this dissertation and recommend that it be approved.

Joerg Reinhold

Lei Guo

Christopher Dares

Werner Boeglin, Major Professor

Date of Defense: June 27, 2022

The dissertation of Rupesh Dotel is approved.

Dean Michael R. Heithaus
College of Arts, Science and Education

Andrés G. Gil
Vice President for Research and Economic Development
and Dean of the University Graduate School

Florida International University, 2022

DEDICATION

To my parents D.P. Dotel and Rena Dotel

ACKNOWLEDGMENTS

This work wouldn't have been possible without the effort and guidance of my advisor Werner Boeglin. I am deeply thankful to him for motivating and encouraging me to be critical to my own work and helping me to think like a scientist. I would also like to thank my committee members, Joerg Reinhold, Lei Guo and Christopher Dares for being a part of this project and helping me throughout my journey.

I owe special thanks to Mariana Khachatryan for helping me particularly in the partial wave analysis of my project. I would also like to thank my FIU friend Mahmoud Kamel for helping me in the calibration effort of the Start Counter detector.

I would like to express my gratitude to Dave Mack, particularly, for helping me to identify sources of background in my channel. My project was a collaborative effort and hence I am very thankful to GlueX members, particularly, Beni Zihlmann, Sean Dobbs, Alex Austregesilo, Justin Stevens, Colin Gleason, Shankar Adhikari and Tolga Erbora for helping me to understand the physics and the working of the detectors.

PhD is a difficult journey and support from family and friends is equally important. My appreciation goes to my sister Rakshya Bhattarai, without whom I wouldn't have been able to start the journey of graduate school in the U.S.A. I am forever grateful to my wife Manuja Ghimire and my lovely daughter Izna Dotel for being an important part of my life and providing me emotional support at all times.

ABSTRACT OF THE DISSERTATION

STUDY OF THE $\eta'\pi^0$ SYSTEM IN GLUEX

by

Rupesh Dotel

Florida International University, 2022

Miami, Florida

Professor Werner Boeglin, Major Professor

The $\eta'\pi$ is an important decay channel for the potentially exotic hybrid meson $\pi_1(1600)$ that has been detected in the COMPASS, VES and E852 experiments. These previous experiments used a charged pion beam as a probe. In contrast, the GlueX experiment is designed to search for the exotic hybrid mesons using a linearly polarized photon beam. This thesis project analyzes the $\eta'\pi^0$ system produced in GlueX by the reaction $\gamma p \to \eta'\pi^0 p$. After optimizing the event selection to minimize background contributions, a mass independent partial wave analysis is performed in search of an exotic signature. Within the currently available statistical precision, no signal was found.

TABLE OF CONTENTS

CHAPTER PAGE

LIST OF FIGURES

CHAPTER 1

INTRODUCTION

1.1 Outline

In the standard model of particle physics, elementary particles are divided into either spin-half fermions or integer-spin bosons. The fermions are further divided into quarks and leptons based on their types of interaction. The quarks interact through the strong force while leptons interact via the electromagentic or weak forces. Quantum Chromodynamics is the theory of strong interaction that describes the interaction of quark systems through the exchange of gauge bosons called gluons.

In the constituent quark model, each meson is described as a bound state of a quark-antiquark $q\bar{q}$ pair. Quarks within a meson interact through the exchange of gluons. A current (naked) gluon is a massless and chargeless gauge boson with spin $J = 1$. Gluons in a $q\bar{q}$ state have been modeled as bags [1] and flux-tubes ([2], [3]). Ordinarily gluonic fields within a meson can be thought of as in a ground state, for example in a pion. Such an observable meson has to be colourless. However, the gluonic field may be contributing fundamentally differently to the $q\bar{q}$ pair system other than in the case of an ordinary meson eg: a pion. We will refer to such mesons as hybrid mesons in which gluonic field manifestation is pronounced. In a hybrid meson the $q\bar{q}$ is most likely colored and only in combination with a colored gluon, a colorless $q\bar{q}g$ state is possible. Here g refers to the gluons. Gluons in a $q\bar{q}g$ have been named as "excited" gluons although one should not understand them in the same sense as we understand an atomic excitation. Light mesonic states can be quite broad and a hybrid meson can therefore overlap with a regular meson making it difficult to identify experimentally. A special type of hybrid, however, is of particular significance because the constituent gluons can contribute to the quantum

number of the mesonic system giving rise to a quantum number not allowed in a regular $q\bar{q}$ pair. Such a quantum number is called an exotic quantum number and the corresponding meson is called an exotic hybrid meson. A light exotic hybrid meson candidate called $\pi_1(1600)$ has been observed previously in pion scattering experiments. Three different experiments E852 [4] in 2001, VES [5] in 2005 and COMPASS [6] in 2015 reported evidence of the $\pi_1(1600)$. E852 used an 18 GeV/c π^- beam to study the reaction $\pi^- p \to \eta'\pi^- p$. VES used a 43 GeV/c π^- beam and studied the reaction $\pi^- p \to \eta'\pi^0 n$ while COMPASS used a much higher energy 190 GeV/c π^- beam to study the $\pi^- p \to \eta'\pi^- p$ reaction. A partial wave analysis of the $\eta'\pi$ system in these studies showed similar evidence of an exotic signal. This analysis focuses on the search for the $\pi_1(1600)$ signal in photoproduction in the GlueX experiment. We will study the photoproduction reaction $\gamma p \to \eta'\pi^0 p$ to search for the $\pi_1(1600)$ exotic hybrid meson.

An outline of this thesis is as follows. Chapter 1 describes the conventional mesons, exotic mesons, motivation, and a discussion of the reference frames used in this analysis. Chapter 2 describes the details of the instrumentation. Event selection and background handling is described in chapter 3. Chapter 4 contains the details of the fitting procedure and the partial wave analysis results. Chapter 5 provides a summary and a conclusion of this thesis.

1.2 Spin J, Parity P and Charge Conjugation C In Mesons

Consider the total wavefunction of a system as a combination of the radial, angular and the spin wavefunctions as

$$\Psi(\vec{r},\vec{s}) = R(r)Y_{LM}(\theta,\phi)\chi(\vec{s}) \tag{1.1}$$

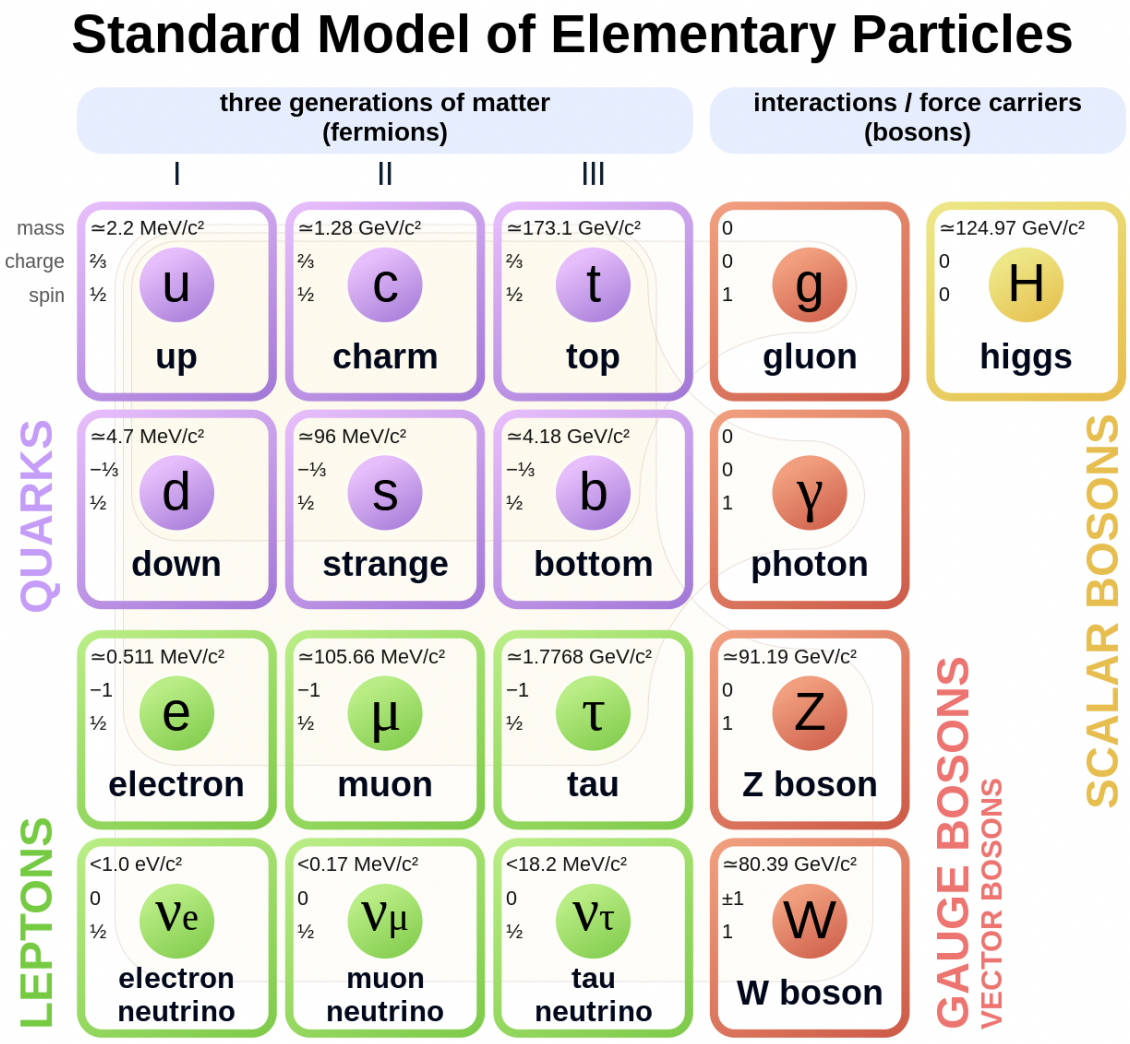

Fig. 1.1. Elementary particles in standard model. Source [7]

The total angular momentum of a combination of quarks is given by

$$\vec{J} = \vec{L} + \vec{S} \tag{1.2}$$

where $\vec{S}$ is the total spin of the individual quarks and $\vec{L}$ is the relative angular momentum of the system. The Parity (P) operator inverts the sign of all the spatial co-ordinates. It's eigenvalue is ± 1. For a quark-antiquark ($q\overline{q}$) pair, Parity is defined as

$$P = (-1)^{L+1} \tag{1.3}$$

The additional factor (-1) us because q and $\overline{q}$ have the opposite intrinsic parities and $(-1)^L$ is due to the spatial inversion

$$Y_{LM}(\pi - \theta, \pi + \phi) = (-1)^L Y_{LM}(\theta, \phi) \tag{1.4}$$

in the $Y_{LM}(\theta, \phi)$ of the $q\overline{q}$ wavefunction.

Charge conjugation (C) is an operator that transforms a particle into it's antiparticle by changing the sign of the charge and magnetic moment of a particle. Charge conjugation eigenvalue for a system of a ($q\overline{q}$) pair is defined as

$$C = (-1)^{L+S} \tag{1.5}$$

The $(-1)^L$ contribution is again from the spatial inversion in the angular dependence of the $q\overline{q}$ wavefunction. The interchange of the q and $\overline{q}$ leads to an additional contribution of (-1) and a factor of $(-1)^{S+1}$ is due to the inversion of the spin wavefunctions $\chi(\vec{s})$ for a system of two fermions.

Therefore in the constituent quark model each meson can be assigned a unique J^{PC} quantum number.

S/L	$L=0$	$L=1$	$L=2$
$S=0$	0^{-+}	1^{+-}	2^{+-}
$S=1$	1^{--}	0^{++}, 1^{++}, 2^{++}	1^{--}, 2^{--}, 3^{--}

Table 1.1. First few allowed J^{PC} quantum numbers for a meson in constituent quark model

1.3 Exotic Quantum Numbers

The table 1.1 shows a list of the first few J^{PC} quantum numbers allowed by the equations 1.2, 1.3, 1.5 for a $q\overline{q}$ pair. Some of the states that are missing are 0^{--}, 0^{+-}, 1^{-+}, 2^{+-}, 3^{-+}, ... These states are referred to as states with exotic quantum numbers. Existence of these missing states for a meson implies a contribution to the quantum number outside of a pure $q\overline{q}$ pair. The quantum number 1^{-+} is of particular significance since several past experiments have shown promising results for this particular state.

A $J^{PC} = 1^{-+}$ state can't be a pure $q\overline{q}$ state and the existence of such a state would confirm a system outside of a $q\overline{q}$ pair or an exotic state.

The study of a system of two pseudoscalar mesons such as $\eta\pi$ or $\eta'\pi$ would be a favorable decay channel for a 1^{-+} system because their total spin $\vec{S}$ being 0, an $\vec{L} = 1$ state would violate the set of equations 1.2, 1.3 and 1.5 indicating a contribution to the J^{PC} of the system from outside of a $q\overline{q}$ pair.

1.4 Previous Experimental Observations of the $J^{PC} = 1^{-+}$ Quantum Number Decaying into the $\eta'\pi$ Channel

Three different experiments conducted in the past have reported a P-wave ($\vec{L} = 1$) signal in the $\eta'\pi$ decay channel. The P-wave intensities from the experiments E852 [4] in 2001, VES [5] in 2005 and COMPASS [6] in 2015 are shown in figures 1.2, 1.3 and 1.4 respectively. E852 used an 18 GeV/c π^- beam to study the reaction $\pi^- p \to \eta'\pi^- p$. VES used 43 GeV/c π^- beam and studied the reaction $\pi^- p \to \eta'\pi^0 n$ while COMPASS used much higher energy 190 GeV/c π^- beam to study the $\pi^- p \to \eta'\pi^- p$ reaction. A wide signal is observed in all 3 reactions in P-wave at around 1600 MeV. In COMPASS (figure 1.4), it is also observed that the $\eta'\pi^-$ intensity is orders of magnitude higher than the $\eta\pi^-$ intensity. However all of these experiments used a negatively charged pion (π^-) beam. The photoproduction of the $\pi_1(1600)$ 1^{-+} state remains largely unexplored to date.

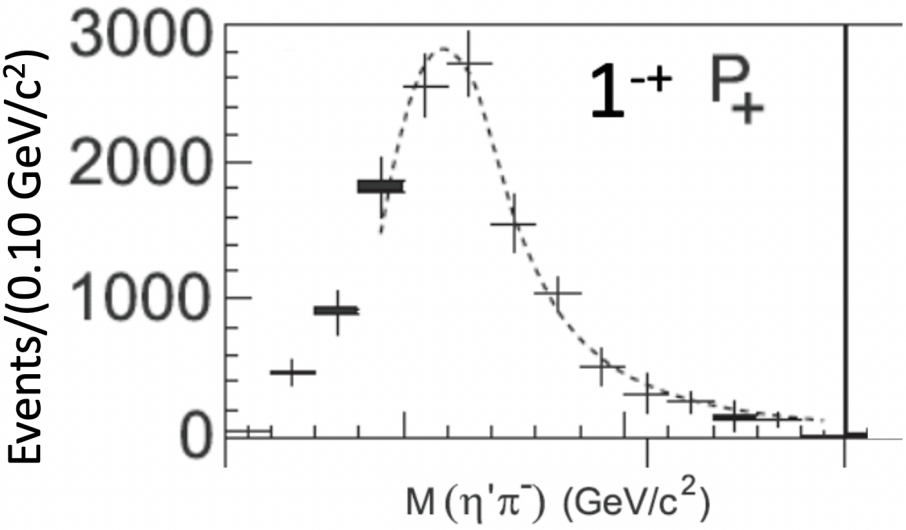

Fig. 1.2. P-wave intensity for $\eta'\pi$ invariant mass from E852 experiment. [4]

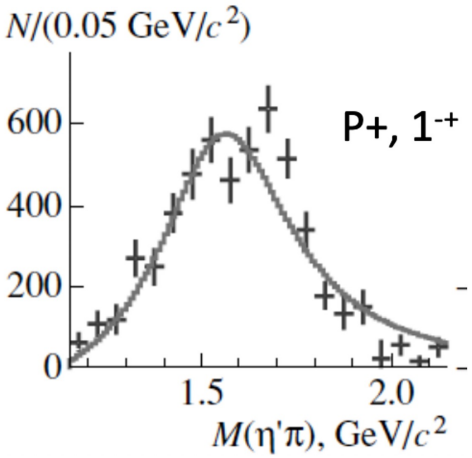

Fig. 1.3. P-wave intensity for $\eta'\pi$ invariant mass from VES experiment. [5]

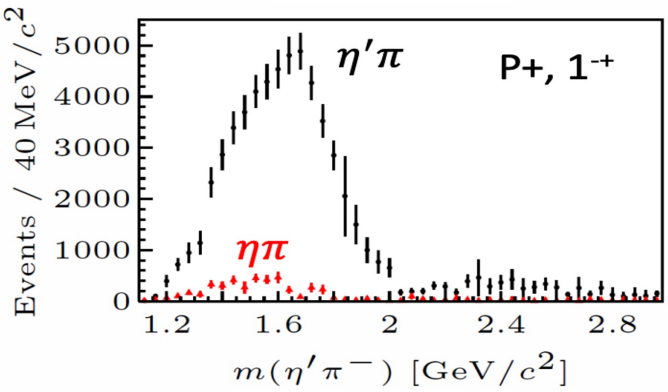

Fig. 1.4. P-wave intensity for $\eta'\pi$ invariant mass from COMPASS (black data points). The red data points belong to the $\eta\pi$ system. The $\eta'\pi$ intensity is more than 5 times stronger than the $\eta\pi$ system in the peak region (1600 MeV). [6]

1.5 Photoproduction Of An Exotic Meson

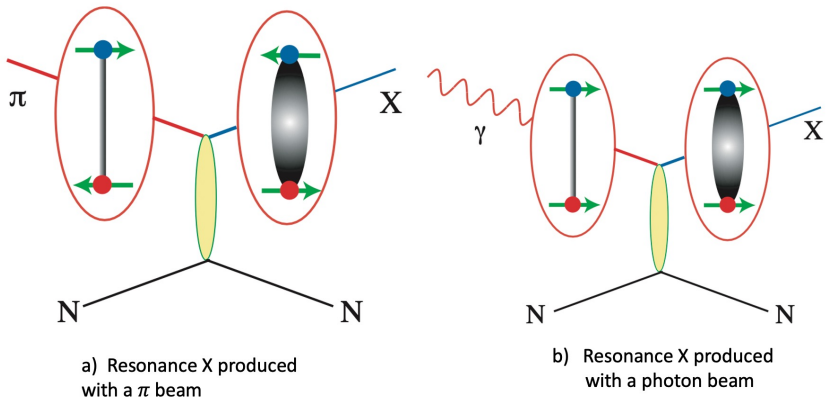

Fig. 1.5. Prediction of behaviour of two different beams on nuclear target. Pion-probe (left) vs photon-probe (right). The photon-probe has spin 1 and might be more likely to produce an exotic with spin 1. Image source [8]

There are theoretical predictions that a photon beam is more likely to produce an exotic quantum number than a pion beam [8]. Figure 1.5 shows a comparison of the two different methods of production of a resonance X. Gluons have been modeled as flux tubes [9] that are in their ground state in conventional mesons. In this picture, the $(q\overline{q})$ is held together by a cylindrical tube of color flux, and the binding energy is proportional to the tube length. An exotic meson can be pictured as an ordinary meson but with an excitation of the gluonic flux tube. Since the spins of the two quarks of a pion beam (left, fig. 1.5) are anti-aligned, the spins have to be aligned followed by an excitation of a flux tube to produce an exotic meson. This method is more likely to produce a hybrid without an exotic quantum number. A photon beam (right, fig. 1.5) can be thought of as a virtual $q\overline{q}$ pair with spins already aligned to produce a net spin $S = 1$. So only an excitation of the flux tube is sufficient to produce an exotic quantum number.

1.6 The Photoproduction Reaction And The Decay Channels

In the GlueX experiment, a 12 GeV electron beam is incident on a diamond radiator. A linearly polarized photon beam in an energy range of 4-12 GeV is produced through coherent Bremsstrahlung. The photon beam has a coherent peak, an enhancement in intensity at an energy at around 9 GeV and it interacts with a liquid hydrogen target at the center of the GlueX detector. At this energy range, a t-channel exchange process as shown in fig. 1.6 is predicted to be the dominating reaction process.

In a t-channel process, the beam interacts with the target via some exchange particle E_x producing a resonance X in the upper vertex and a recoil proton in the lower vertex. The resonance then decays into a π^0 and an η'. The dominant decay mode of $\pi^0 \to \gamma\gamma$ with a branching fraction of 98.8% is chosen for study [10]. The three different decay modes $\eta' \to \pi^+\pi^-\eta$, $\eta' \to \rho^0\gamma$ and $\eta' \to \pi^0\pi^0\eta$ have the branching fractions 42.5%, 29.5% and 22.4% respectively [10]. For the η', the channel $\eta' \to \pi^+\pi^-\eta$ is chosen. The $\pi^+\pi^-\eta$ decay mode is chosen against the $\rho^0\gamma$ decay mode, although it involves an η which again decays to $\gamma\gamma$ with a branching fraction of 72.1% [10], because the $\rho^0\gamma$ decay mode has a single photon in the final state which is difficult to identify. For example, a missing photon from a π^0 decay to $\gamma\gamma$ can easily be misidentified as a bachelor photon.

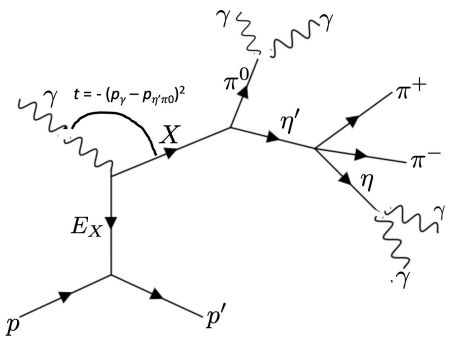

Fig. 1.6. Feynman diagram for the reaction of interest. The photon beam interacting with a proton target through a t-channel exchange. A resonance X is produced in the upper vertex which decays to an η' and a π^0. The η' decays to $\pi^+\pi^-\eta$, and η decays to $\gamma\gamma$, and the π^0 decays to $\gamma\gamma$

1.7 Reaction Kinematics: Helicity And Gottfried-Jackson Frames

To extract the spin of the $\eta'\pi^0$ system, it is convenient to study the decay of the resonance X in a particular reference frame. The left diagram in fig. 1.8 is the helicity frame. First we boost from the lab frame to the center of mass frame of the $\eta'\pi^0$ system. The z-axis is defined as opposite to the recoil proton momentum. The y-axis is chosen as a cross product of the direction of the beam and the z-axis. The x-axis is orthogonal to the yz plane given by the right hand rule. i.e

$$\hat{z} = \frac{-\vec{p}_{recoil}}{|-p_{recoil}|} \qquad \hat{y} = \frac{\vec{p}_{beam} \times \hat{z}}{|\vec{p}_{beam} \times \hat{z}|} \qquad \hat{x} = \hat{y} \times \hat{z} \tag{1.6}$$

In the right diagram the xz plane is rotated by some angle such that the beam direction and z-axis are the same. This frame is called the Gottfried-Jackson frame. The reason behind using these frames is that in the rest frame of the $\eta'\pi^0$ system, the angular distribution of the decay product η' contains the information of the

spin of the $\eta'\pi^0$ system. Since the total spin $\vec{J}$ is conserved, it reflects on the decay angles of the products. To be more specific, in an ideal case, the cosine of the polar angle in the Gottfried-Jackson frame will show symmetries for different quantum mechanical waves (S,P,D, ..) corresponding to the spins (L = 0,1,2,..) for the $\eta'\pi^0$ system as shown in fig. 1.7.

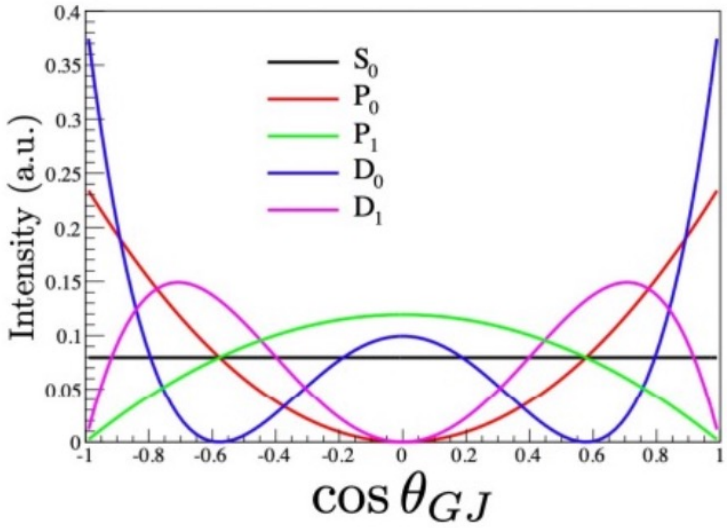

Fig. 1.7. A figure of the symmetries reflected in the $cos\theta_{GJ}$ variable for different quantum mechanical waves. Image source [11]

In the figure 1.8, the $\vec{\epsilon'}$ is the electric field vector of the photon beam, also called the polarization vector and the angle Φ is the angle between polarization plane and the production plane. The angle Φ provides an additional constraint to study the production and the decay mechanisms.

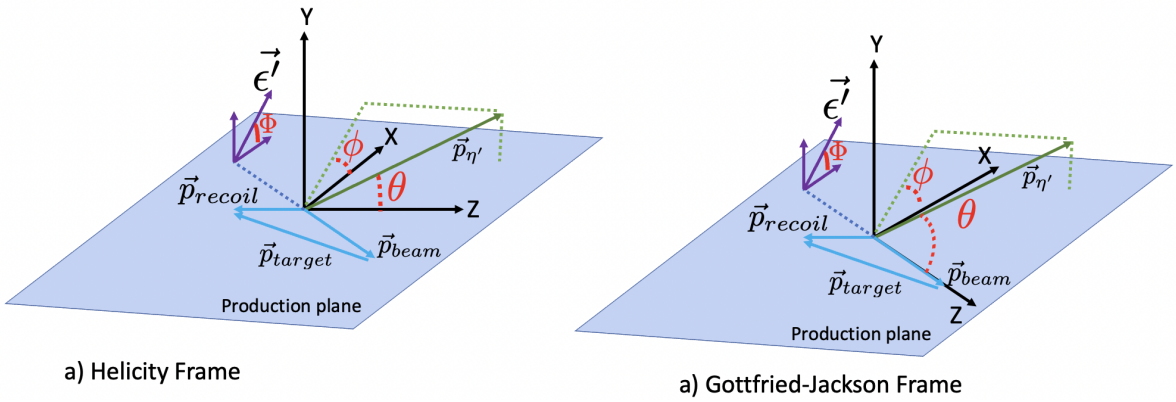

Fig. 1.8. Helicity (left) and Gottfried-Jackson (right) frames to study the decay of $\eta'\pi^0$ system. The θ and ϕ represent the polar and azimuthal angles of the decay η' in the $\eta'\pi^0$ rest frame. In Helicity frame the z-axis is opposite to the recoil proton and in Gottfried-Jackson frame the z-axis is in the direction of the beam. The Φ is the angle between the polarization plane and the production plane.

1.8 Partial Wave Analysis

One way of identifying a resonance is by studying the invariant mass distribution. However a peak in an invariant mass distribution might not always correspond to a resonance. It could be an artifact of the acceptance effect. One might also see a peak in the invariant mass distribution corresponding to a resonance but determining it's J^{PC} quantum numbers requires a partial wave analysis. A partial wave analysis determines the production amplitudes by fitting the decay angular distributions. The fit requires a model to the total intensity which is parameterized in terms of the polarization of the beam and the target, spin and parity of the resonance and their decay products and most importantly the relative angular momenta between the decay products. Hence a detail study of the nature of a possible resonance and identifying the J^{PC} quantum number can be achieved by a partial wave analysis.

In this analysis, we study the $\eta'\pi^0$ system in GlueX. We will analyze the background from different alternate channels in detail. Then we explore two different methods of signal to background separation which will be described in chapter 3. Finally we perform a partial wave analysis of the extracted signal angular distributions using the extended maximum likelihood method which is described in chapter 4.

Bibliography

[1] Ted Barnes and Frank E Close. A light exotic qqg hermaphrodite meson. *Physics Letters B*, 116(5):365–368, 1982.

[2] Yoichiro Nambu. Electromagnetic currents in dual hadrodynamics. *Physical Review D*, 4(4):1193, 1971.

[3] Yoichiro Nambu. The confinement of quarks. *Scientific American*, 235(5):48–63, 1976.

[4] EI Ivanov, DL Stienike, DI Ryabchikov, GS Adams, T Adams, Z Bar-Yam, JM Bishop, VA Bodyagin, DS Brown, NM Cason, et al. Observation of exotic meson production in the reaction π^- p$\rightarrow \eta'$ π^- p at 18 gev/c. *Physical review letters*, 86(18):3977, 2001.

[5] DV Amelin, Yu G Gavrilov, Yu P Gouz, VA Dorofeev, RI Dzhelyadin, AM Zaitsev, AV Zenin, AV Ivashin, IA Kachaev, VV Kabachenko, et al. Investigation of hybrid states in the ves experiment at the institute for high energy physics (protvino). *Physics of Atomic Nuclei*, 68(3):359–371, 2005.

[6] C Adolph, R Akhunzyanov, MG Alexeev, GD Alexeev, A Amoroso, V Andrieux, V Anosov, A Austregesilo, B Badełek, F Balestra, et al. Odd and even

partial waves of $\eta\pi^-$ and $\eta'\,\pi^-$ in π^- p$\rightarrow\eta^{(\prime)}\,\pi^-$ p at 191 gev/c. *Physics Letters B*, 740:303–311, 2015.

[7] Wikipedia contributors. Standard model — wikipedia, the free encyclopedia, 2018. Accessed: 3-5-2022.

[8] GlueX Collaborators. https://halldweb.jlab.org/doc-private/DocDB/ShowDocument?docid=2442. 2016. Accessed: 8-3-2022.

[9] Nathan Isgur and Jack Paton. Flux-tube model for hadrons in qcd. *Physical Review D*, 31(11):2910, 1985.

[10] Particle Data Group. https://pdg.lbl.gov/2020/tables/rpp2020-tab-mesons-light.pdf. 2020. Accessed: 10-3-2022.

[11] Alexander Austregesilo. *Central production of two-pseudoscalar meson systems at the COMPASS experiment at CERN*. PhD thesis, Technische Universität München, 2014.

CHAPTER 2

THE GLUEX EXPERIMENT

The GlueX (Gluonic Excitation) experiment is a photoproduction experiment performed in experimental Hall D at the Thomas Jefferson National Accelerator Facility (Jefferson Lab or JLab) in Virginia. A photon beam interacting with a proton target is expected to produce heavy but short-lived exotic hybrid mesons that decay into lighter charged and neutral particles. The design of the detector was driven by the primary goal of detecting all of these decay products efficiently. Hence a detector system of almost 4π acceptance and good efficiency was constructed. It consists of a 2-T solenoidal magnet that contains chambers in central forward region for tracking purposes. The energy depositions are measured by a cylindrical shaped calorimeter in the central region located inside the solenoid and a forward calorimeter in the forward direction of the beam which is outside of the magnetic field. The sub-detectors were constructed at different universities in USA and Canada over a period of several years and assembled in Hall D. This chapter describes the photon beam production starting from a 12 GeV electron beam, it's characterization and measurement followed by a brief description of the tracking detectors and calorimeters. A detailed description of the GlueX detector can be found in the GlueX nuclear instrumentation paper [1].

2.1 CEBAF

CEBAF stands for Continuous Electron Beam Accelerator Facility. At the source of polarized electrons are the injectors that produce photoelectrons from the illumination of a gallium arsenide photocathode with a diode-based laser. The pulse of the laser is set to 499 MHz or 249.5 MHz, delivering a beam bunch every 2 ns or 4 ns. The facility has two main linear accelerators (linacs) connected by the arcs

giving a racetrack configuration (figure 2.1) for the electron trajectory. The electrons produced from the injector are then fed to the linear accelerators which use superconducting RF cavities. The cavities produce an oscillating electromagnetic field to accelerate the electrons. With each pass through the linacs, electrons gain 2.2 GeV energy. Electrons undergo a 5.5 pass before they are directed to the Hall D complex, consisting of a tagger hall, a collimator cave and the experimental Hall D detector.

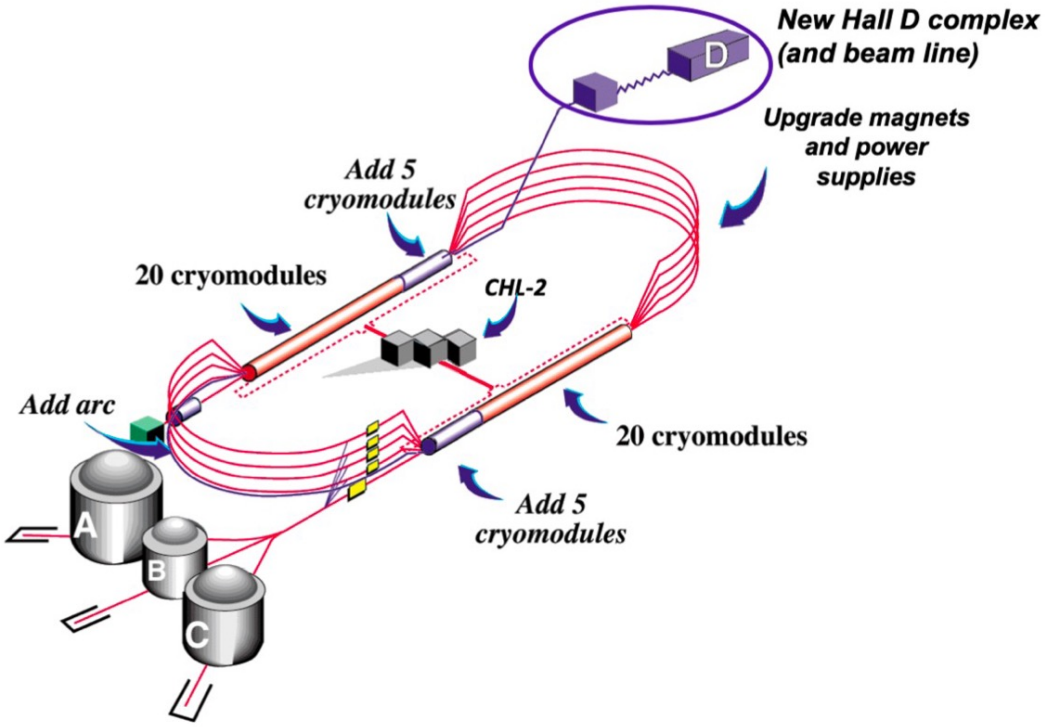

Fig. 2.1. A schematic diagram showing two parallel linear accelerators connected by recirculating arcs and 4 experimental Halls. Hall D is located at the north-east end. Image source [1]

2.2 Coherent Photon Production And The Beamline

Electron beam then enters the tagger hall of the Hall D complex shown in fig. 2.2. Inside the tagger hall, a thin diamond radiator is used to produce a linearly polarized photon beam through coherent Bremsstrahlung. The electron beam position is monitored for stability and position by a beam position monitor located before the diamond radiator. The coherent Bremsstrahlung leads to an intensity enhancement at certain energies in the energy spectrum. A typical coherent spectrum is shown in fig. 2.3. For GlueX, the nominal value for the right edge of the coherent peak used for data taking is near 9 GeV. The exact location of the peak and the degree of polarization in the peak region can be adjusted by the orientation of the diamond radiator with respect to the incident electron beam. In principle, a coherent edge could be produced at any energy value up to the incident beam energy, however, an edge location of 9 GeV together with a 40% peak linear polarization is found to be optimal for the GlueX experiment [1]. The radiator material was chosen as diamond because it has a high probability for coherent scattering in the Bremsstrahlung process [2]. Radiator of thicknesses ranging 20-60 μm were tried out and the optimum value was found to be 50 μm [1].

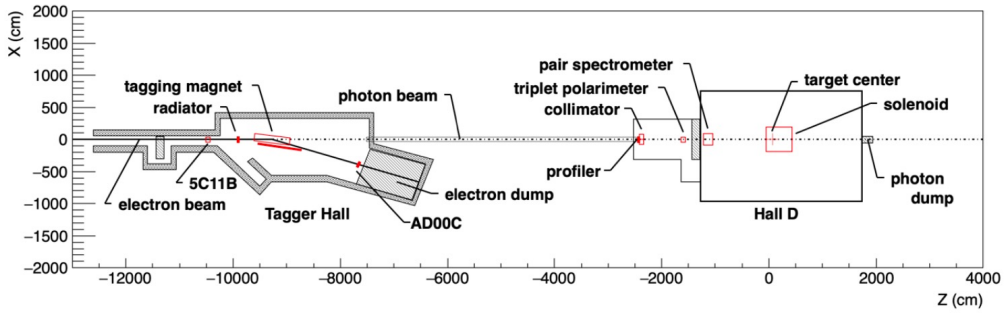

Fig. 2.2. A schematic of the Hall D complex. Image source [1]

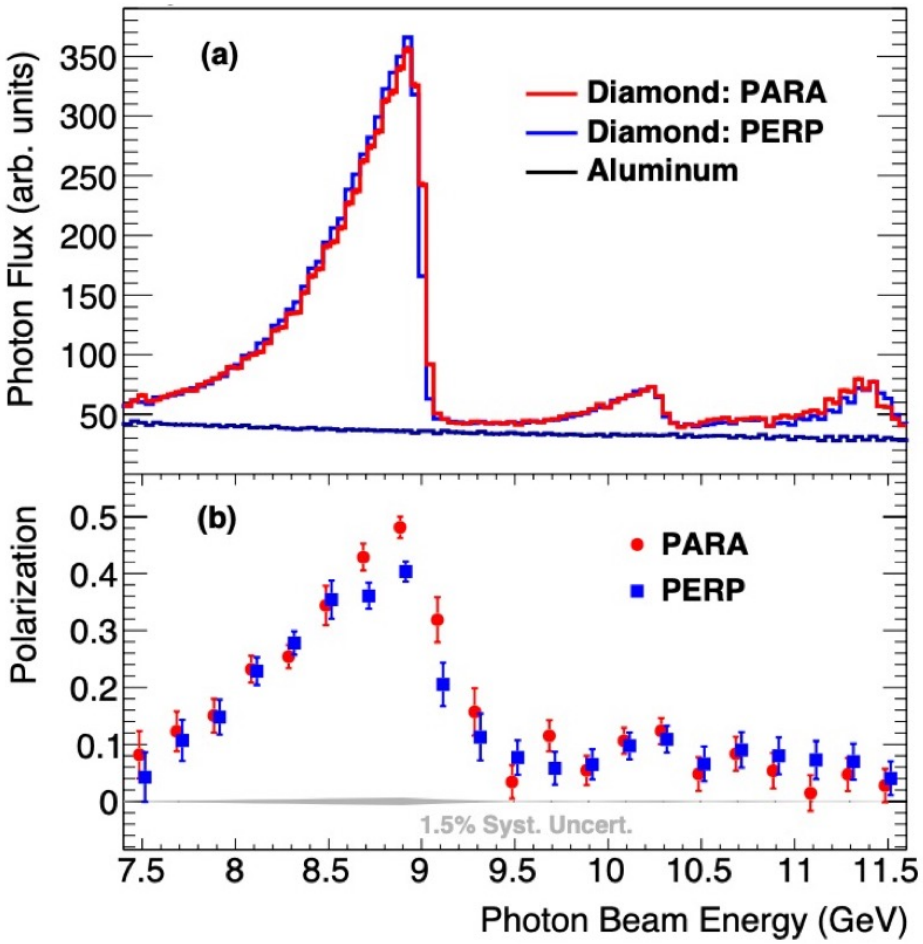

Fig. 2.3. (a) Photon beam intensity as a function of energy : Pair Spectrometer measurement. (b) Photon beam polarization as a function of beam energy : Triplet Polarimeter measurement . PARA and PERP are the polarization plane orientation of the photon beam with respect to the Hall floor. Source [1]

2.2.1 The Photon Tagging System

The Hall D tagging system consists of a dipole magnet, a tagger microscope (TAGM) and a tagger hodoscope (TAGH). After the interaction of the electron beam with the radiator, a mixture of photon and electron beams results. The electrons that didn't interact with the radiator are swept away by a dipole magnet and directed into a

beam dump [1]. TAGH and TAGM are the scintillator detector arrays that measure the energy of the electrons after emitting a Bremsstrahlung photon. The electron energies are determined based on the position of their hits in the arrays TAGH or TAGM. Figure 2.4 gives a conceptual idea of the tagger system. For example an electron with a larger energy loss will be bent more by the tagger magnets, while electrons with a smaller energy loss will be bent less and detected further to the far right in fig. 2.4. TAGM is a high resolution detector that measures the energy of recoil electrons corresponding to the coherent region of the Bremsstrahlung photons with a resolution of about 12 MeV while the TAGH has an energy resolution of 8 MeV to 30 MeV depending on the location of the TAGH counter. The energy of the Bremsstrahlung photon is determined by the equation $E_\gamma = E_0 - E_e$, where E_0 is the energy of the incident beam and E_e is the energy of the post Bremsstrahlung electrons. Thus resulting polarized photon beam travels about 75 m and encounters a tungsten plate where off-axis beam photons are intercepted before they enter the collimator .

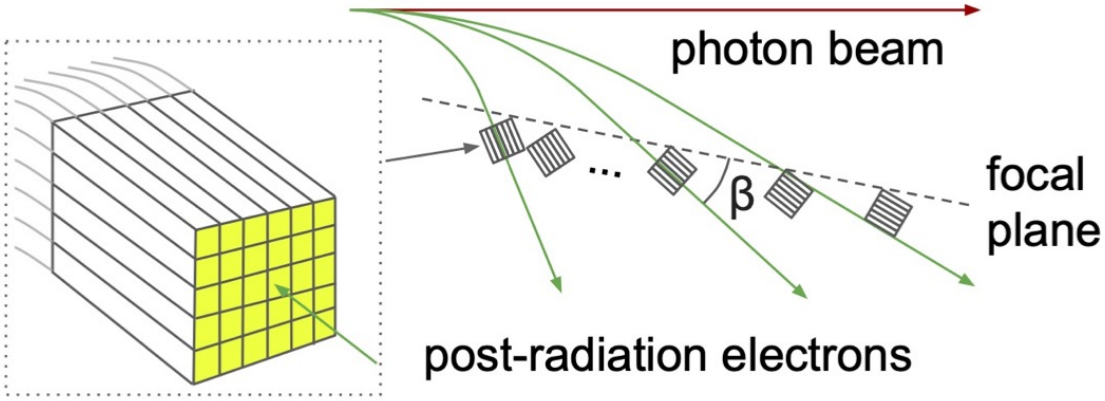

Fig. 2.4. Tagger microscope design. Image source [1]

2.2.2 Photon Beam Flux And Polarization Measurement

Triplet Polarimeter

In order to measure the photon beam polarization, the collimated photon beam is incident on a thin 75 μm beryllium target which acts as an electron target. The electromagnetic reaction $\gamma e^- \rightarrow e^- e^+ e^-$ can be analyzed to study the "slow" recoil electron which is detected in the triplet polarimeter (TPOL) and can be used to measure the photon beam polarization. The fast $e^- e^+$ pair is detected in the pair spectrometer (PS) further downstream and is used to measure the photon beam flux. This will be described briefly in the next section. The cross-section for a pair photoproduction by a polarized photon beam can be written as ,

$$\sigma_t = \sigma_0[1 - P\Sigma cos(2\phi)] \tag{2.1}$$

where σ_0 is the cross-section in case of a non-polarized beam [1]. P is the photon beam polarization that we want to measure and Σ is the beam asymmetry. The energy and azimuthal angle of the recoil electron can be measured by the TPOL detector system and the yield per azimuthal angle bin is fitted to a function of the form $A[1 - Bcos(2\phi)]$ and from the fit parameter B one can determine P given that Σ is known, which can be calculated from quantum electrodynamics *qed* for such an interaction [3]. The acceptance and efficiency of the detector system is extracted from a Monte Carlo simulation.

Pair Spectrometer

The $e^- e^+$ pair from the triplet photoproduction is detected in the Pair Spectrometer (PS) shown in fig.2.5. A 1.8 T dipole magnet bends the pair in opposite direction. A high granularity hodoscode PS-A and a set of coarse counters PSC-A

are two types of scintillators, that that use the silicon photo-multipliers (SiPMs) and photo-multiplier tubes (PMTs) as read outs respectively. The timing resolution is about 120 ps and this measurement in conjunction with tagger measurement identifies conincident beam photons. A conincidence in the two arms of PS is also used as a trigger, in addition to physics trigger from the calorimeters (see section 3.1). The pair energy resolution of the PS hodoscope is about 25 MeV [1]. An important measurement that is required for calculating any cross-sections is the photon beam flux. The raw yield of the detected e^-e^+ pairs is calculated from e^-e^+ counts in the PS detector as a function of energy. The total number of photons incident on the GlueX target is determined from raw yield. It requires the calibration parameters corresponding to the fraction of photon beam that converts to e^-e^+ pair [4].

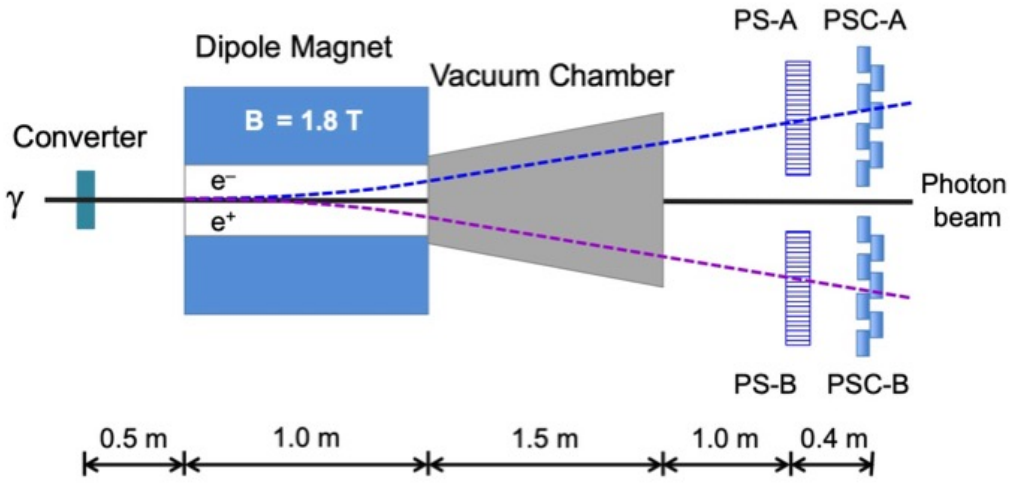

Fig. 2.5. A schematic of the Pair Spectrometer. Image source [5]

2.3 The GlueX Detector

A schematic of the GlueX detector is shown in fig. 2.6. At the center of the detector is a 30 cm long target cell with a diameter of about 1.6 cm filled with liquid hydrogen.

The target density is kept constant at $71.2 \pm 0.3 mg/cm^3$. Particles produced in the photon-proton interaction and their decay products are tracked and their energies are measured by the GlueX detector. In this section, a brief description of each sub-detector is provided.

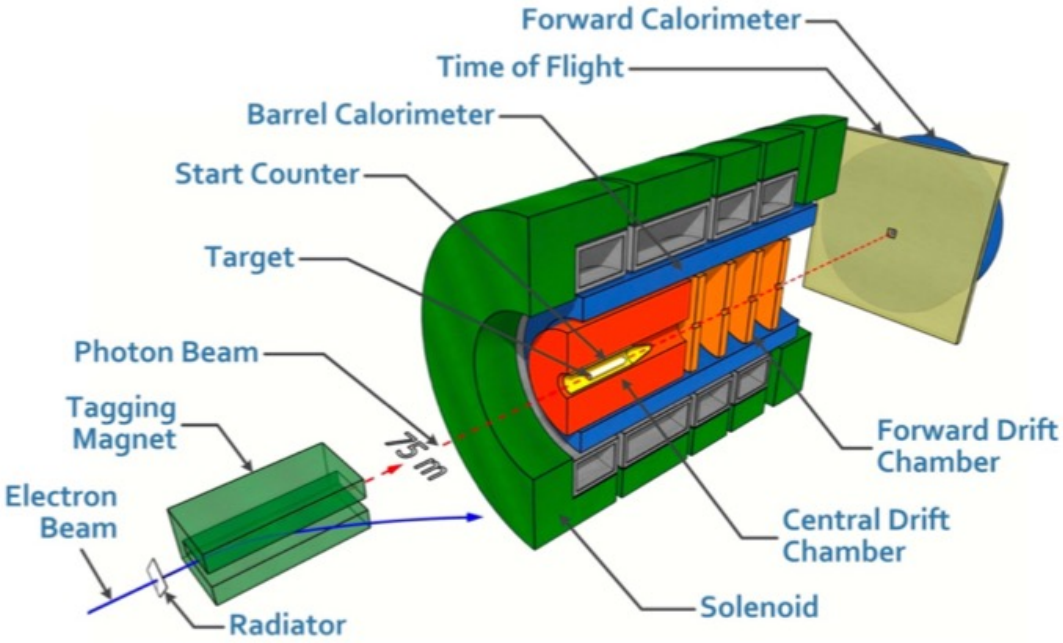

Fig. 2.6. A schematic of the GlueX Spectrometer. Image source [1]

2.3.1 Start Counter

The primary purpose of the GlueX Start Counter (SC) is to identify which of the 4ns beam bunches initiated the reaction. The SC consists of a cylindrical array of 30 thin scintillators that taper towards the forward region to increase the acceptance. Each paddle was manufactured to be 3 mm thick and diamond milled to be 600 mm in length and 20 mm wide. A schematic of the SC enclosing the target is shown

in figure 2.7. Each paddle is read out at the upstream end using SiPMs, connected to flash ADCs and TDCs [4]. It is designed to operate at tagged photon beam intensities of up to 10^8 γ/s in the coherent peak where the photons range in energy from 8.2 to 8.8 GeV [6]. More details on the design, construction and calibration can be found in reference [7]. The timing calibration of the SC was repeated for the GlueX Phase-II data taking in the same way as mentioned in [8].

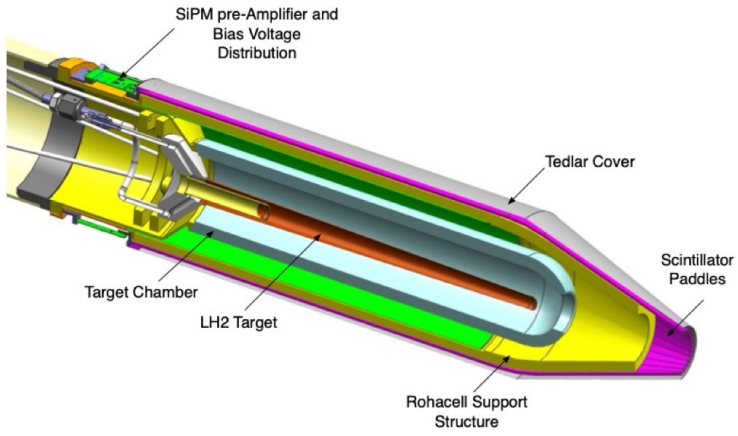

Fig. 2.7. A schematic of the Start Counter enclosing the target. Image source : [7]

2.3.2 Tracking Detectors

The solenoidal magnet encloses a Central Drift Chamber (CDC) and a Forward Drift Chamber (FDC) which are used for tracking the charged particles.

Central Drift Chamber

The CDC consists of 3522 straw drift tubes arranged in 28 layers. Each starw consists of a Mylar tube of 15.55 mm inner diameter. The inner surface of the tube

is coated with vapor-deposited aluminium which acts as cathode. The aluminium is about 100 nm in thickness. Along the central axis of the tube, a 20 μm gold-plated tungsten anode is inserted which acts as anode. The tube is filled with 1:1 argon-carbon dioxide gas mixture at atmospheric pressure. The CDC covers a polar angle between 6° to 168° and spans a space between inner radius 10 cm and outer radius 56 cm. The anode wires are held at +2.1 kV during normal operation.

CDC is used to track charged particles by providing position, timing and energy loss measurements. More details of the CDC can be found in reference [1].

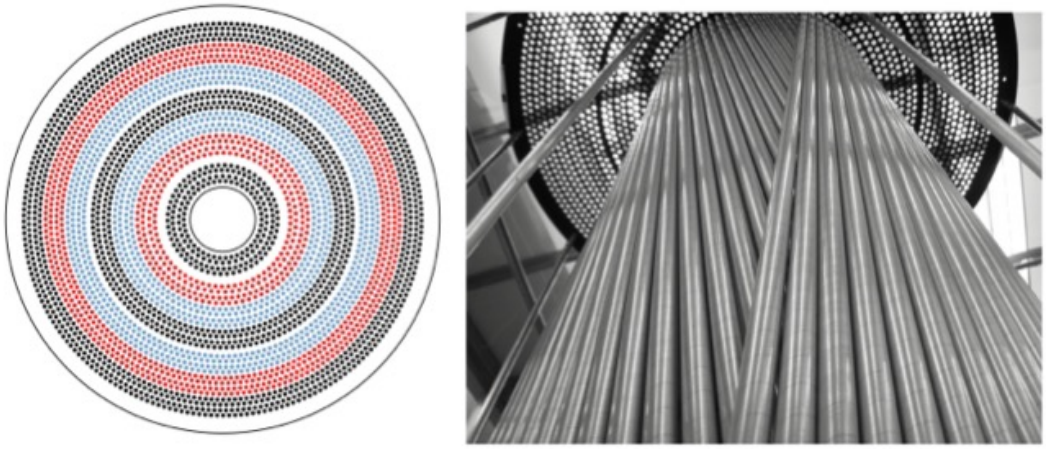

Fig. 2.8. (Left) A schematic of the Central Drift Chamber viewed from the upstream end plate. (Right) CDC at the time of construction. The straw tubes are shown connected tot he end plate.Image source [9]

Forward Drift Chamber

The charged particles in very forward direction are detected in Forward Drift Chamber(FDC). Charged particles with polar angles between 1° to about 10° are covered by FDC. It consists of of 24 disc-shaped planar drift chambers of 1 meter diameter each and grouped into 4 packagaes of 6 chambers each. A schematic of each chamber is shown in fig. 2.9. A wire plane consisting of 20 μm diameter

sense wires and 80 μm diameter field wires 5 mm apart is sandwiched between two cathode planes. A gas mixture of argon to carbon dioxide in a ratio of 2:3 is used, the sense wires are maintained at +2.2 kV and the field wires at -0.5 kV. The position resolution for a corresponding hit to wire distance of range of (4.5 mm - 0.5 mm) is about (140 μm - 240 μm) [4].

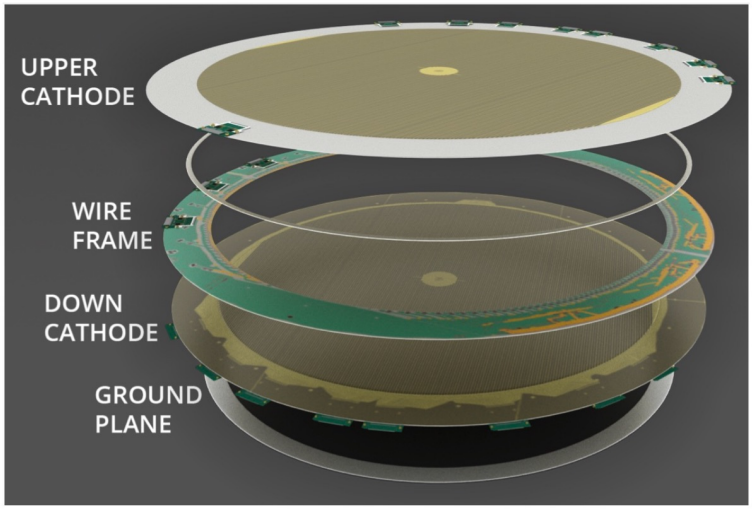

Fig. 2.9. A schematic of the Forward Drift Chamber. Image source [1]

2.3.3 Calorimeter System

The GlueX calorimetry system consists of the Barrel Calorimeter and the Forward Calorimeter.

Barrel Calorimeter

The Barrel Calorimeter (BCAL) is an open cylindrical electromagnetic calorimeter which detects photons of energies from 50 MeV upto a few GeV. It covers a polar angle of 11° to 126° and an azimuthal angle of 2π as shown in fig. 2.10 (b). It consists of 48 modules. Each module is a sandwich 0.5 mm thick lead sheets and 1 mm diameter scintillating fibers with a total of 185 lead sheet layers and 15000 scintillating fibers. The scintillating fibers are read out by SiPMs which are not affected by the solenoidal magnetic field. The high energy photons and electrons produce electromagnetic showers in the fiber/lead sandwich. The energy and the time of the shower is measured by BCAL for particle identification. More information on BCAL can be found on [10].

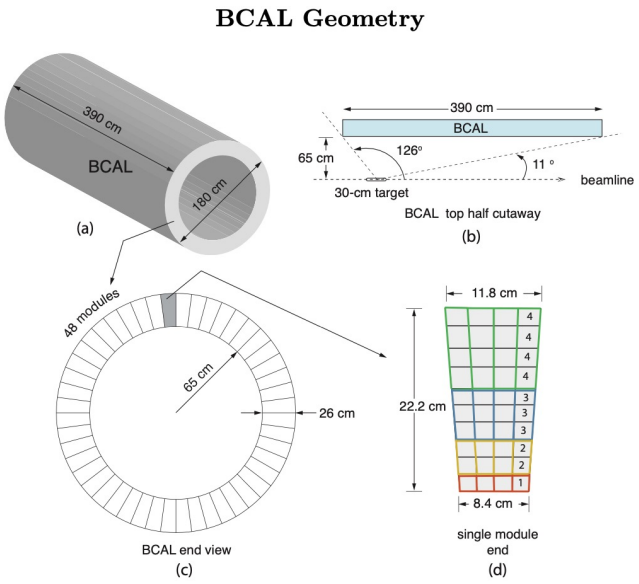

Fig. 2.10. BCAL geometry. (a) BCAL design and size scale. (b) Polar angle coverage and distance of BCAL from target. (c) Cross-section view of BCAL. (d) 4 layers of each module. Image source [10]

Forward Calorimeter

Since the GlueX experiment is a fixed target experiment, a lot of particles are produced at the small angles with respect to the photon beam. The Forward Calorimeter (FCAL) in GlueX detects photons in the polar angle range between 1° to 11°. It consists of 2800 lead-glass blocks, each $4 \times 4 \times 45 cm^3$ arranged in a circular pattern as shown in fig. 2.11. Cherenkov radiations are produced by electromagentic showers in lead-glass and is detected by photo-multipliers (PMT). PMT's can be used as since FCAL is outside the solenoid magnet. The number of Cherenkov photons is proportional to the energy deposited in the lead-glass blocks and hence can be related to the total energy of the photon that started the electromagnetic shower. The FCAL detects photons of energy ranging from 0.1 GeV to several GeV.

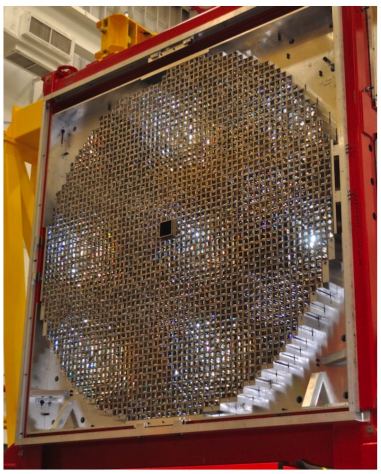

Fig. 2.11. Forward Calorimeter during construction. Image source : GlueX Collaboration

Calorimeter Performance

A calorimeter's photon energy resolution can be parameterized as

$$\frac{\delta E}{E} = \sqrt{\frac{a^2}{E(GeV)} + b^2} \tag{2.2}$$

where E is the photon energy, and a and b are constant terms determined by a fit.

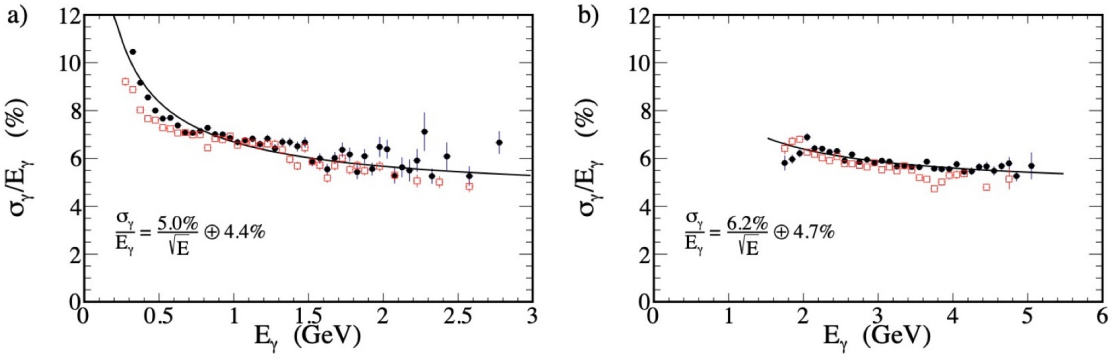

Fig. 2.12. The energy resolution, σ_γ/E_γ as a function of photon energy. Solid black circles are data and open red circles are simulation. The fits to the data are shown by the black curves. Source : [1]

2.3.4 The Time of Flight

The GlueX time of flight (TOF) detector is shown in fig. 2.13. It consists of a plane of vertical scintillator bars and a plane of horizontal scintillator bars. The position resolution of TOF is about 1.6 cm. It is located 5.5 m downstream of the target and covers a polar angle of 0.6° to 13°.The typical timing resolution of the TOF is 70 ps. TOF measures the time of flight for particles and combining this with the measurement of momentum through tracking, one can extract the particle mass. TOF can identify pions from kaons upto 2 GeV/c.

Fig. 2.13. Time of flight detector. Source : GlueX Collaboration

Bibliography

[1] S Adhikari, CS Akondi, H Al Ghoul, A Ali, M Amaryan, EG Anassontzis, A Austregesilo, F Barbosa, J Barlow, A Barnes, et al. The gluex beamline and detector. *Nuclear Instruments and Methods in Physics Research Section A: Accelerators, Spectrometers, Detectors and Associated Equipment*, 987:164807, 2021.

[2] H Bilokon, G Bologna, F Celani, BD'Ettorre Piazzoli, R Falcioni, G Mannocchi, and P Picchi. Coherent bremsstrahlung in crystals as a tool for producing high energy photon beams to be used in photoproduction experiments at cern sps. *Nuclear Instruments and Methods in Physics Research*, 204(2-3):299–310, 1983.

[3] Michael Dugger, BG Ritchie, N Sparks, K Moriya, RJ Tucker, RJ Lee, BN Thorpe, T Hodges, FJ Barbosa, N Sandoval, et al. Design and construction of a high-energy photon polarimeter. *Nuclear Instruments and Methods in Physics Research Section A: Accelerators, Spectrometers, Detectors and Associated Equipment*, 867:115–127, 2017.

[4] Yang Yunjie. *Commissioning the DIRC Detector and Searching for Axion-like Particles at GlueX*. PhD thesis, Massachusetts Institute of Technology, 2021.

[5] F Barbosa, C Hutton, Alexandre Sitnikov, A Somov, S Somov, and Ivan Tolstukhin. Pair spectrometer hodoscope for hall d at jefferson lab. *Nuclear Instruments and Methods in Physics Research Section A: Accelerators, Spectrometers, Detectors and Associated Equipment*, 795:376–380, 2015.

[6] H Al Ghoul et al. Gluex collaboration. In *AIP Conf. Proc*, volume 1735, page 020001, 2016.

[7] Eric Pooser, Fernando Barbosa, Werner Boeglin, Charles Hutton, MM Ito, Mahmoud Kamel, Puneet Khetarpal, Anthony Llodra, N Sandoval, Simon Taylor, et al. The gluex start counter detector. *Nuclear Instruments and Methods in Physics Research Section A: Accelerators, Spectrometers, Detectors and Associated Equipment*, 927:330–342, 2019.

[8] Kamel Mahmoud. *Photo-Production of η mesons*. PhD thesis, Florida International University, 2020.

[9] NS Jarvis, CA Meyer, B Zihlmann, M Staib, A Austregesilo, F Barbosa, C Dickover, V Razmyslovich, S Taylor, Y Van Haarlem, et al. The central drift chamber for gluex. *Nuclear Instruments and Methods in Physics Research Section A:*

Accelerators, Spectrometers, Detectors and Associated Equipment, 962:163727, 2020.

[10] Tegan D Beattie, AM Foda, CL Henschel, S Katsaganis, ST Krueger, GJ Lolos, Zisis Papandreou, EL Plummer, IA Semenova, A Yu Semenov, et al. Construction and performance of the barrel electromagnetic calorimeter for the gluex experiment. *Nuclear Instruments and Methods in Physics Research Section A: Accelerators, Spectrometers, Detectors and Associated Equipment*, 896:24–42, 2018.

CHAPTER 3

ANALYSIS PART 1 : EVENT SELECTION AND BACKGROUND STUDIES

3.1 Outline

The polarized photon beam impinges on a liquid hydrogen target at the center of the GlueX detector system. Particles produced from the interaction then fly across the sub-detectors and upon hitting the detectors, interact with the detector material producing electronic signals. At the fundamental level, all signals can be categorized into either timing signals or charge signals. Time signals are collected and digitized by time-to-digital converters (TDC's). The TDC's are basically stop watches that measure time interval. While charge signals are collected and digitized by charge-to-digital converters (QDC's) [1]. The trigger system in GlueX is optimized to record mostly high energy hadronic interactions based on the measurement of energy deposition in the Forward and Barrel Calorimeters [2]. The GlueX trigger also requires time coincidence of the hits in the two arms of the Pair Spectrometer detector [2]. This analysis uses the GlueX phase I data set which was taken on Spring 2017, Spring 2018 and Fall 2018. The trigger rate was 40 KHz and approximately 270 billion triggers were recorded during the phase I operation [2].

Figure 3.1 shows the analysis flow for this project. The first step is to calibrate the detectors and reconstruct events. For TDC and QDC signals to be useful, they have to be calibrated. The timing calibration is needed because the signals should be measured and corrected relative to some reference time [1]. For GlueX detectors that are instrumented with QDC for example for Central Drift Chamber and Forward Calorimeters, charge collected in a QDC is proportional to the amount of energy deposited. The proportionality is determined by calibration [1]. The energy of the

particles are measured by the amount of light produced by the particle hits in the Forward and Barrel calorimeters. The particles entering the drift chambers make a hit in the wire that is read out as time signals which when combined with the drift velocity will give the distance of closest approach of the particle from where it initiates the ionization in the chamber to the wire. This gives a measured value of the position. Also since the charged particle is in a homogeneous magnetic field, the momentum vector perpendicular to the magnetic field changes direction. The momentum vector parallel to the magnetic field is not affected. The resultant motion is a helix. The measured position and momenta are then fitted to a helix. The fitted function is used as a track for each particle that intercepts the drift chamber. With the information of momenta from tracking and energy from calorimeters for each particle, the particle is thus assigned a measured 4-momentum vector from which one can extract interesting variables like invariant mass, energy, momentum and angles in different frames for physics analysis.

Detector information like time and energy loss are used to make loose selection cuts based on the expected behaviour of the well known particles. These are called particle identification cuts. For example an expected timing window for different detectors can be estimated for a π^+ meson. Similarly, an expected energy loss behaviour can be predicted and a cut around the nominal value can be used. This helps to identify the different particles like pions, kaons etc. A list of the standard GlueX analysis launch cuts used for 2017, 2018 and 2019 data can be found here https://halldweb.jlab.org/wiki/index.php/Spring_2017_Analysis_Launch_Cuts

The rest of this chapter explains the event selection for the current analysis and kinematic fitting. Then a discussion of the identification of alternate channels follows. Finally two different methods of signal-background separation is discussed.

Chapter 4 will be dedicated to the process of extraction of partial wave amplitudes and moments.

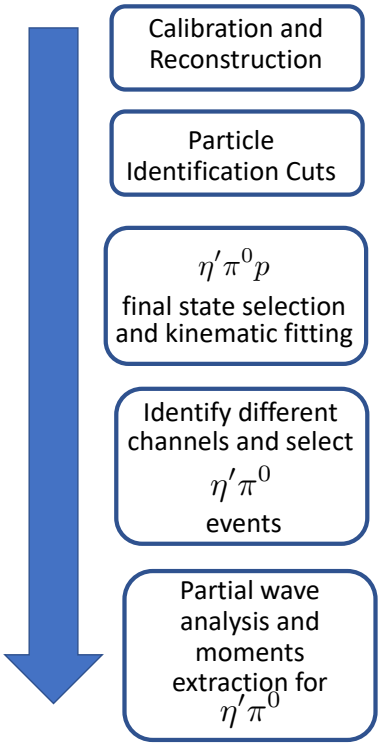

Fig. 3.1. Analysis Flowchart

3.2 Event Selection

The current analysis is the study of $\eta'\pi^0$ channel. A complete t-channel Feynman diagram is shown in fig. 1.6. The polarized beam photon interacts with a target proton through some exchange particle E_X. A resonance X is produced which decays into an η' and a π^0. The π^0 again decays into $\gamma\gamma$ and the η' decays into $\pi^+\pi^-\eta$, out of which the η decays into $\gamma\gamma$. Thus the final state is identified by 3 charged tracks ($\pi^+\pi^- p$) and 4 neutrals ($\gamma\gamma\gamma\gamma$), all of which are required to be detected. If an event has 3 charged tracks and 4 neutral showers then the event is accepted as a possible signal event. In addition, up to 3 extra charged tracks were

allowed in the selected topology, so that a track originating from a detector noise is not misidentified as a true track. This might increase the possibility of background inclusion in the data set, but it will reduce the possibility of a good event being rejected. Out of 270 billion triggers, one can filter out a particular final state, in this case, 3 charged tracks (2 positive and 1 negative) and 4 neutral showers with upto 3 extra charged tracks admissible. The selected topology is then written into ROOT trees which is used by the analyser for further event selection and extracting observables.

3.2.1 Kinematic Fitting

Kinematic fitting is an involved process to obtain a new and improved set of measured variables by a) varying the measured quantities within their errors and b) by using constraints based on physics information such as conservation laws like energy and momentum conservation and common vertex constrain. In general one can define a χ^2 as,

$$\chi^2 = (\boldsymbol{y} - \boldsymbol{\eta})^T \boldsymbol{V_y^{-1}} (\boldsymbol{y} - \boldsymbol{\eta}) + 2\boldsymbol{\lambda}^T \boldsymbol{f} \tag{3.1}$$

Here $\boldsymbol{y}$ represents the measured values and $\boldsymbol{\eta}$ represents the estimated values of the observables [3]. $\boldsymbol{V_y^{-1}}$ is the covariance matrix of the experimentally measured data $\boldsymbol{y}$ as the $\boldsymbol{y_i}$ are not necessarily independent. $\boldsymbol{\lambda}$ is a set of unknown constant Lagrange multipliers which are free parameters during fitting and $\boldsymbol{f}$ are the set equations for constraints. The first part of the right hand side introduces the detector resolution while the second part introduces energy and momentum conservation, common vertex and mass constraints of the particles if any. For the current analysis, the kinematic fit included a 4-momentum conservation which conserves energy and

momentum , a common vertex constraint which requires the final state to originate from the same point in space and mass constraints which enforce two final state photons to be a π^0 and the other two to be an η. A possible bias might have been introduced at this point. But a signal to background separation for a comparatively small background underneath the η' signal was preferable. A larger background underneath the η' signal was observed in a mass unconstrained fit. The χ^2 is then minimized by setting the partial derivatives with respect to $\boldsymbol{\eta}$ and $\boldsymbol{\lambda}$ equal to zero. A cumulative χ^2 probability distribution is defined as,

$$F(\chi^2) = \int_{\chi^2}^{\infty} f(\chi^2)\, d\chi^2 \tag{3.2}$$

where $f(\chi^2)$ is the χ^2 probability density distribution. Ideally $F(\chi^2)$, also known as the confidence level, is a flat distribution between 0 and 1. A $F(\chi^2)$ closer to 0 corresponds to a higher value of the reduced χ^2 of the fit. Figure 3.2 shows an example of the $F(\chi^2)$. A large number of events close to 0 correspond to poor fits. A cut at 0.001 indicated by red vertical line was used and events with value $F(\chi^2)$ > 0.001 were selected.

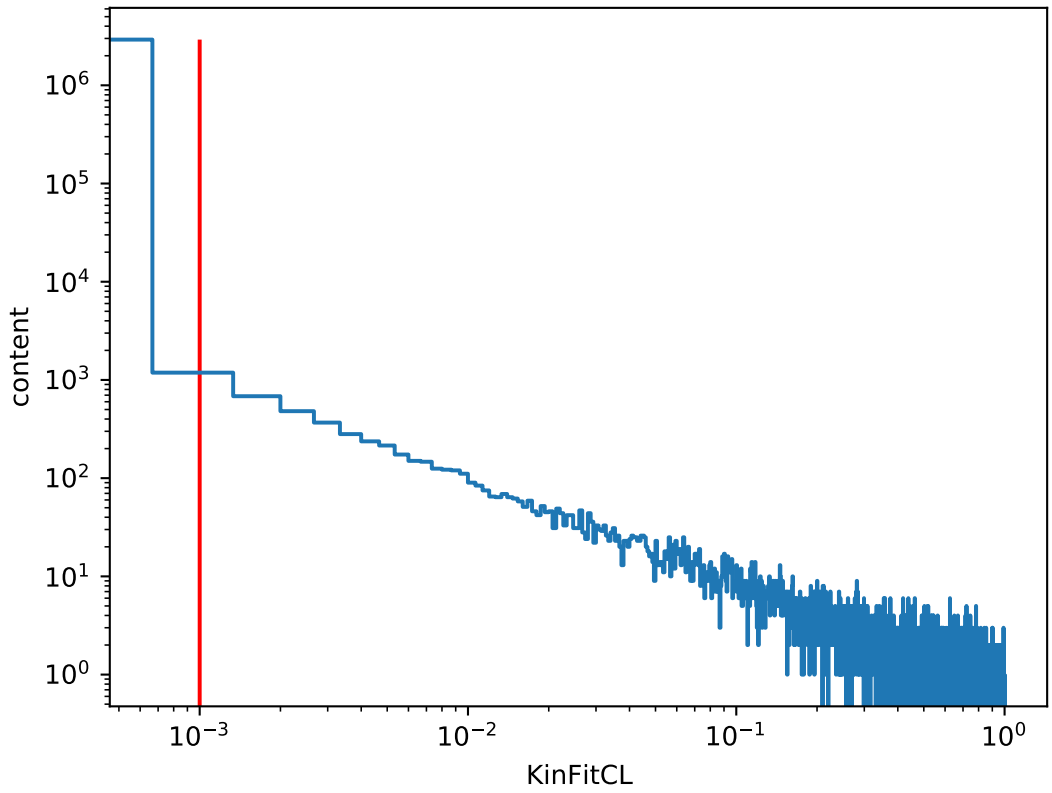

Fig. 3.2. Kinematic Fitting Confidence Level. Ideally this should be a flat distribution. Large fraction of events close to 0 correspond to poor fits and are rejected. For demonstration purpose, this distribution was taken from a single run and hence is not flat due to lack of statistics.

3.2.2 Timing Distribution

Since the accelerator delivers electron beam bunches every 4 ns to the hall, the (Radio Frequency) RF time is the time calculated from the frequency at which accelerator is run i.e. 1497 MHz. The time of hit of the final state tracks in the detector can be back tracked to a common point in space and time, where the reconstruction for different final states converge. This is the common vertex and the time for the common vertex is the beam time. Figure 3.3 shows the difference

between the RF time and the beam time. A central peak , followed by accidental peaks are seen. This analysis uses the events that fall only in the central peak of timing window (-2 ns, 2 ns) in between vertical red lines. The efficiency of tagger is the ratio of recorded hits divided by all hits from electrons. The GlueX tagger has a dead time of about 25 ns and that means the tagger can't distinguish two electrons that are within 25 ns in time interval. In addition to this, the scintillator has a cross section of 3mm by 3mm but it has a cladding of about 0.15mm that is not scintillator so the active area is only 2.85mm by 2.85mm. As a consequence only about 90% of the hits get registered. Due to these imperfections in tagger, a particular final state might correspond to multiple beam photons. A final state associated with each of these beam photons is called a combination. Even if an event has one and only one beam photon associated with a particular final state, the final state particles can be permutated to provide new combinations. These are the sources of duplicate events which within the selected timing window in fig. 3.3 might pass through all selection cuts. The fraction of such events will be estimated and addressed in section 3.4 after applying most of the event selection cuts.

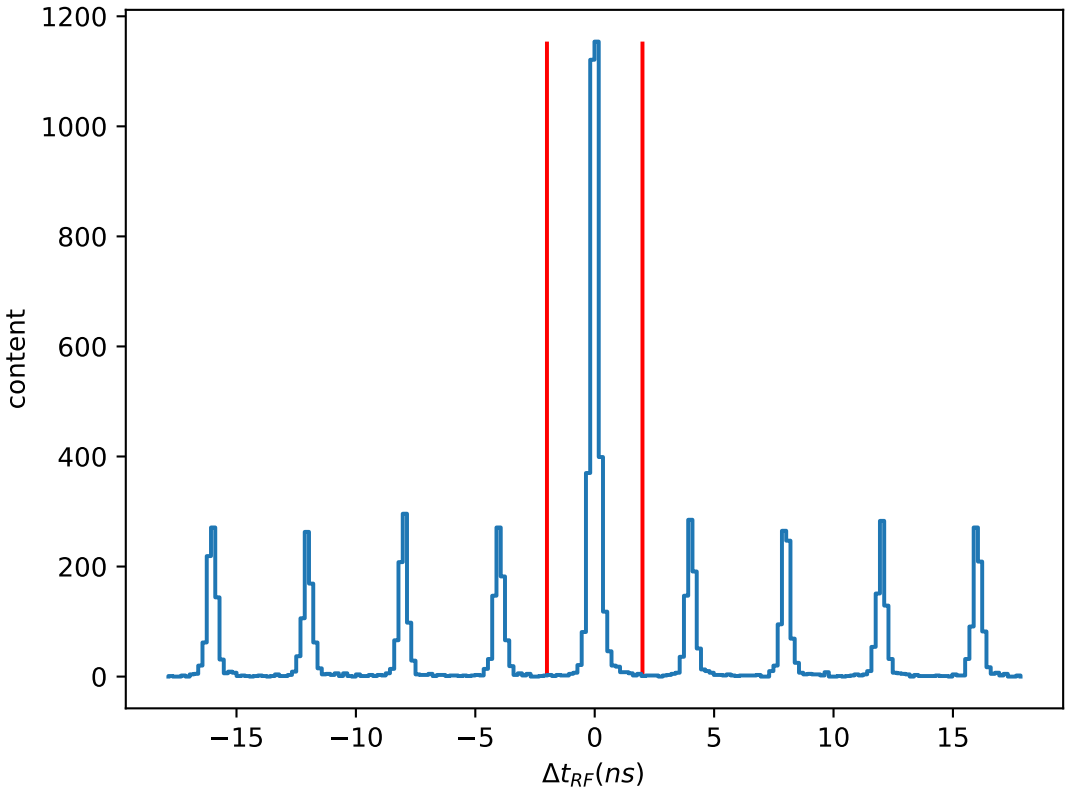

Fig. 3.3. The timing difference between the RF time and the beam time. The central peak is the coincidence (prompt) peak and the adjacent peaks are called the accidental peaks. Only the events within the prompt peak (-2ns, 2ns) within the vertical red lines are selected for analysis.

3.2.3 Missing Mass Squared

The difference in 4-vectors of the initial state $p_i = p_{beam} + p_{targetproton}$ and the final state $p_f = p_{\pi^+} + p_{\pi^-} + p_{recoilproton} + p_\gamma + p_\gamma + p_\gamma + p_\gamma$ is calculated. Ideally, if all the measurements are exact and nothing is missing, it should be a delta function at 0. The square of the invariant mass of this difference shows some distribution centered around 0 (figure 3.4). This is because the current analysis requires all the particles to be detected. If any charged particle were undetected (missing), the centering

would deviate from 0. And the finite width of the distribution is due to the finite energy and momentum resolution of the detector. Events within the vertical red lines (-0.02, 0.02) $(\mathrm{GeV/c^2})^2$ for this variable were chosen for further analysis.

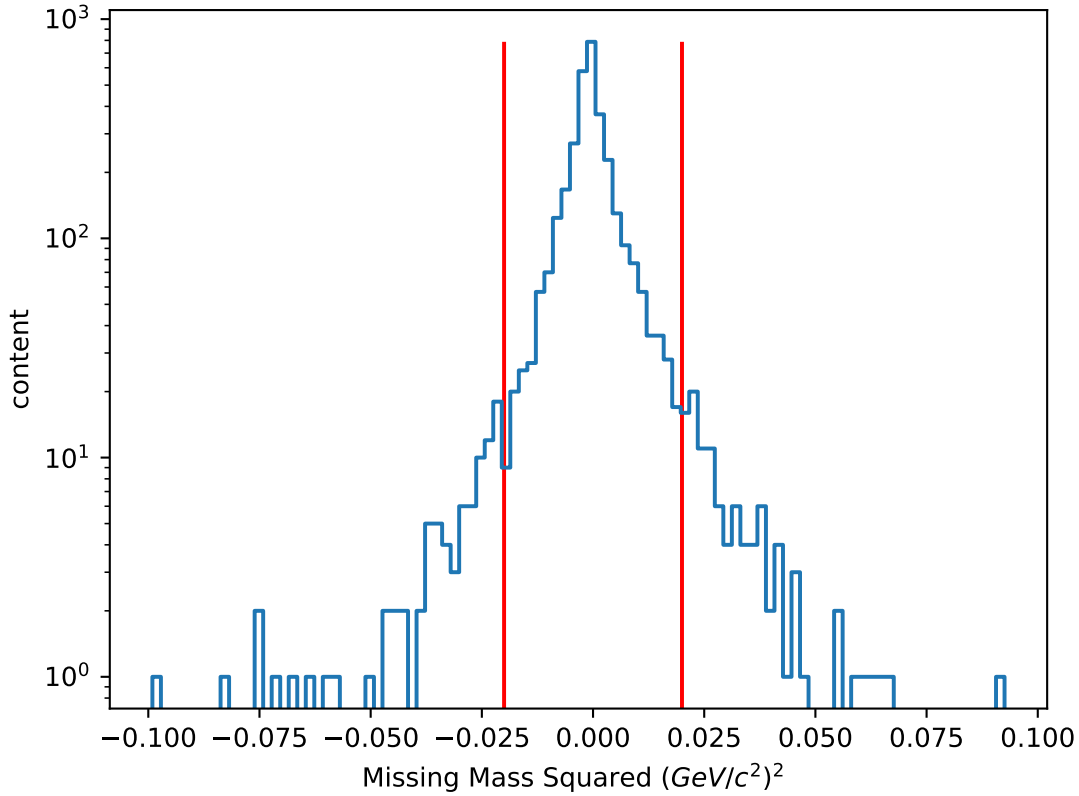

Fig. 3.4. Histogram showing missing mass squared selection between (-0.02, 0.02) between the red vertical lines. The resolution is finite because of the uncertainties in measurements. The distribution is centered around 0 because nothing is missing.

3.2.4 Momentum Transfer

The momentum transfer t shown is defined as $t = -(p_\gamma - p_{\eta'\pi^0})^2$, where p_γ and $p_{\eta'\pi^0}$ are the 4 vectors of incoming beam and $\eta'\pi^0$ system respectively, is shown in fig. 3.5. The events with very low t can't be reconstructed completely because the recoil

system cannot leave the target or pass through all necessary detectors while at high t, other processes like a target excitation (Δ^+ or N^*) are more probable. Hence a t window of (0.1, 0.7) (GeV/c)^2 between the red lines was selected.

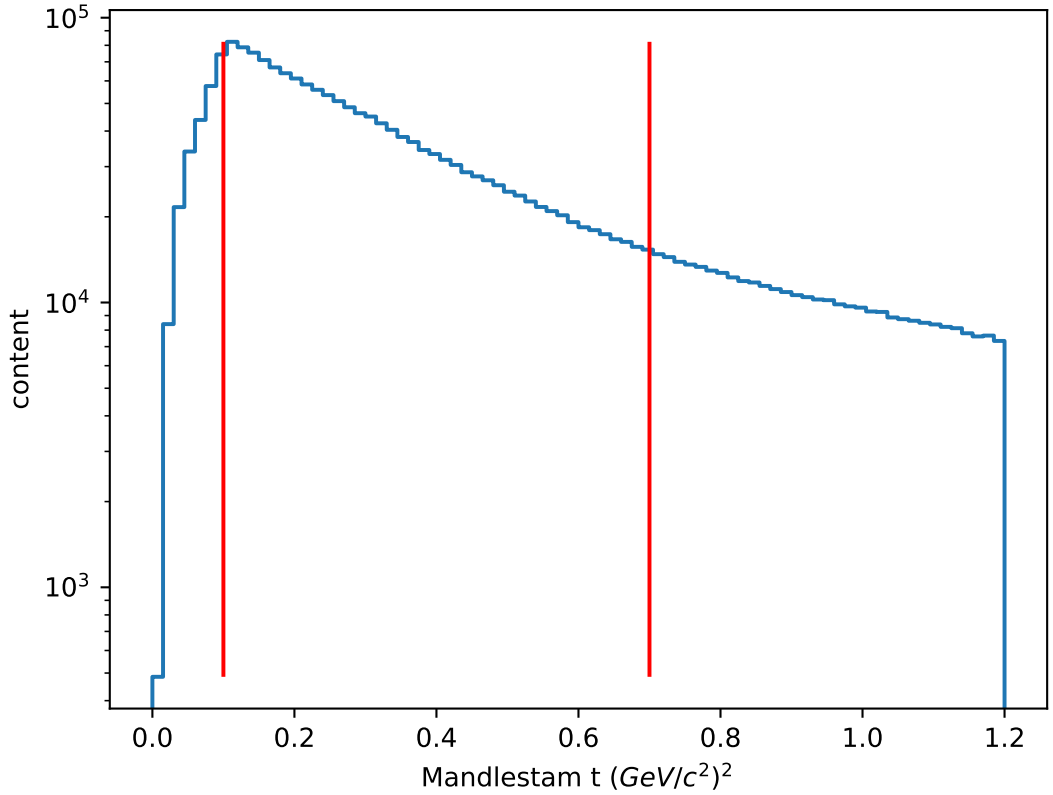

Fig. 3.5. Histogram showing momentum transfer t. A window of (0.1, 0.7) is selected. Events with t < 0.1 might not be reconstructed completely while events with t > 0.7 are not of interest.

3.2.5 Photon Beam Energy

The electrons of energy between 11 GeV to 12 GeV incident on a diamond radiator produce a linearly polarized photon beam through coherent Bremsstrahlung. The photon beam energy was also selected to be in the coherent region of 8.2 to 8.8 GeV

as indicated by red vertical lines in fig. 3.6 where the polarization fraction of the beam is highest.

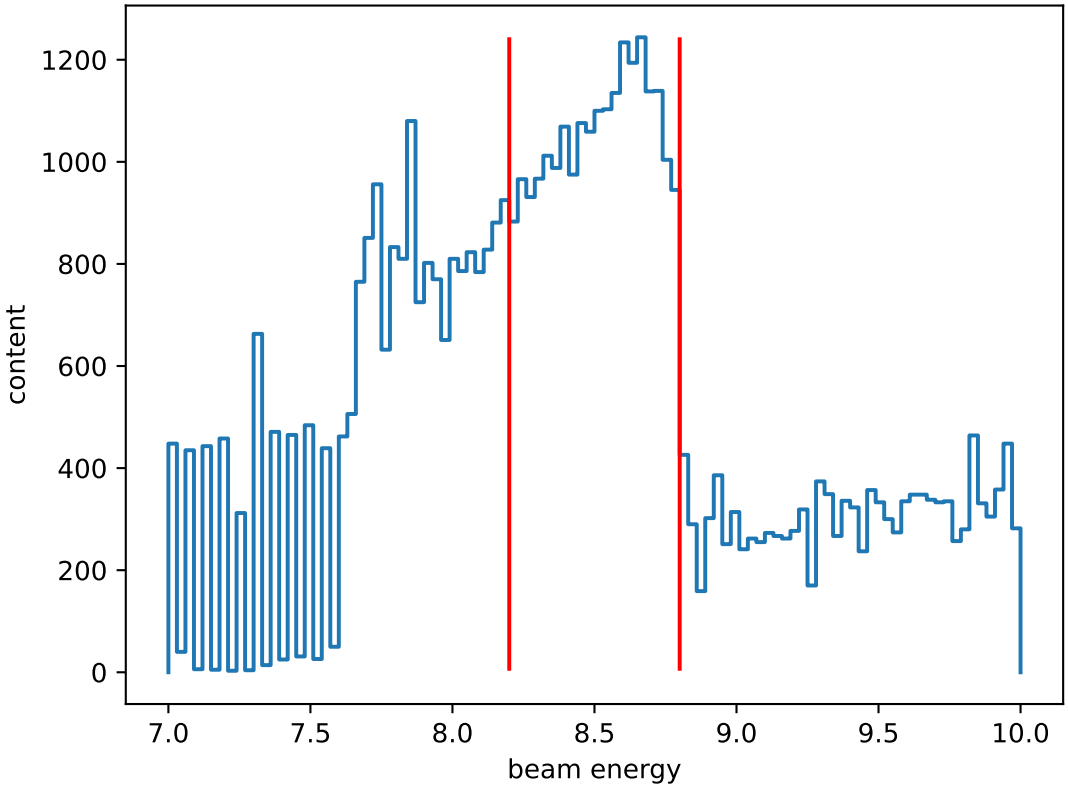

Fig. 3.6. Histogram showing photon beam energy in GeV. A window of (8.2, 8.8) is selected where the beam polarization fraction is estimated to be maximum.

3.2.6 Shower Quality

A shower is a cascade of secondary particles produced as the result of a high-energy particle interacting with dense matter. In general, an electromagnetic shower in FCAL initiated by a photon should have a different signature than a hadronic shower initiated by a π^+ or a π^- in the calorimeter. In GlueX, a neural network was used to distinguish between the two. Eight different types of variables based on 3 different

attributes: a) geometry of shower b) energy deposited and c) timing information of each shower was used to distinguish a shower produced from a photon from a shower produced from a hadron. The photon shower quality score is result of a neural network classifier that is trained to distinguish a photon shower from a hadronic shower in the Forward Calorimeter. More information about the use of neural network can be found in reference [4]. Based on the optimum performance of this neural network, a shower quality close to 1 should distinguish a true photon from a hadronic decay like a π^0 decay while a shower quality close to 0 corresponds most probably to a shower produced from charged particles colliding with the Forward Calorimeter or is a result of detector noise. Figure 3.7 shows a histogram of the shower quality value of a typical final state photon. A typical value of 0.5 is taken and we require that all the 4 final state photons in this analysis be above 0.5 value for shower quality. For the showers in BCAL, work is in progress to obtain the shower quality score. During this analysis, all BCAL showers were assigned a shower quality of 1 by default.

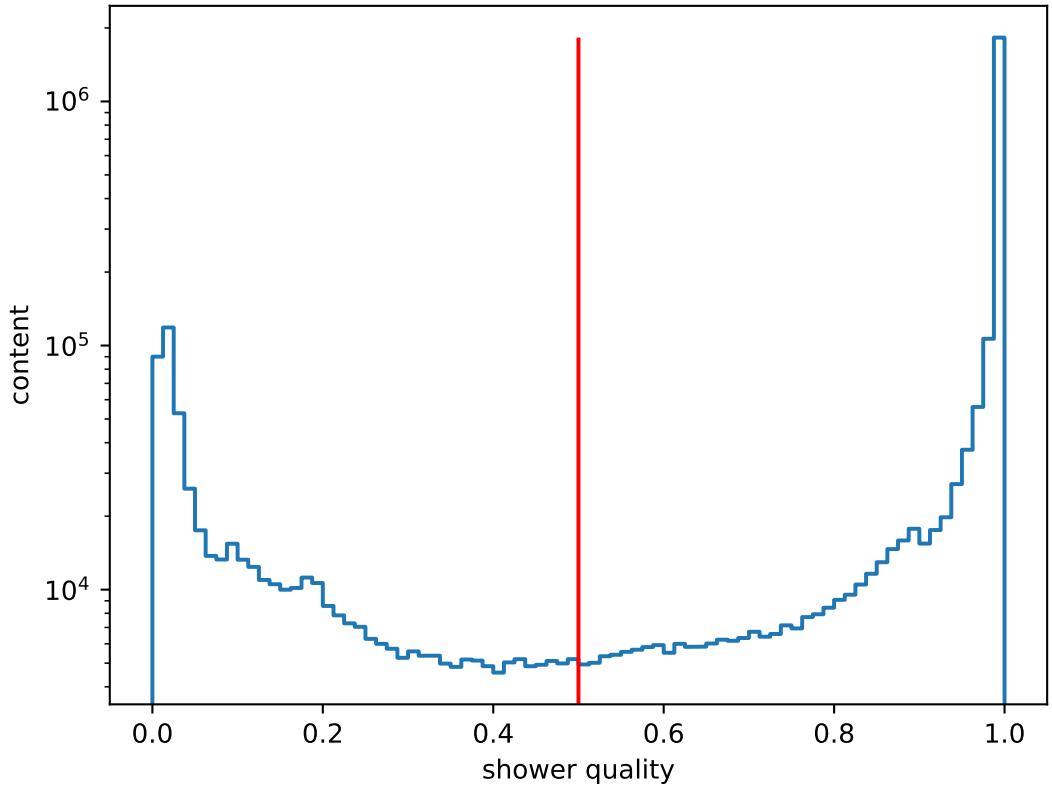

Fig. 3.7. Histogram showing a photon shower quality score. A score of less than 0.5 is more likely to correspond to a hadronic split-off or a detector noise. A score of more than 0.5 is more likely to be a electromagnetic shower initiated by a true photon. For all 4 final state photons detected in FCAL, a score of above 0.5 is required.

3.3 Identification of Alternate Channels

There could be multiple ways of producing a $\pi^+\pi^-$ pair and 4 photons with a final state proton. Out of many possibilities, we could identify 3 important alternate reactions that have the same final state. A discussion of identification of these reactions and their rejection methods are described next.

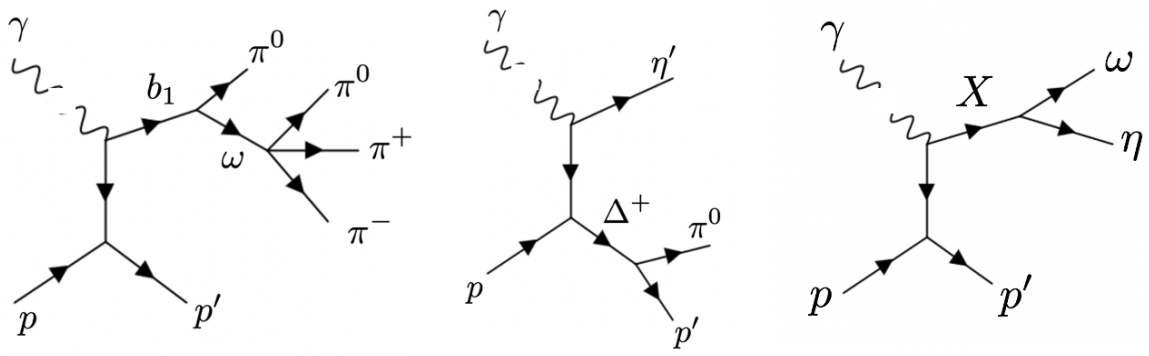

Fig. 3.8. Feynmann diagram showing 3 background reactions for the current analysis. 1) Left : source of $\pi^0\pi^0$ events 2) Center : target excitation Δ^+ background 3) Right : source of $\omega\eta$ events

3.3.1 $\pi^0\pi^0$ Events

The current analysis has 4 photons in the final state namely : $\gamma_1, \gamma_2, \gamma_3$ and γ_4. Kinematic fitting constrains two of them $\gamma_1\gamma_2$ to be a π^0 and the other two $\gamma_3\gamma_4$ to be an η. However, there could be misidentified events like a $\pi^0\pi^0$ that is forced to look like a $\pi^0\eta$ event. In figure 3.9 a set of 2D histograms of the invariant masses of $\gamma_1\gamma_3$ vs $\gamma_2\gamma_4$ (left) and $\gamma_1\gamma_4$ vs $\gamma_2\gamma_3$ (right) are shown. Two distinct features are noticed in top 2 histograms where the majority of events localise. A star shaped polygon and a banana shape. The star shaped polygon is centered around the π^0 mass along both horizontal and vertical directions in both permutations. While there are many potential sources for this, one reaction that might be producing these events is $\gamma p \to b_1 p$, where $b_1 \to \omega\pi^0$ and $\omega \to \pi^+\pi^-\pi^0$ decays follow. A Feynmann diagram of the reaction is shown in the left of fig. 3.8. The bottom two histograms show how the same events show up in two different permutations. The banana events in $\gamma_1\gamma_3$ vs $\gamma_2\gamma_4$ are actually the $\pi^0\pi^0$ events in $\gamma_1\gamma_4$ vs $\gamma_2\gamma_3$.

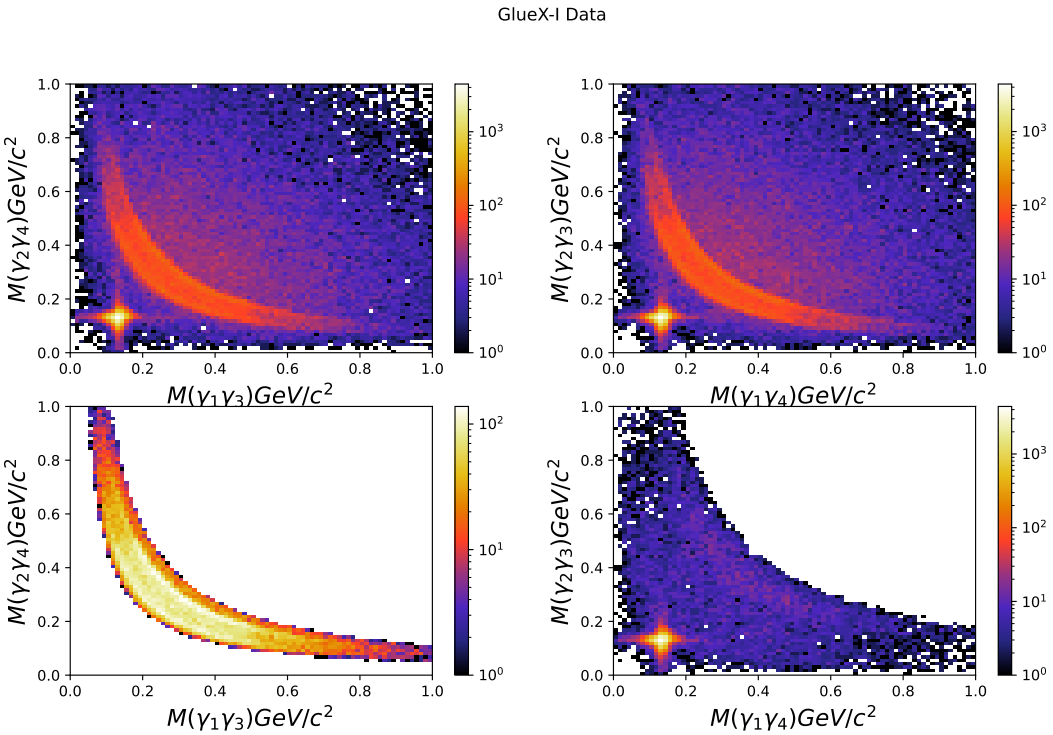

Fig. 3.9. $\pi^0\pi^0$ as background events illustrated in two different permutations of photon pairs. $\gamma_1\gamma_3$ invariant mass vs $\gamma_2\gamma_4$ invariant mas (top left) and $\gamma_1\gamma_4$ invariant mass vs $\gamma_2\gamma_3$ (top right) . The start shaped events localised in bottom left corner in top two histograms are the $\pi^0\pi^0$ events. The bottom two histograms suggest that the $\pi^0\pi^0$ events in one permutation mainly corresponds to the banana shaped events in the other permutation.

The left histogram of 3.10 shows the events that survive after the star shaped polygon cut is used in one of the permutations. The cut that was used to reject $\pi^0\pi^0$ events , however, was used in both permutations with an OR logic i.e. if any event lies in the star shape of either of the two permutations, the event is then rejected. The right histogram of fig. 3.10 shows how the cut affects the invariant mass of $\pi^+\pi^-\eta$. It shows an η' peak at around $0.958\,\mathrm{GeV/c^2}$ on a significant background. The rejected events suggest no signal loss. The same cut on signal MC showed a loss of about 3.13%.

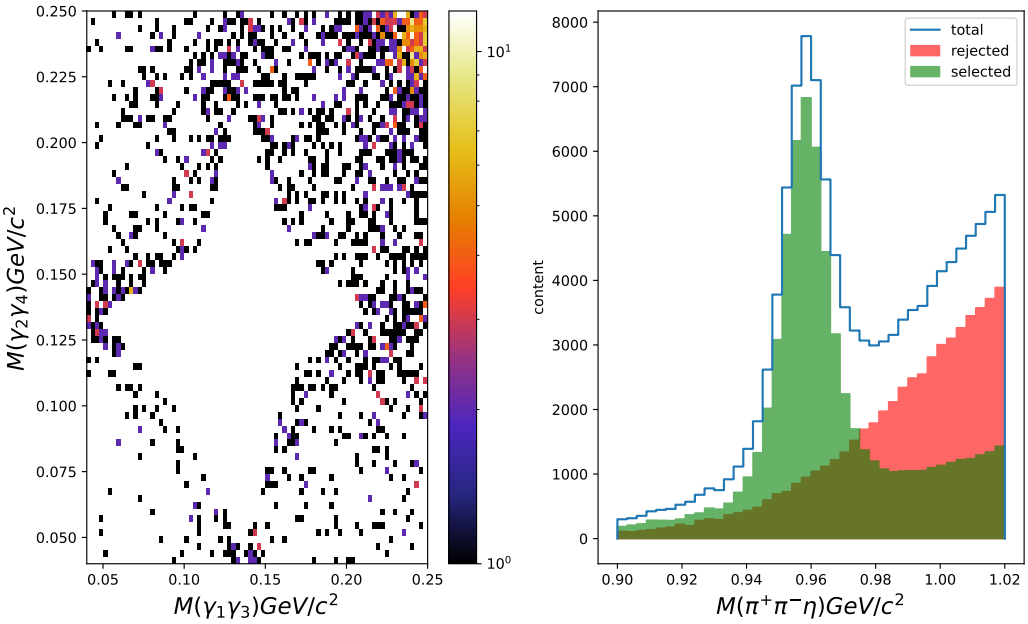

Fig. 3.10. Rejection of $\pi^0\pi^0$ events (left) and the effect of this cut on the $\pi^+\pi^-\eta$ invariant mass distribution (right).

3.3.2 Baryon Resonances

Another source of background could be a t-channel process, where a beam photon interacts with target proton, producing an η' in the upper vertex. A Feynmann

diagram of the reaction is shown in the center of figure 3.8. The momentum transfer to the target would be excited to a Δ^+ baryon. The histogram in figure 3.11 shows the cosine of the polar angle of the final state π^0 in the initial state γp rest frame as a function of the $\pi^0 p$ invariant mass. A strong enhancement is seen at about $1.25\,\mathrm{GeV/c^2}$ extending from the backward angle to about $\cos\theta = 0$. The histogram also indicates a second structure at about $1.6\,\mathrm{GeV/c^2}$ with strength much less than the previous structure. A projection of the 2D histogram onto the $\pi^0 p$ invariant mass is shown to the right. The first peak near the threshold is clearly the dominant structure while the second peak at around $1.6\,\mathrm{GeV/c^2}$ is also visible. These peaks most likely represent the $\Delta^+(1232)$ and $\Delta^+(1600)$ respectively, produced from the reaction $\gamma p \to \eta' \Delta^+$ followed by the decay $\Delta^+ \to \pi^0 p$ producing the same final state as an $\eta' \pi^0 p$ channel. Several possibilities were explored to reject these events.

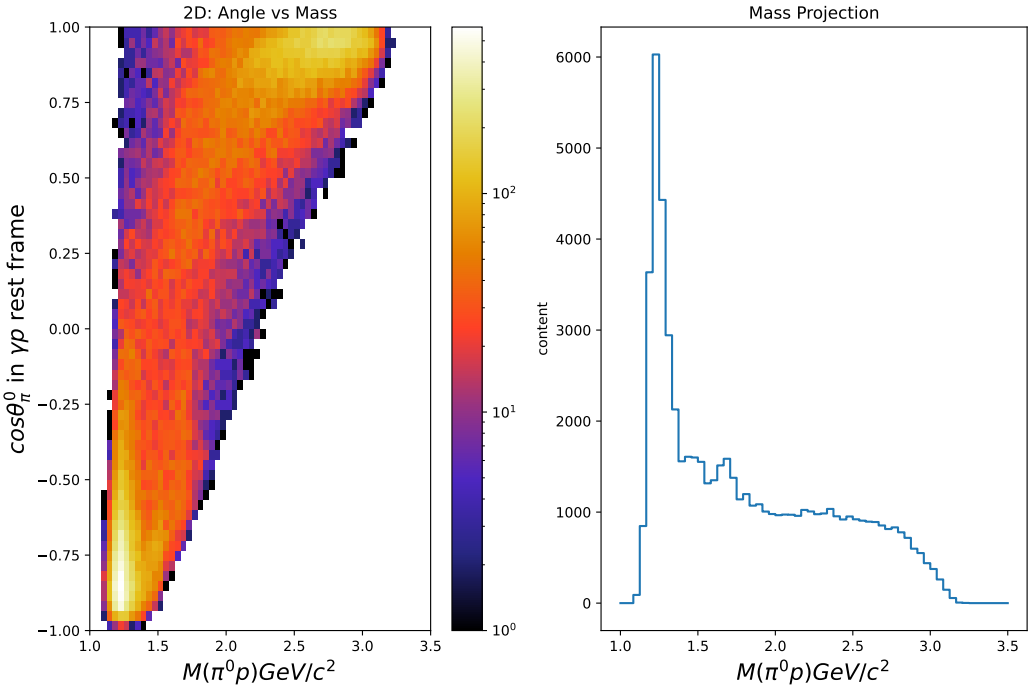

Fig. 3.11. $\cos\theta_{\pi^0}$ in γp rest frame vs $M(\pi^0 p)$ (left), projection of the left histogram on $M(\pi^0 p)$ axis (right)

In the histogram the forward going events near $\cos\theta \sim 1$ are nicely separated from the target excitation events in the backward angle $\cos\theta \sim -1$. Consequently a cut on angle, $cos\theta_{\pi^0} > 0$ was chosen. Figure 3.12 (left) shows the region that was rejected (top) and selected (bottom) and the corresponding η' signal. Clearly, the Δ^+ dominated region has a strong η' signal with much less background compared to the region of interest. This indicates that the reaction $\gamma p \to \eta' \Delta^+ p$ dominates the final state. About 43% probable $\gamma p \to \eta' \Delta^+ p$ events were rejected by this angle cut. Out of the remaining 57% of the events that pass this cut, the signal fraction for η' peak region estimated from a fit is about 0.58.

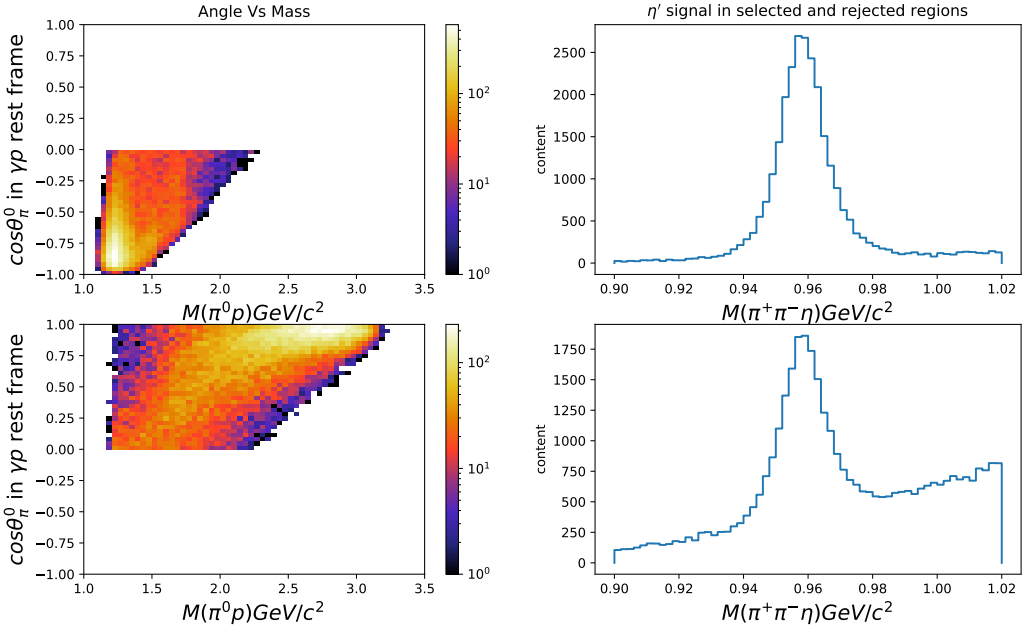

Fig. 3.12. Top left : rejected events dominated by Δ^+ peaks , bottom left : events outside the Δ^+ peaks, top right : η' signal for events dominated byΔ^+ region, bottom right : η' signal for the events outside Δ^+ region

3.3.3 The ω Background

Another important background identified in this channel is the ω (782) meson. Two different reactions could potentially dominate the contribution to the ω signal : 1. $\gamma p \rightarrow b_1 p$, where $b_1 \rightarrow \omega\pi^0$, and $\omega \rightarrow \pi^+\pi^-\pi^0$, 2. $\gamma p \rightarrow \omega\eta p$, where $\omega \rightarrow \pi^+\pi^-\pi^0$. Feynmann diagrams for these reactions are shown in left and right of fig. 3.8 respectively. Both of these channels have the same final state particles ($\pi^+\pi^-4\gamma$ p) as $\gamma p \rightarrow \eta'\pi^0 p$. However, the omega contribution from the b_1 will already have been addressed to a certain degree by the $\pi^0\pi^0$ rejection. The histogram in fig. 3.13 shows the $\pi^+\pi^-\eta$ invariant mass along y-axis vs the $\pi^+\pi^-\pi^0$ invariant mass along the x-axis. The ω signal is spread throughout the η' invariant mass region with its

strength increasing with increasing η' invariant mass. Projection onto the $\pi^+\pi^-\pi^0$ invariant mass shows a dominant ω signal in the right histogram. A narrow cut that rejects the events between the vertical red lines was consequently applied to exclude the omega background contributions.

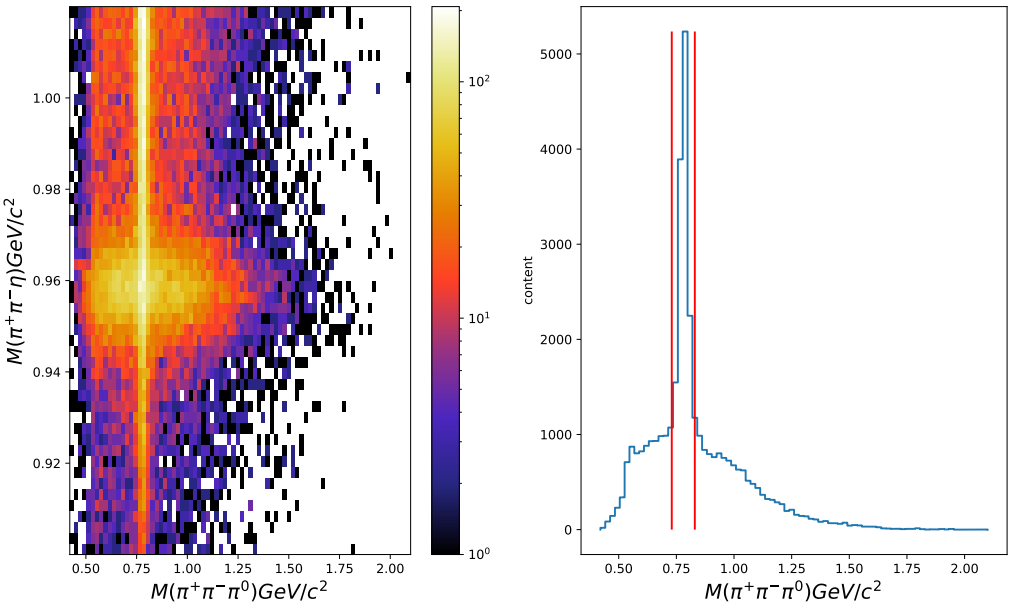

Fig. 3.13. Left : 2D histogram of $M(\pi^+\pi^-\eta)$ Vs $M(\pi^+\pi^-\pi^0)$, right : projection on $M(\pi^+\pi^-\pi^0)$, red vertical lines show the rejected mass window used for ω cut

Figure 3.14 shows the $\eta'\pi^0$ invariant mass and the effect of ω cut affects on this variable. The mass region between 1.3 GeV to 1.8 GeV, which is most affected by the cut is a crucial region for the possible exotic $\pi_1(1600)$ meson. A separate MC study was done that will be described in the next section to study the signal loss from this cut.

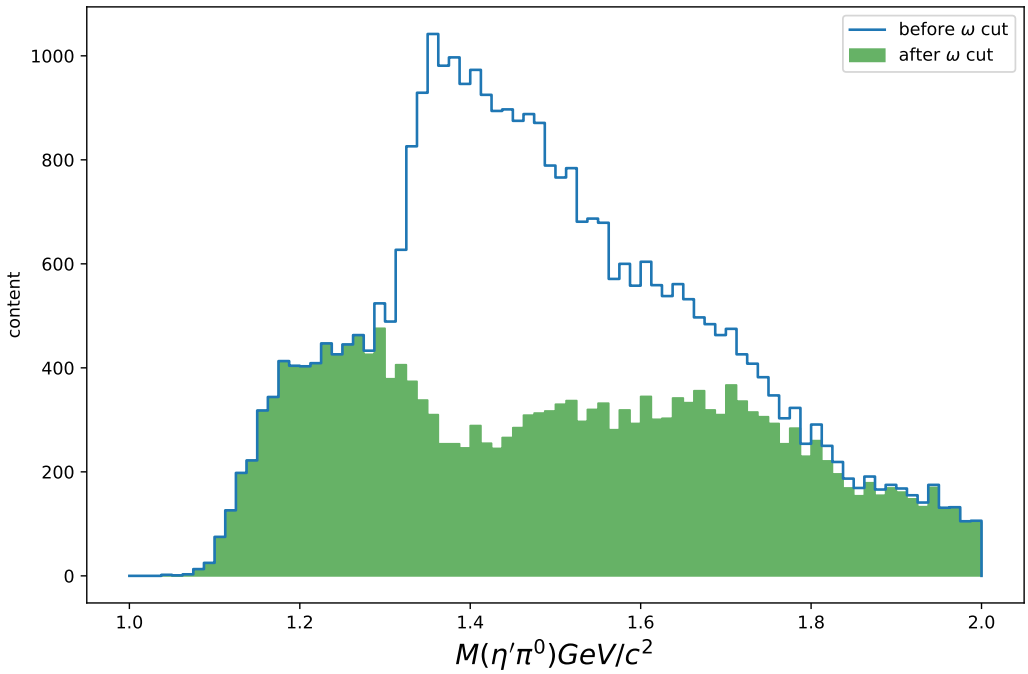

Fig. 3.14. Effect of ω cut on $M(\eta'\pi^0)$. The unfilled distribution is before the cut and the green distribution is after the cut. Significant loss of events around the $\pi_1(1600)$ mass region is seen.

3.3.4 Monte Carlo Study for the Omega Cut

Two different reactions were generated : $\gamma p \to \eta'\pi^0 p$ and $\gamma p \to \omega\eta p$. To make the Monte Carlo (MC) simulation more realistic, angular distributions in the form of D-waves namely $a_2(1320)$ and $a_2'(1700)$ were generated in the $\eta'\pi^0$ invariant mass distribution. Similarly, a P-wave corresponding to the $\Omega(1560)$ was generated for the $\omega\eta$ invariant mass distribution. Events thus generated were passed through GEANT4 and only the interested decay modes of the particles were employed to increase efficiency. The simulated final states would then be detected by the simulated GlueX detector. Both the generated channels were reconstructed as $\eta'\pi^0$ final states. Figure 3.15 shows the histogram of the reconstructed invariant mass of

the $\pi^+\pi^-\eta$ (left) and of the $\pi^+\pi^-\pi^0$ (right). The green distributions are the reconstructed $\eta'\pi^0$ events while the red distributions are the reconstructed $\omega\eta$ events from the $\omega\eta$ background generation. Approximately, less than a percent of the generated $\omega\eta$ were reconstructed as $\eta'\pi^0$ final state. The red distribution on right which is the pure ω signal shows up as the background underneath the η' signal on left.

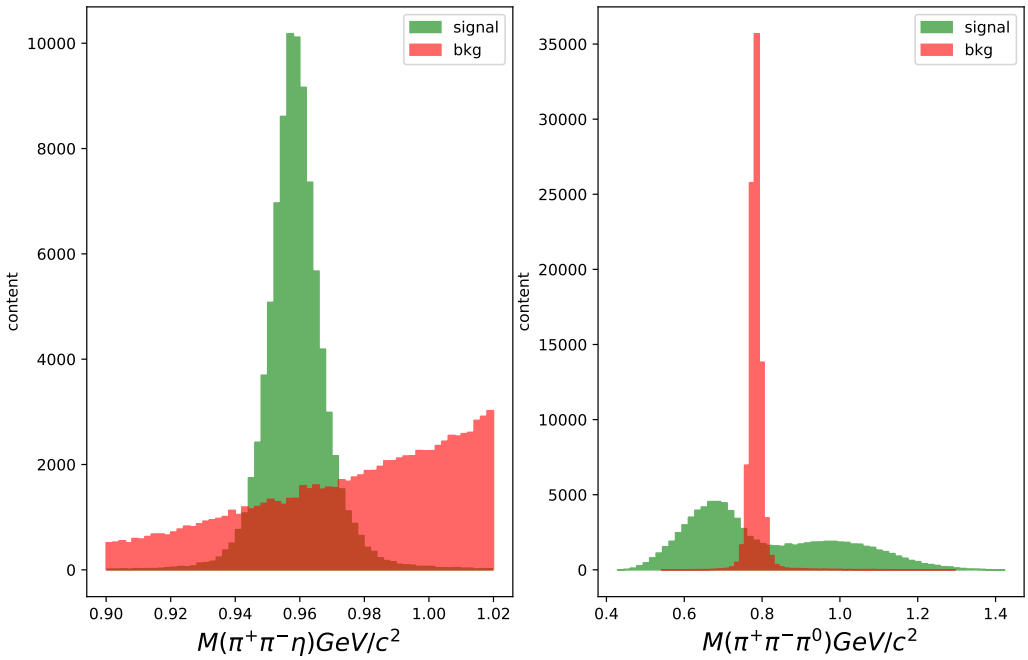

Fig. 3.15. Reconstructed events: $\pi^+\pi^-\eta$ invariant mass on left and $\pi^+\pi^-\pi^0$ invariant mass on right. Events for green distribution are from $\eta'\pi^0$ generation and events for red distribution are from $\omega\eta$ generation.

The same ω cut that was applied in the data set was tested for these samples. Figure 3.16 shows the $\eta'\pi^0$ invariant mass before and after the cut for both signal: $\eta'\pi^0$ and background: $\omega\eta$ channels. The cut does remove a significant background of about 98% along with signal loss of about 15%.

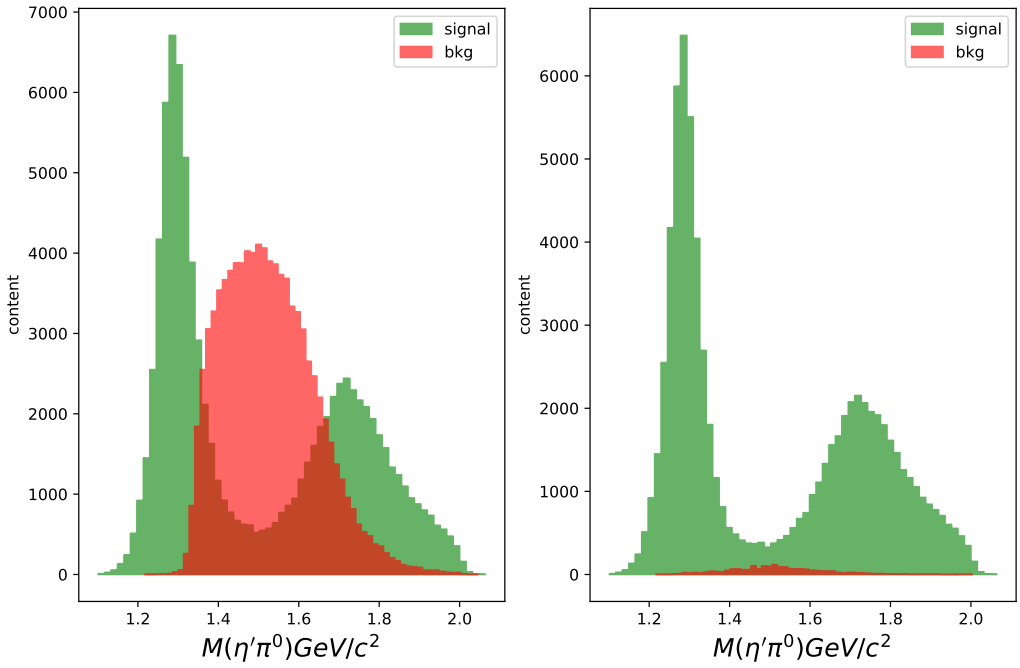

Fig. 3.16. $\eta'\pi^0$ invariant mass distribution for signal and bkg channels before (left) and after (right) the ω cut.

3.3.5 Bggen Monte-Carlo for Study of Background : Effect of $\pi^0\pi^0$ rejection box cut and the ω cut

Another way of evaluating the effects of the $\pi^0\pi^0$ rejection and the ω rejection is to study the bggen sample. Bggen is a PYTHIA [5] based Monte-Carlo event generator that is useful for background study. Out of multiple generated samples one can select a specific final state like the $\eta'\pi^0 p$ in this case. All batches of bggen-2017-01-ver03 and batches 1 and 2 of bggen-2018-01-ver02 from https://halldweb.jlab.org/wiki/index.php/Simulations were used to reconstruct the $\eta'\pi^0 p$ final state. Figures 3.17, 3.18 and 3.19 show 3 stacked histograms. The unfilled blue distribution is the total reconstructed $\eta'\pi^0$ invariant mass. Different colors indicate

the strength of the $\eta'\pi^0$ invariant mass contributions from different topologies that were accepted by the reaction filter contributed to the total histogram. The legend indicates the final states and the decay modes for heavier particles are shown inside the parenthesis. Figure 3.17 shows the stacked histogram without any rejection cut. The green topology which is the $\eta'\pi^0$ signal has a relative strength of about 59%. The yellow and black color distributions indicate the $\pi^0\pi^0$ and $\omega\eta$ channels. In this case a box cut was used to reject the $\pi^0\pi^0$ events because of technical reasons. Box cut means if an event lies in the window of $0.11 < M(\gamma\gamma)\mathrm{GeV/c^2} < 0.17$ in the 2D histogram of $M(\gamma_1\gamma_3)$ Vs $M(\gamma_2\gamma_4)$ OR $M(\gamma_1\gamma_4)$ Vs $M(\gamma_2\gamma_3)$ along both horizontal and vertical directions, then the event is rejected. The box cut is probably slightly inefficient compared to the actual polygon cut used in the data. This cut removes a significant fraction of the yellow topology $\pi^0\pi^0$ events that mainly populate the threshold energy region. This can be seen in fig. 3.18. The $\omega\eta$ channel (black topology) mainly populates the mass region that is close to the possibly exotic $\pi_1(1600)$ region with significant strength. The ω cut ($0.73 < M(\pi^+\pi^-\pi^0)\mathrm{GeV/c^2} < 0.83$) removes a good fraction of the these events which can be seen in fig. 3.19.

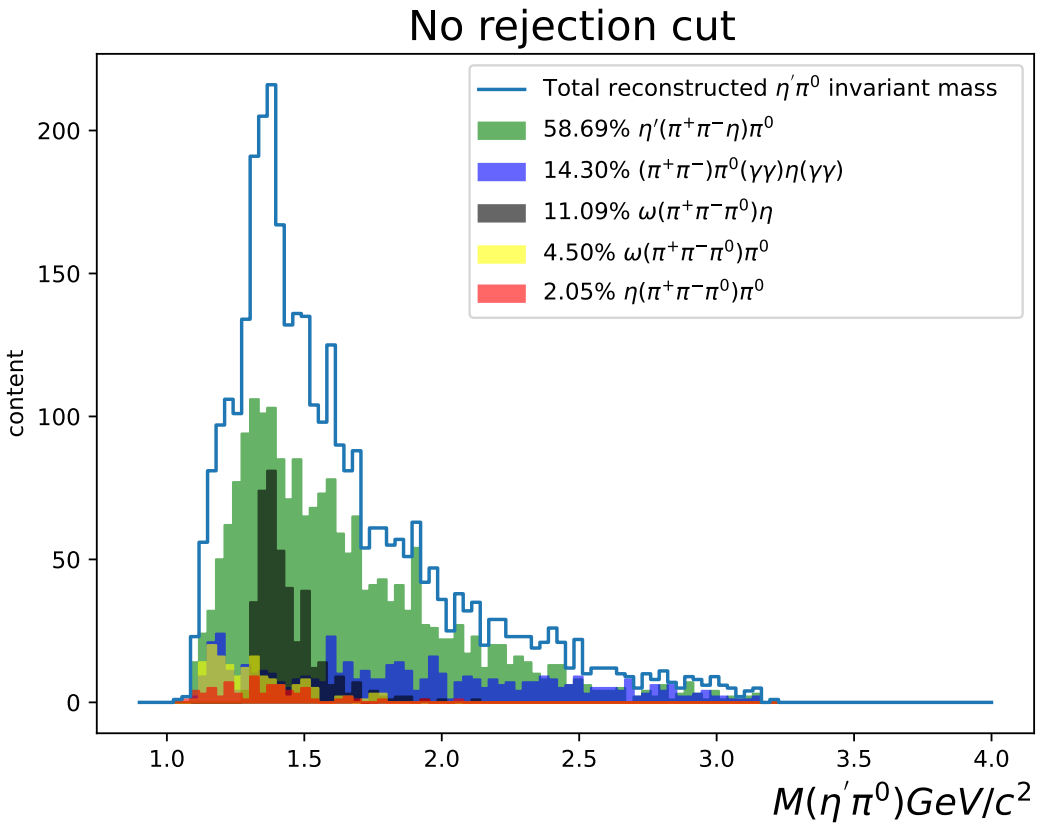

Fig. 3.17. Bggen stacked histograms for $\eta'\pi^0$ invariant mass with no $\pi^0\pi^0$ or ω cut. Different topologies are shown in different colors and their relative strengths percentages are shown in legend.

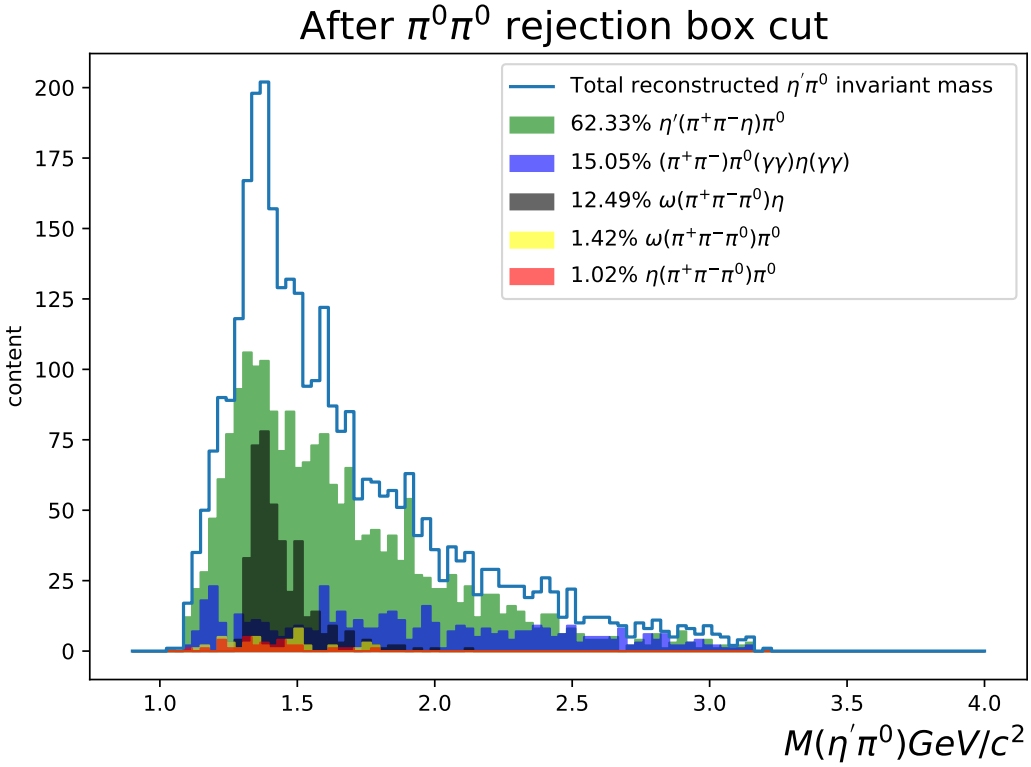

Fig. 3.18. Bggen stacked histograms after $\pi^0\pi^0$ rejection box cut

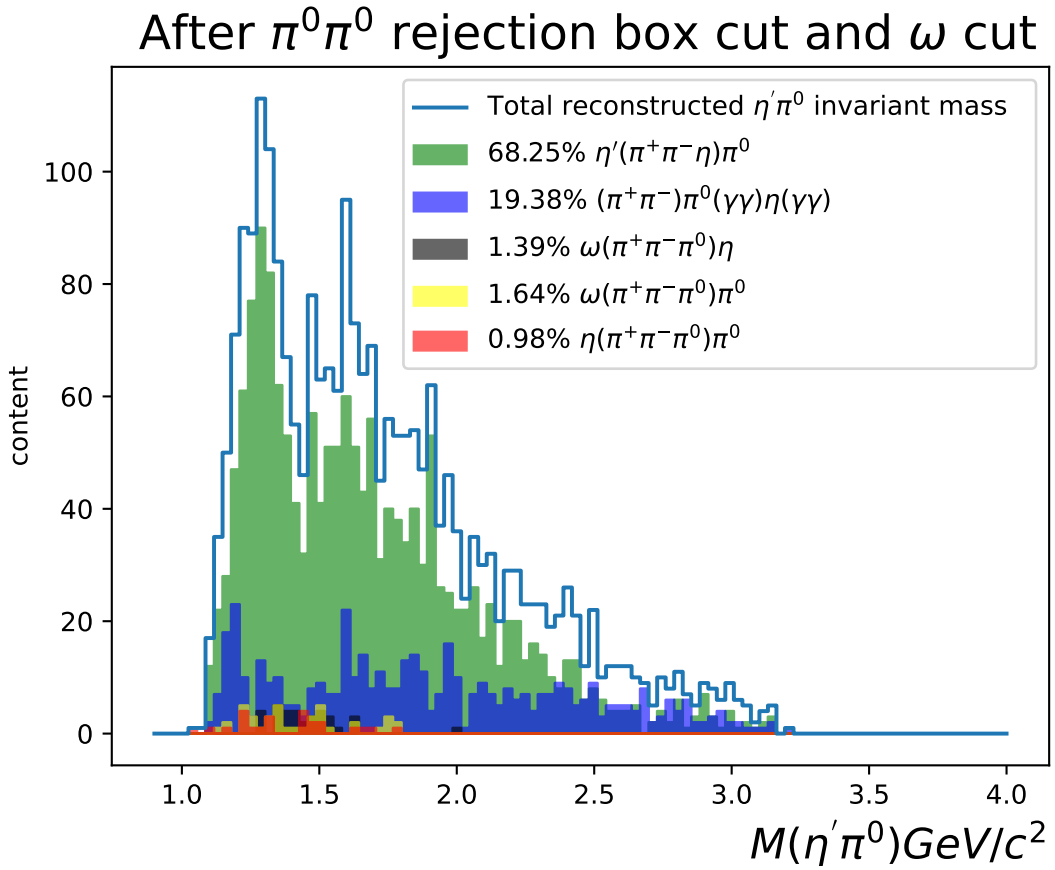

Fig. 3.19. Bggen stacked histograms after rejection $\pi^0\pi^0$ box cut followed by an ω cut

3.4 Duplicate Events

The central peak in the timing distribution in section 3.2.2 has multiple beam photons final state particle combinations (combos) from the same event that pass all analysis cuts. The source of multiple combos could either be (a) the same trigger for multiple tagger hits , mainly because the GlueX tagger is not 100% efficient (section 3.2.2) or (b) multiple triggers for same tagger hit. A further selection of unique events within this central peak in timing distribution was done by the following method. Each unique event is identified by a (run number, event number) pair.

If more than one combo is found to have the same (run number, event number) pair, they were rejected. For the current analysis, about 22% of such combos were identified and rejected.

3.5 Background Subtraction

3.5.1 Sideband Subtraction

The classical approach to sideband subtraction is based on the assumption that a peak sits on top of a smoothly varying linear background. In this case, after all event selection and rejecting possible alternate channels, the $\pi^+\pi^-\eta$ invariant mass in fig. 3.20 shows a blue distribution with a peak at around $0.96\,\mathrm{GeV/c^2}$ which is the η' signal. The peak sits on a smooth background that is approximately linear. The following discussion describes the equations used to do a sideband subtraction.

Consider two points in a line (x_l, y_l) and (x_r, y_r). Any point (x_b, y_b) lying on the same line can be written as

$$y_b - y_l = \frac{(y_r - y_l)}{(x_r - x_l)}(x_b - x_l) \tag{3.3}$$

For simplicity, let

$$f = \frac{(x_b - x_l)}{(x_r - x_l)} \tag{3.4}$$

In case of a 1D histogram, x and y are the bin centers and bin contents respectively. If y_i is the average yield per bin in a sideband, then the total yield would be

$$Y_i = N_i y_i \tag{3.5}$$

where N_i is the number of bins in the sideband region. Hence, if y_b and N_b are average yield per bin and number of bins in the signal region then,

$$Y_b = N_b y_b \tag{3.6}$$

is the total background yield where y_b is estimated using sideband regions located to the left and right of the peak. Using equations 3.4 , 3.5 and 3.6, in equation 3.3, one can write

$$Y_b = (1 - f)\frac{N_s}{N_l}Y_l + f\frac{N_s}{N_r}Y_r \tag{3.7}$$

This is the general case. In case of equal number of bins and equal band widths $N_r = Ns = N_l$ and $f = \frac{1}{2}$, equation 3.7 is just a mid-point approximation in between a line.

Three different windows : (a) the peak region (in between red lines in fig. 3.20) $0.94 < M(\pi^+\pi^-\eta)\,\mathrm{GeV/c^2} < 0.98$, b. left sideband region (in between black lines on left) $0.90 < M(\pi^+\pi^-\eta)\,\mathrm{GeV/c^2} < 0.93$ and (c) right sideband region (in between black lines on right) $1.00 < M(\pi^+\pi^-\eta)\,\mathrm{GeV/c^2} < 1.02$ are chosen. Interpolating the shape in the peak region from sidebands gives a linear background shown by orange distribution in figure 3.20. It is subtracted from the total (blue distribution) to get a background corrected (green distribution) distribution based on the sideband method.

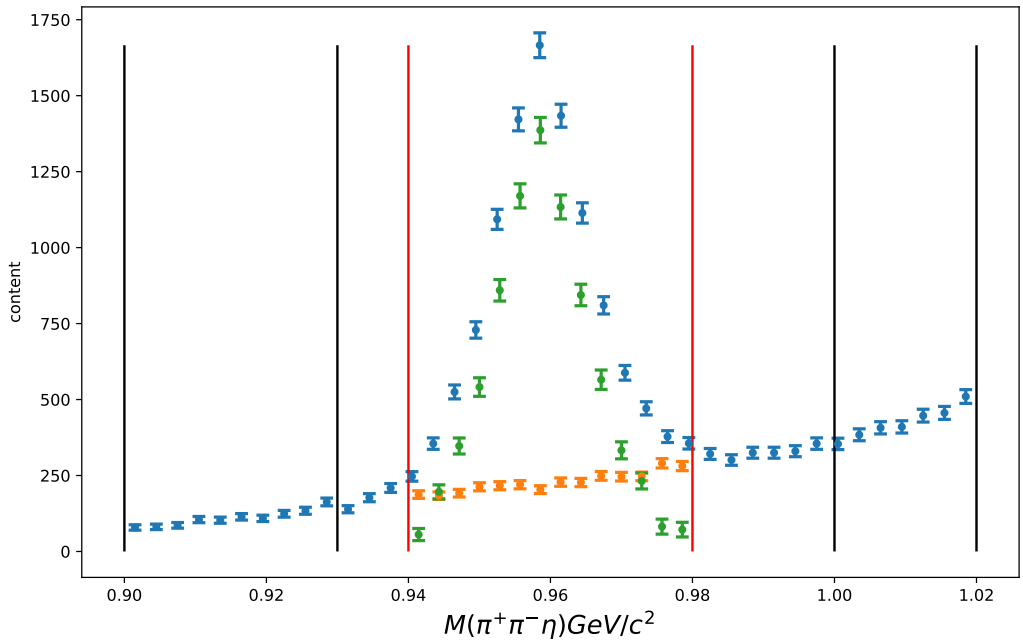

Fig. 3.20. Three different windows chosen were for sideband subtraction, red vertical lines indicate the peak window, black vertical lines are the sideband windows. In the peak region background estimate from the sidebands is shown in orange, and corrected distribution is shown in green.

Ideally the resonances corresponding to different quantum mechanical waves will show symmetries (figure 1.7) along the $cos\theta_{GJ}$, where θ_{GJ} is the angle discussed in the figure 1.8 in chapter 1. In figure 3.21 below, the top histogram shows the $cos\theta_{GJ}$ angle of the decaying η' Vs $M(\eta'\pi^0)$ in the peak region and the bottom shows the sideband corrected histogram. The $cos\theta_{GJ}$ is the cosine of the Gottfried-Jackson angle described in fig. 1.8. No such symmetries are obvious along the angular distribution in the histogram.

Figure 3.22 shows the projection on the $M(\eta'\pi^0)$ axis. An enhancement near threshold ($1.27\,\mathrm{GeV/c^2}$) is seen. A second enhancement of less strength follows at around ($1.7\,\mathrm{GeV/c^2}$). The data here includes the ω cut. The structures might be artefacts of the acceptance. An acceptance correction will be discussed later.

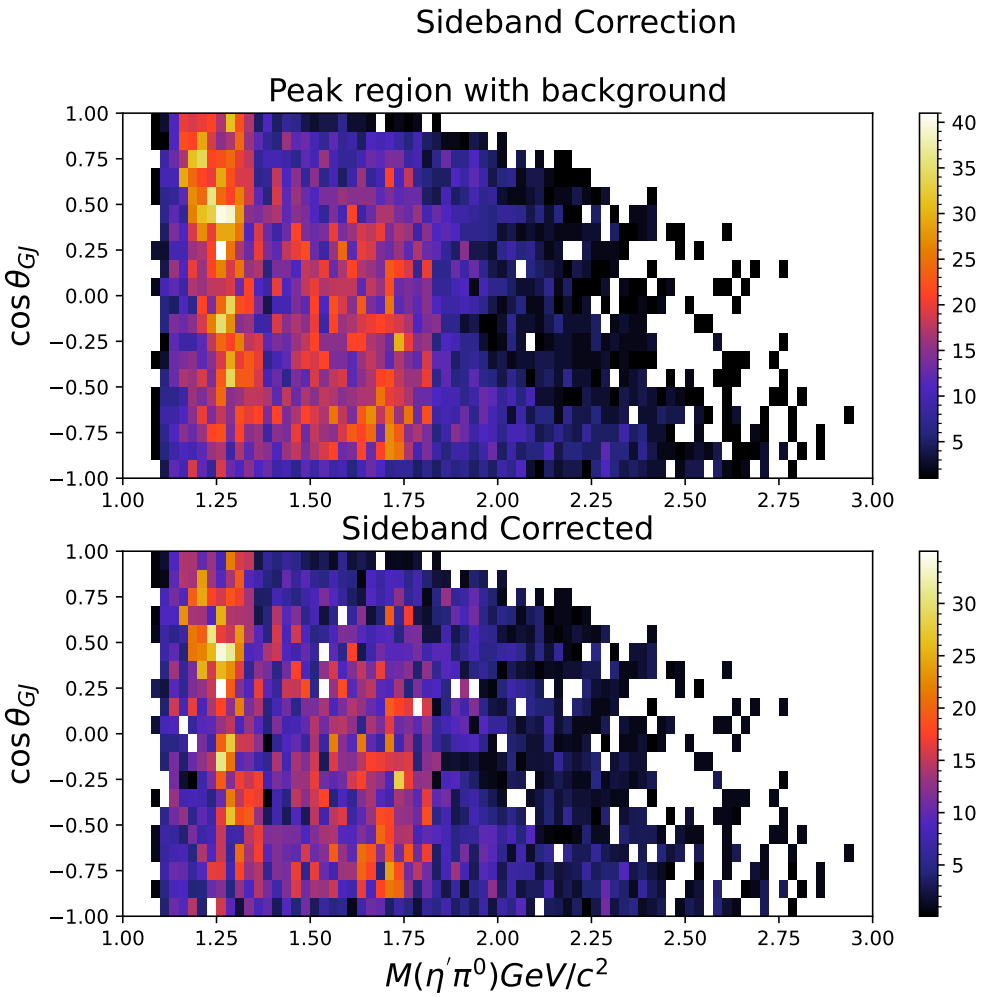

Fig. 3.21. $cos\theta_{GJ}$ Vs $M(\eta'\pi^0)$. Left : η' peak region with background, right : sideband corrected for η' peak region. No noticeable symmetries can be identified along the $cos\theta_{GJ}$ axis.

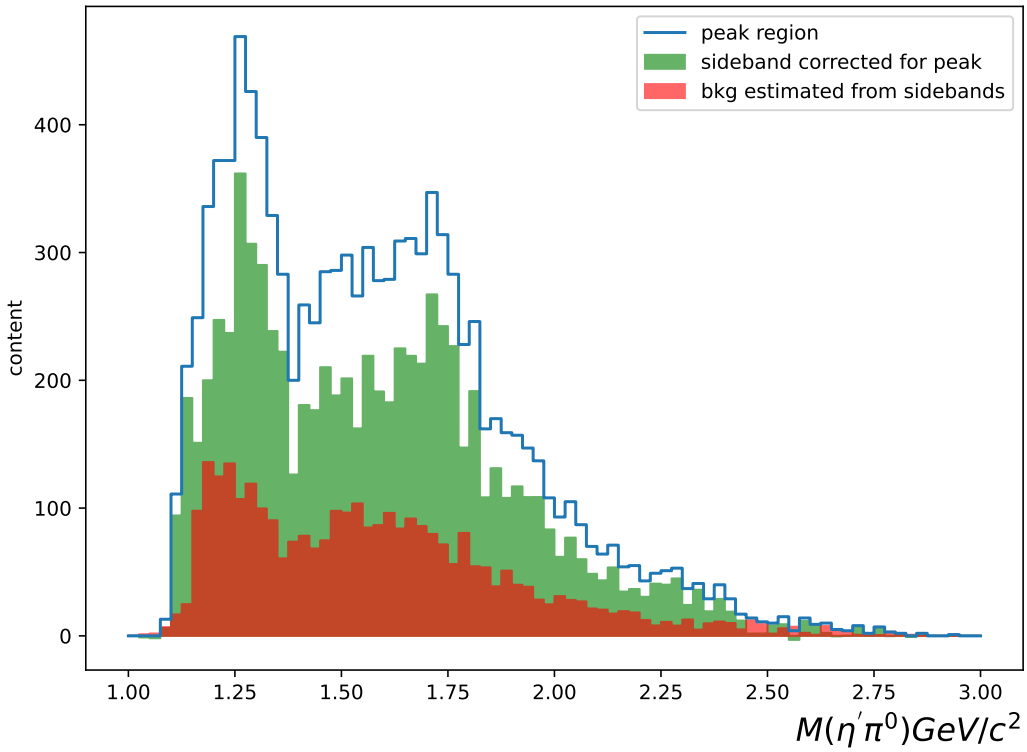

Fig. 3.22. $M(\eta'\pi^0)$ for peak region, sideband region and sideband corrected for peak region of η' signal. No significant difference in shape is observed for signal and background region.

3.5.2 Probabilistic weighing on an event-by-event basis : Q-factors

An alternate approach to background subtraction is the probabilistic approach [6]. This is a sophisticated and computationally expensive method since it works at the level of each event unlike sideband subtraction method where background separation is carried out at the level of histograms.

We start by selecting a region of phase space volume element around the location of the current event. In our case, we chose the cosine of the polar angle $cos\theta_{GJ}$ and

the azimuthal angle ϕ_{GJ} of the decaying η' as the discriminating variables. By discriminating, we mean the η' signal-background varies in different regions of the chosen variable. The assumption is that the background shape and signal size might vary depending on where the event lies in terms of these angles. For simplicity, the subscript GJ is dropped hereafter. The angles used are always in the Gottfried-Jackson frame unless mentioned explicitly. A metric d_{ij} for the distance between two events is defined based on these angles between any two events, as

$$d_{ij} = \sqrt{d_n \phi_{ij}^2 + d_n \cos\theta_{ij}^2} \tag{3.8}$$

This is an euclidean distance between two events i and j based on their separation on these angles. $d\phi_{ij}^2$ and $d\cos\theta_{ij}^2$ are calculated as

$$d\phi_{ij}^2 = (cos\phi_i - cos\phi_j)^2 + (sin\phi_i - sin\phi_j)^2 \tag{3.9}$$

$$d\cos\theta_{ij}^2 = (cos\theta_i - cos\theta_j)^2 \tag{3.10}$$

Equations 3.9 and 3.10 are normalized by the maximum possible distance between events i and j in terms of the quantities the distance is defined. The normalization ensures equal weight is assigned to each discriminating variable. In case of $cos\theta$, it's range is (-1,1) so the maximum distance is 2. So, the normalized distance is

$$d_n \cos\theta_{ij}^2 = \frac{d\cos\theta_{ij}^2}{4} \tag{3.11}$$

and similarly for ϕ,

$$d_n \phi_{ij}^2 = \frac{d\phi_{ij}^2}{8} \tag{3.12}$$

The ϕ angle has normalization factor of 1/8, because it has 2 terms, one of $cos\phi$ and the other $sin\phi$. For each event i, the distance d_{ij} is then calculated with every other event j where $\sum j$ = total number of events - 1. Based on the metric d_{ij}, the N_h nearest neighbor events ($N_h = 400$ in our case) for each event i are selected and divided into 20 bins of $\pi^+\pi^-\eta$ invariant mass. The number of nearest neighbors is somewhat arbitrary. If the number is too big, the phase space areas for different events will have a reduced sensitivity to the dependence on the background. On the other hand N_h has to be large enough to obtain a good fit. Different numbers of neighboring events N_h 800, 600, 400, 200 were tried and no noticeable difference was observed in the q-factor weighted $\pi^+\pi^-\eta$ invariant mass distribution. For each event the chosen invariant mass spectrum for the N_h events in its neighborhood is then fitted by sum of a Gaussian signal with a linear background. The parameter estimation was done by χ^2 minimization. The total fit function is then used to calculate the probability (q value) which gives the relative strength for the event to be a signal or a background. This is then repeated for every event in the sample and for each event a q value is extracted. The details showing the calculation are described below.

We define a total function as,

$$F = Aexp\frac{-(x-\mu)^2}{2\sigma^2} + a_0 + a_1 x \tag{3.13}$$

Here, A, μ, σ represent the amplitude, position and width of the Gaussian signal and x is the variable one is interested to fit, in this case it is $\pi^+\pi^-\eta$ invariant mass. And a_0 and a_1 are the coefficients of the linear background.

The function F is then fitted to the $\pi^+\pi^-\eta$ invariant mass distribution chosen based on the nearest neighbors. Fit parameters A, μ, σ, a_0, a_1 were estimated using minimization of χ^2. The q-factor for the event is then calculated as the signal

strength divided by the total strength. Q-factors can only have a physical meaning in the range (0,1), where 0 indicates a pure background event while 1 indicates a pure signal event.

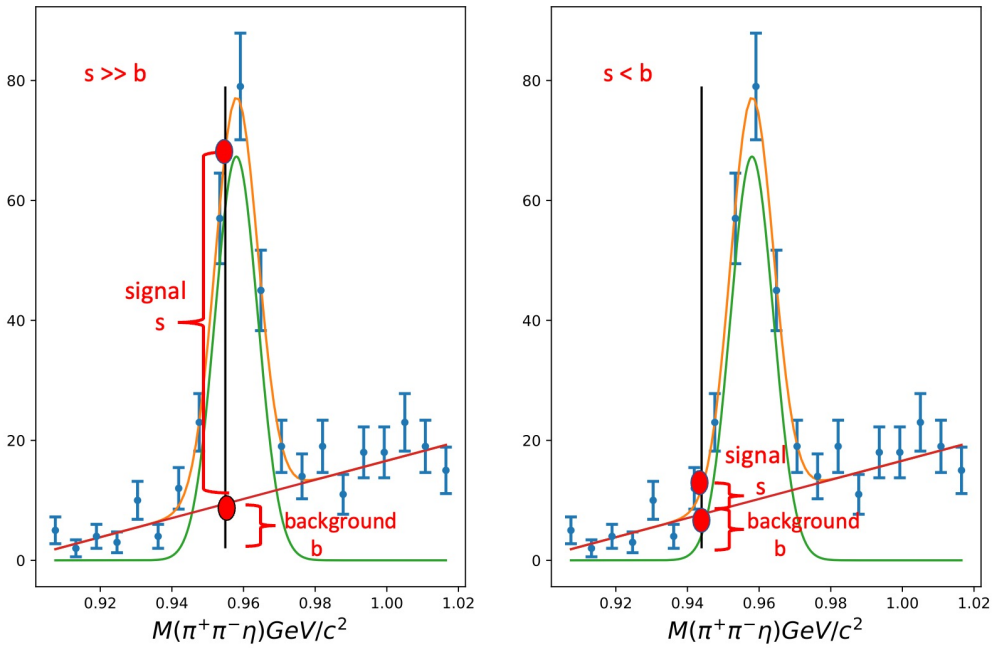

Fig. 3.23. Sample fits for q-factor determination. Left : A high q-factor of about 0.86 for mass at around 0.954 $\mathrm{GeV/c^2}$ (vertical black line). Right : A relatively low q-factor of about 0.35 for mass at around 0.943 $\mathrm{GeV/c^2}$

Figure 3.23 shows two such sample fits. The blue points are the data chosen from the nearest neighbors for the particular event and divided into 20 bins . The green, red and orange distribution shows the signal, background and total fit functions. The black vertical line shows where the current event lies in the invariant mass spectrum. Although the 2 histograms and their fits look similar, since the current invariant mass lies far left from the peak in the right histogram, it's q-value is at around 0.35, while for the left histogram the q-value is at around 0.86. The values suggest that the current event for right case has a 35% probability for being a signal event while for left case it has an 86% probability for being a signal event. The fits

are done for all events and each event will thus have a q-factor associated with it. Figure 3.24 shows $\pi^+\pi^-\eta$ invariant mass distribution and its shape when weighted by signal (q) and background (1-q) probabilities. A total of about 7900 events are in the signal (q) weighted distribution. The shapes, in general, matched with the signal and background shapes used for each fit.

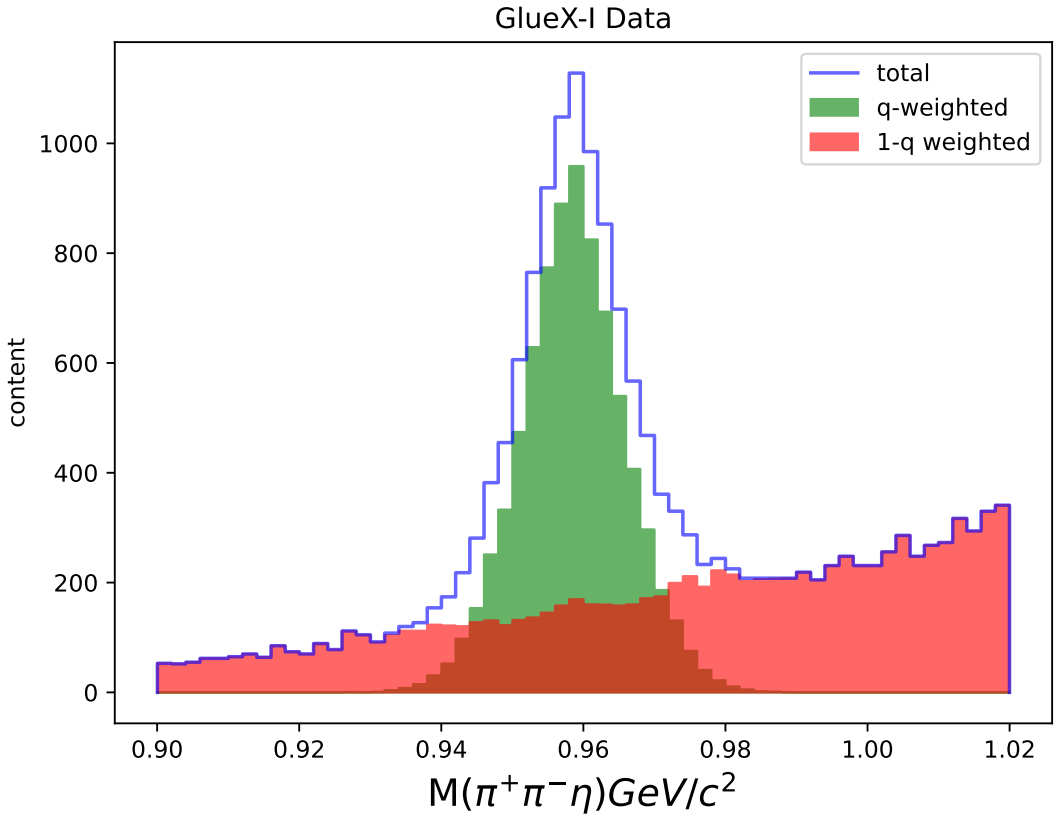

Fig. 3.24. $\pi^+\pi^-\eta$ invariant mass spectrum. The blue is the total distribution, the green and red are the signal and background distributions

Figure 3.25 shows a comparison of the background separation using the two different methods. The 2D histograms show the $cos\theta_{GJ}$ as a function of the $M(\eta'\pi^0)$ between 1 to 2 GeV. The top histogram is sideband corrected and the bottom one is q-factor weighted. Figure 3.26 shows the $\eta'\pi^0$ invariant mass for two methods. The

distributions are not identical but in general there is good agreement between the two methods.

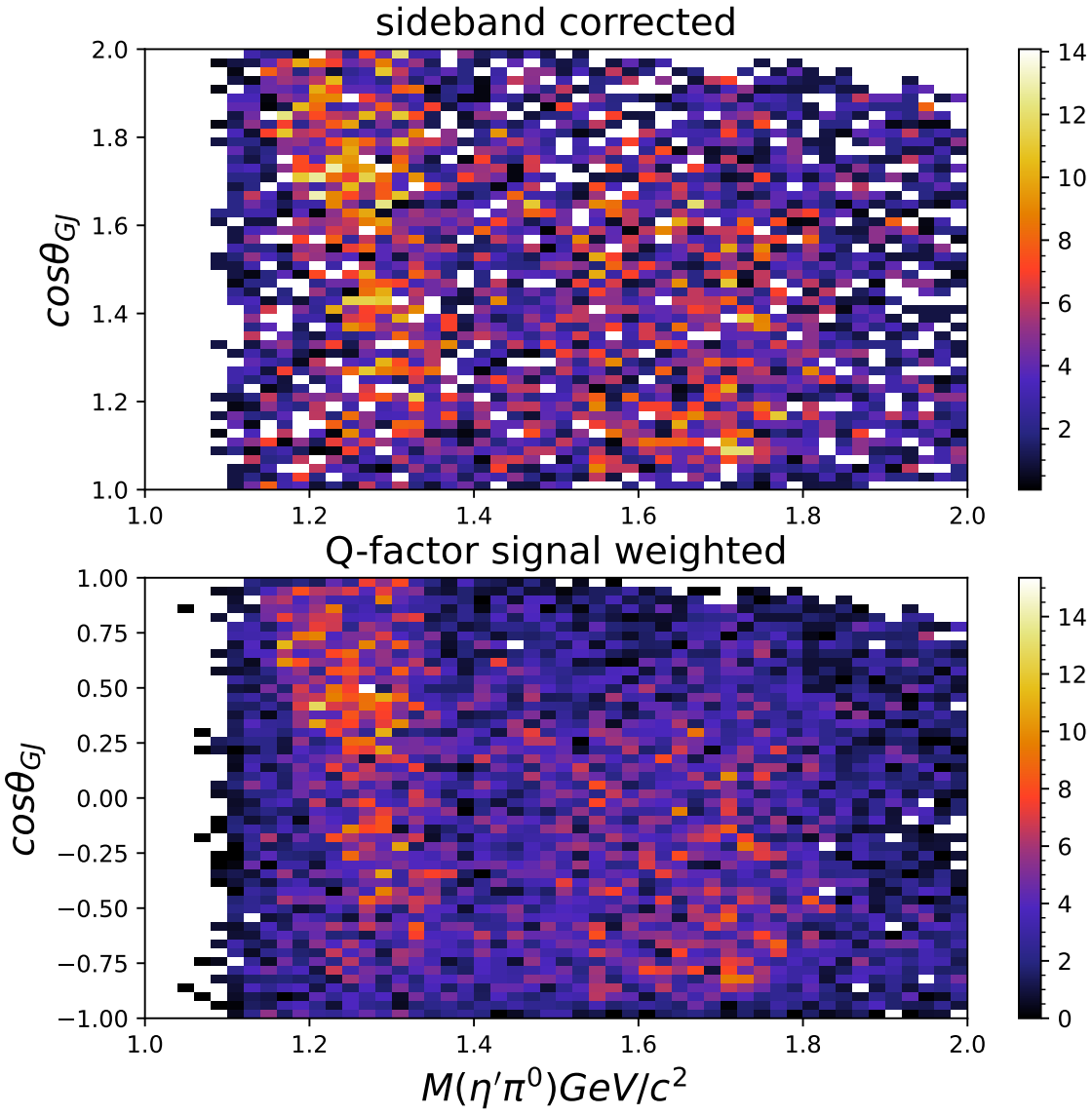

Fig. 3.25. $cos\theta_{GJ}$ as a function of $M(\eta'\pi^0)$; Top : Sideband corrected, Bottom: Q-factor signal weighted.

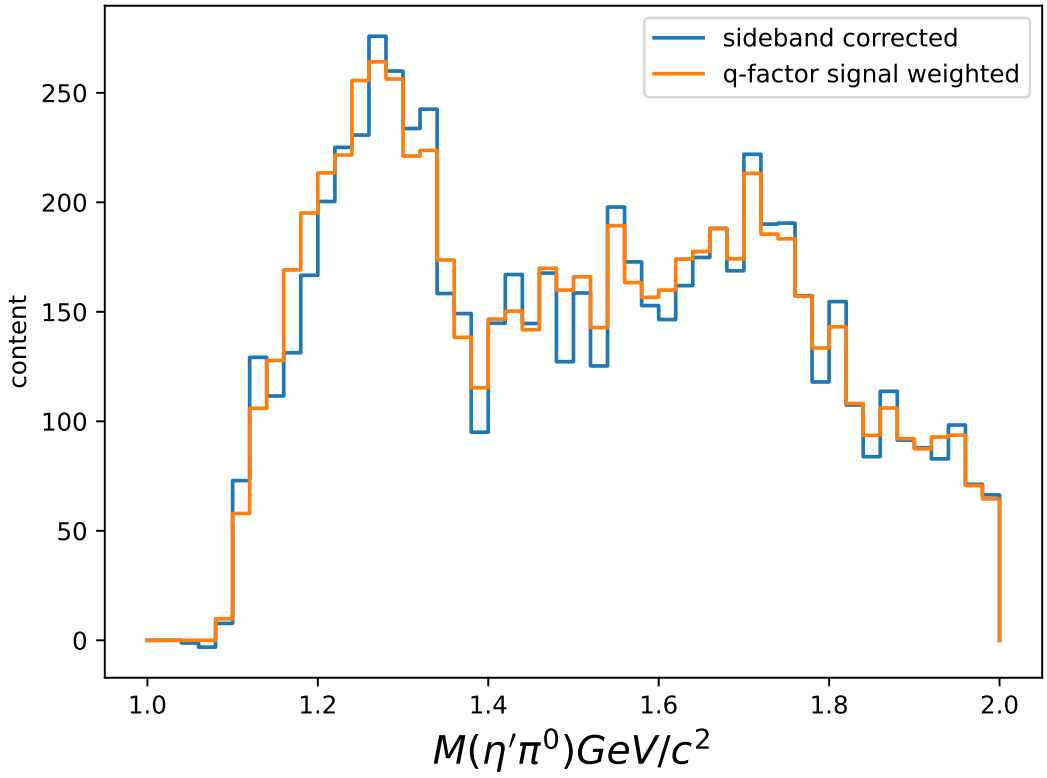

Fig. 3.26. $\eta'\pi^0$ invariant mass comparison for two different signal to background separation methods. In general, a good agreement is seen.

Figure 3.27 shows the difference between the two methods along Y-axis as a function of the $M(\eta'\pi^0)$.

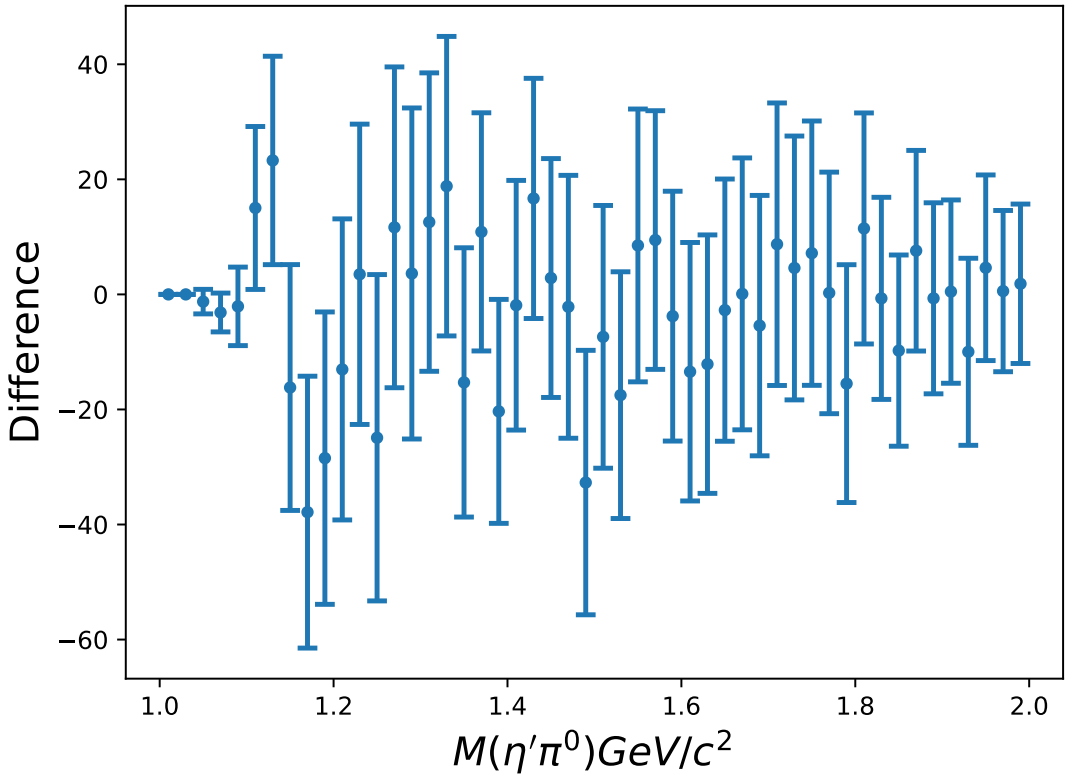

Fig. 3.27. Difference between the sideband and the q-factor method.

This q-factor method was also tested in the MC sample mentioned in section 3.3.4 after an ω cut. In figure 3.28 (left), the blue unfilled distribution is the sum of true signal and true background events. A similar q-factor method is applied to this sample. The signal shape couldn't be described by a simple Gaussian as in the data, and so an empirical signal distribution was used. This shape was then combined with a linear background to construct a total fit function. For each event, a fit was done and q-factor was calculated. Only the signal size and its position was allowed to vary during the fit. The right histogram in fig. 3.28 shows the signal and background distribution after weighing by the corresponding q-weights. The left histogram in fig. 3.29 shows the true signal and the q-weighted distribution while

the right shows the true background and the 1-q weighted distributions. In general, a good agreement is seen in the two histograms. The right histogram shows a more bin-by-bin fluctuation for true background distribution while the 1-q weighted distribution looks more smooth.

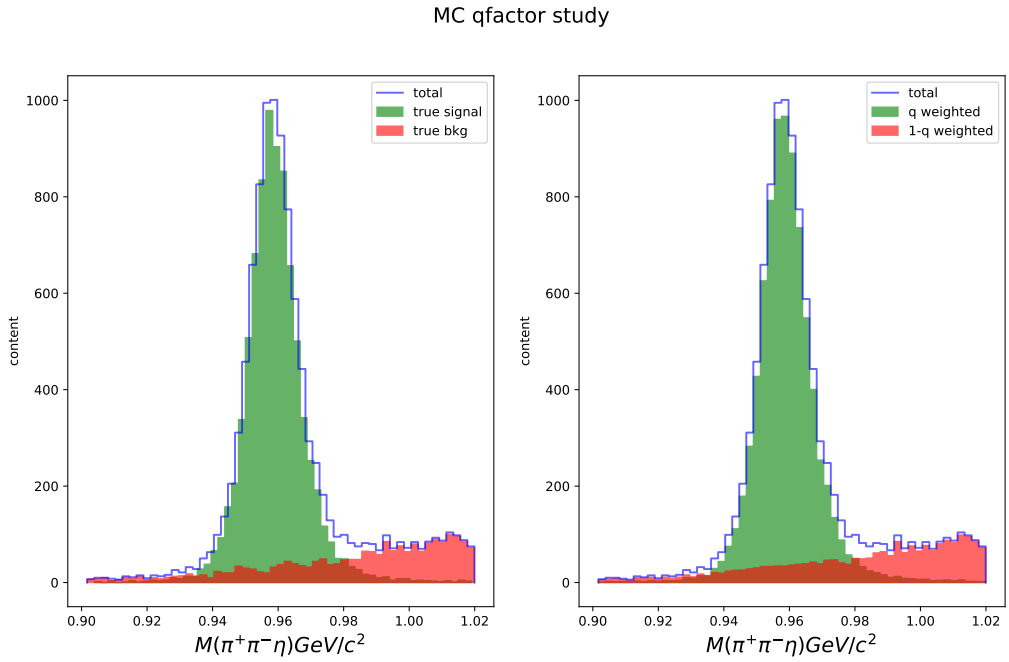

Fig. 3.28. Q-factor study for MC. Histograms show the $\pi^+\pi^-\eta$ invariant mass, the true signal and background MC (left) and the q-factor separated signal and background MC (right).

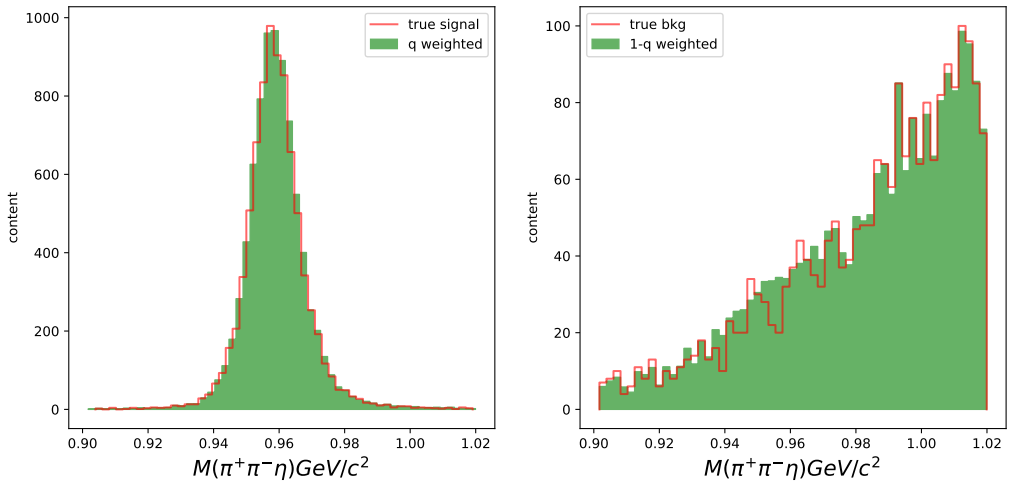

Fig. 3.29. Q-factor study for MC. True signal compared with q-factor separated signal events (left) and true background compared with the q-factor separated background events (right).

Figure 3.30 shows that the agreement is good for the $\pi^+\pi^-\eta$ invariant mass (left) but we see a clear discrimination between the true Monte-Carlo and the q-factor separated signal events in the $\eta'\pi^0$ invariant mass distribution (right).

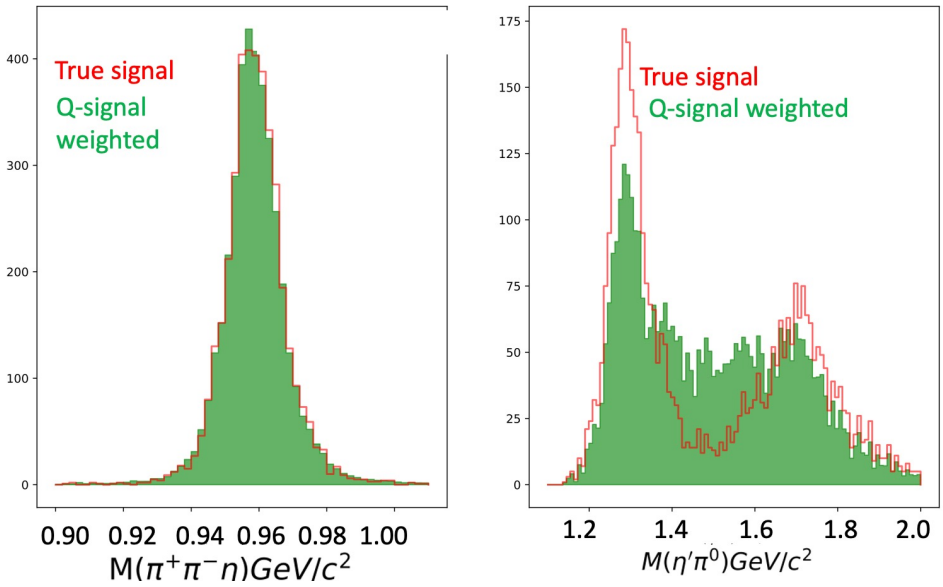

Fig. 3.30. Q-factor study for MC. The $\pi^+\pi^-\eta$ invariant mass agrees for the true MC and the q-factor separated signal events. But the $\eta'\pi^0$ invariant mass shows discrepancy for the two distributions.

Figure 3.31 compares the true signal Monte-Carlo with the sideband subtracted $\eta'\pi^0$ invariant mass distribution and the q-factor separated events. Clearly the sideband method shows much better agreement with the true Monte-Carlo distribution.

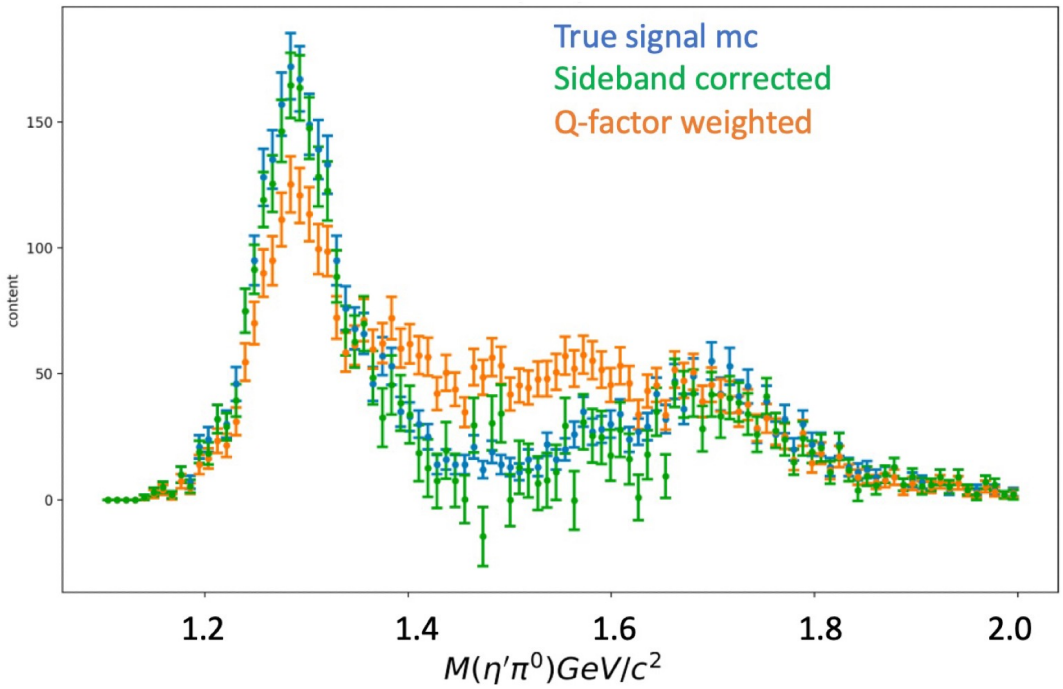

Fig. 3.31. Q-factor and sideband comparison. Sideband matches the true MC. Q-factor fails to match the true MC.

In order to correct for this, we included the $\eta'\pi^0$ invariant mass along with the $cos\theta_{GJ}$ and ϕ_{GJ} in the set of discriminating variables. The q-factor separated signal events show a much better agreement with the true Monte-Carlo (fig. 3.32) after including the $\eta'\pi^0$ invariant mass variable. The conclusion from this Monte-Carlo q-factor study is that if the η' signal and background varies along a variable, $\eta'\pi^0$ invariant mass in this case, and if the variable is not a part of the phase space volume element where q-factor fits are performed then the q-factor method can't correctly reconstruct the corresponding shape i.e. $\eta'\pi^0$ invariant mass.

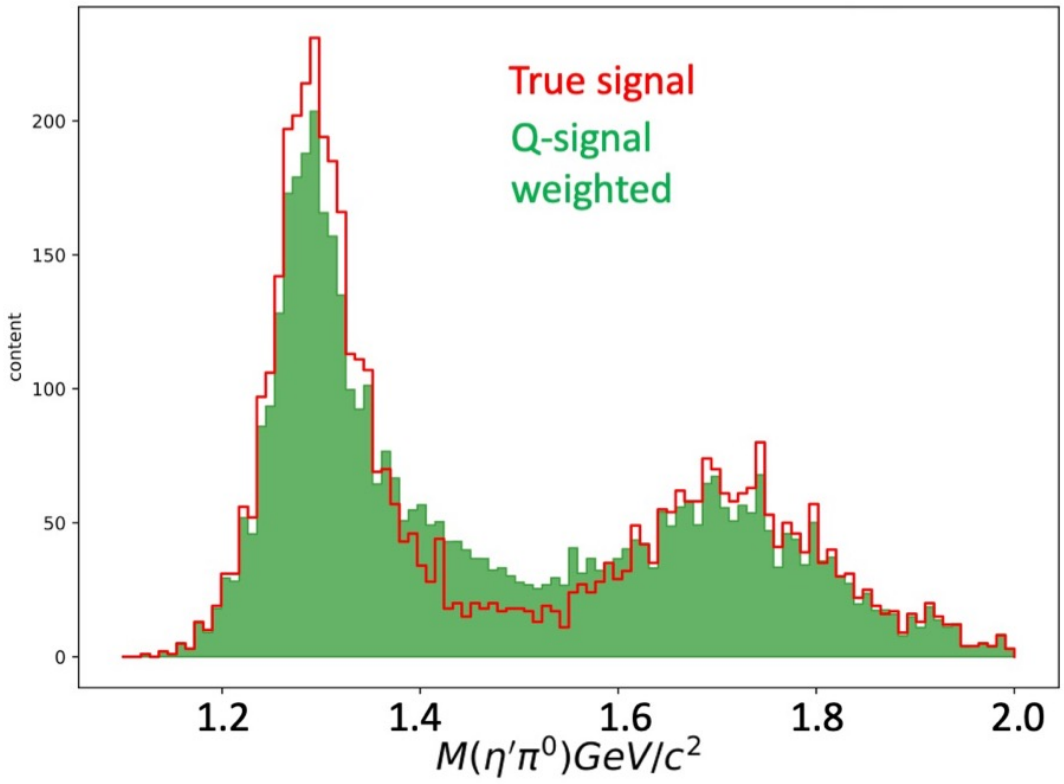

Fig. 3.32. Q-factor study for MC. Adding the $\eta'\pi^0$ invariant mass in the set of discriminating variables in q-factors analysis seems to better reconstruct the correct shape.

In data, two separate q-factor analysis were performed with different sets of discriminating variables. In one set, we use the helicity angles $cos\theta_{HX}$ and ϕ_{HX} and in the other set we use $\eta'\pi^0$ invariant mass in addition to the two angles. Figure 3.33 compares the $\eta'\pi^0$ invariant mass distributions for these two analyses. A very good agreement is seen implying that the η' signal and background doesn't vary within the $\eta'\pi^0$ invariant mass. This might be an indication of a phase space with no signal in the $\eta'\pi^0$ invariant mass.

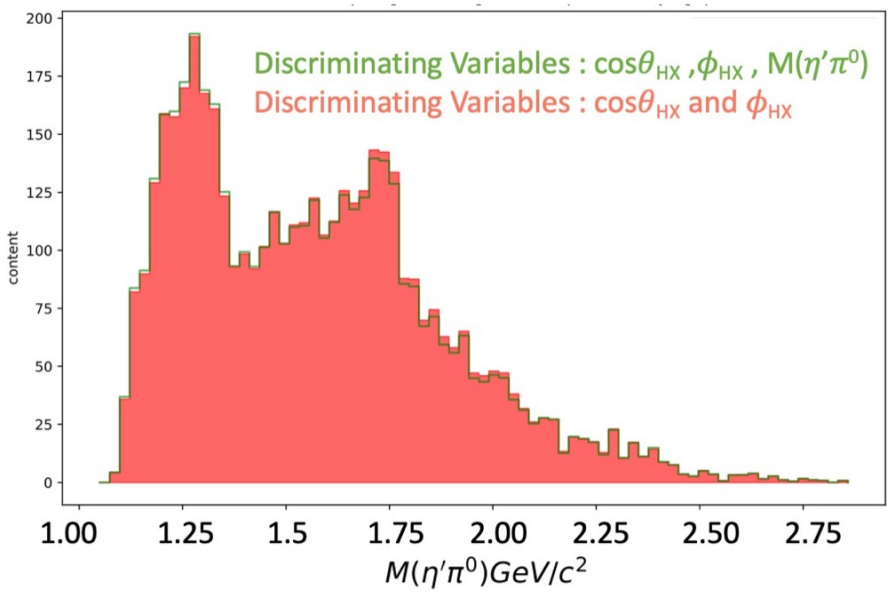

Fig. 3.33. Q-factors separated signal events for GlueX-I data. Adding the $\eta'\pi^0$ invariant mass in the set of discriminating variables in the q-factors study makes no real difference for the q-factor separated $\eta'\pi^0$ invariant mass.

3.5.3 Acceptance Correction

A flat phase space Monte-Carlo (MC) sample of $\eta'\pi^0$ was generated in the energy range $(8.2, 8.8)\,\mathrm{GeV/c^2}$ to study the effect of cuts on the acceptance using simulation. Here flat means flat in $cos\theta_{GJ}$ and $M(\eta'\pi^0)$. Neither any waves in angular distribution nor resonances were used. The generated events were then passed through the GlueX detector and reconstructed. The same cuts were applied to these reconstructed MC events for the GlueX-I data events. The events that pass these cuts are the accepted MC events. One can then study the $cos\theta_{GJ}$ as a function of the $\eta'\pi^0$ invariant mass for both generated and accepted MC. Figure 3.34 shows the acceptance in $cos\theta_{GJ}$ and $M(\eta'\pi^0)$. It corresponds to the ratio of the accepted histogram to the generated histogram. A low acceptance is seen at around $1.4\,\mathrm{GeV/c^2}$ due to

the ω cut. The left histogram in fig. 3.35 is the $\eta'\pi^0$ invariant mass for GlueX-I dataset weighted by signal probabilities but is not corrected for acceptance, where as the right histogram is corrected for acceptance. A noticeable feature from these two histograms is that the peak followed by a dip below $1.4\,\mathrm{GeV/c^2}$ is eliminated after an acceptance correction is done.

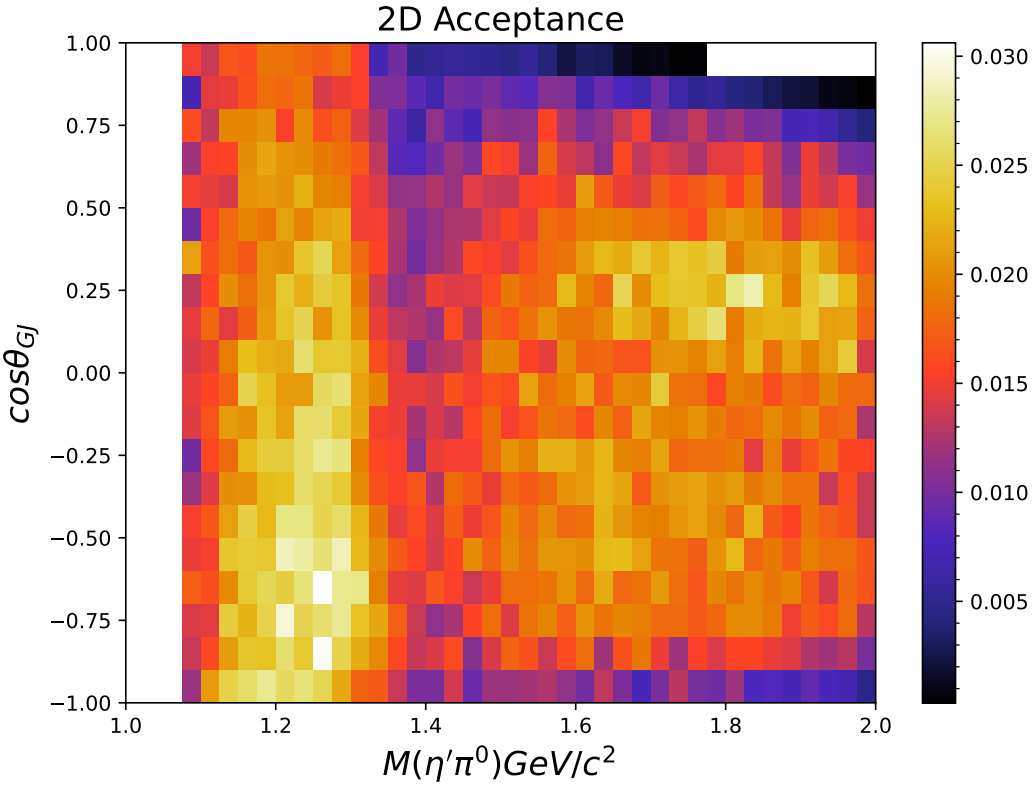

Fig. 3.34. 2D Acceptance, a significant loss of events is seen at around $1.4\,\mathrm{GeV/c^2}$ due to the ω cut

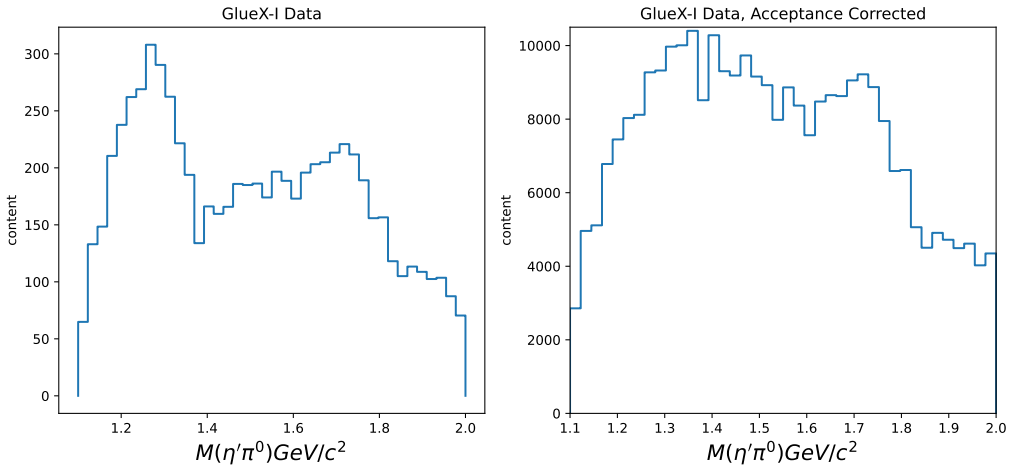

Fig. 3.35. Left : acceptance not corrected, right: acceptance corrected $\eta'\pi^0$ invariant mass distributions

3.5.4 Errors on Q-factors: δ_Q^2

Uncertainties for each q-factor were calculated from the following equation

$$\delta_Q^2 = \sum_{ij} \frac{\delta Q}{\delta Q_{par_i}} (C^{-1}_{Q_{par}})_{ij} \frac{\delta Q}{\delta Q_{par_j}} \tag{3.14}$$

where Q_{par} are the parameters. A, μ, σ are the signal parameters and a_0 and a_1 are the background parameters described earlier. $C^{-1}_{Q_{par}}$ is the covariance matrix obtained from each event's fit [6].

3.5.5 Double-Regge Processes

Apart from backgrounds discussed in previous sections, there is another type of background which requires a pure η' and a pure π^0 production but is a non-resonant mode of production. In this process, an η' and a π^0 mesons are produced in a two step exchange. A Feynmann diagram for such processes is shown in fig. 3.36. A two step t-channel process exchange could have a η' produced in an upper vertex followed

by a π^0 production in the lower vertex or the η' and π^0 can also be exchanged. Such processes are predicted to dominate higher energy region mainly above 2 GeV in the $\eta'\pi^0$ invariant mass. Our signal data sample would also have some contribution from these processes, a quantification of which was not possible for the current analysis. It would require a separate analysis along with theoretical input.

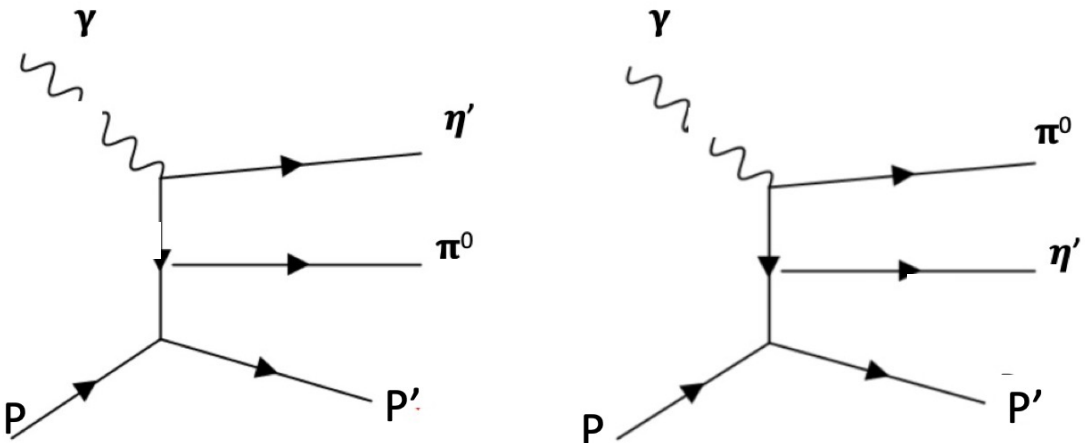

Fig. 3.36. Feynmann diagrams showing t-channel double-regge exchange processes. The η' and a π^0 is produced without a resonance being produced (left). The positions of η' and the π^0 are swapped (right).

Bibliography

[1] Peter Pauli. *Lambda (1520) measurements at the GlueX experiment*. PhD thesis, University of Glasgow, 2020.

[2] S Adhikari, CS Akondi, H Al Ghoul, A Ali, M Amaryan, EG Anassontzis, A Austregesilo, F Barbosa, J Barlow, A Barnes, et al. The gluex beamline and detector. *Nuclear Instruments and Methods in Physics Research Section A: Accelerators, Spectrometers, Detectors and Associated Equipment*, 987:164807, 2021.

[3] Paul Mattione. Least squares kinematic fitting of physics reactions (2016). https://halldweb.jlab.org/DocDB/0021/002112/005/KinematicFitting.pdf.

[4] Rebecca Barsotti and Matthew R Shepherd. Using machine learning to separate hadronic and electromagnetic interactions in the gluex forward calorimeter. *Journal of Instrumentation*, 15(05):P05021, 2020.

[5] Torbjörn Sjöstrand. The pythia event generator: Past, present and future. *Computer Physics Communications*, 246:106910, 2020.

[6] Mike Williams. Measurement of differential cross sections and spin density matrix elements along with a partial wave analysis for $\gamma p \rightarrow p\omega$ using clas at jefferson lab. *Jlab Thesis*, 2007.

CHAPTER 4

ANALYSIS PART 2 : PARTIAL WAVE ANALYSIS

4.1 Likelihood Construction and The Fitting Procedure

In order to carry out the partial wave analysis (PWA), we will use a unbinned extended maximum likelihood method for fitting individual bins of the $\eta'\pi^0$ invariant mass. Here unbinned means that the data are not binned in polar or azimuthal angular directions of the decaying η' in the $\eta'\pi^0$ rest frame or the helicity frame discussed before. The PWA presented below is using the AMPTOOLS [1] package, a C++ library written to perform an extended maximum likelihood fitting. Following the reference [1], a summary of the general principle of the likelihood fitting that is used in the current analysis is discussed below. We follow the same notation as is used in the reference [1].

Consider that $\mathbf{x}$ is a vector of dimension n that describes the kinematics of the reaction. The intensity model of our analysis that is fit to the data will be a function of $\mathbf{x}$ and will contain m parameters $\boldsymbol{\theta}$. The goal of the fit is to obtain the best estimates of the parameters $\boldsymbol{\theta}$ that maximizes the likelihood of the model to represent the data.

For a set of N independent observations $\mathbf{x}_i$, the expression for the extended likelihood as a function of the parameters $\boldsymbol{\theta}$ is given as,

$$L(\boldsymbol{\theta}) = \frac{e^{-\mu}\mu^N}{N!}\prod_{i=1}^{N} P(\mathbf{x}_\mathrm{i};\boldsymbol{\theta}) \tag{4.1}$$

where P is the n-dimensional probability density. P will be written in terms of the intensity $I(\mathbf{x};\boldsymbol{\theta})$, the explicit form of which is described in the next section. $I(\mathbf{x};\boldsymbol{\theta})$ is the model-predicted number of signal events per unit phase space. Let

$\eta(\mathbf{x})$ be the probability that an event with kinematics $\mathbf{x}$ is detected by the detector and pass all subsequent event selection criteria to make it to the final sample of N events that is used as an input to the fit. Then the total model-predicted number of observed events for some set of parameters $\boldsymbol{\theta}$ is written as,

$$\mu = \int I(\mathbf{x};\boldsymbol{\theta})\eta(\mathbf{x})d\mathbf{x} \tag{4.2}$$

The probability density function can be written as,

$$P(\mathbf{x};\boldsymbol{\theta}) = \frac{1}{\mu} I(\mathbf{x};\boldsymbol{\theta})\eta(\mathbf{x}) \tag{4.3}$$

The minimization of -2ln$L$, in practice, is much easier than maximizing the likelihood L. Using equations 4.2 and 4.3 in equation 4.1, we get

$$-2lnL(\boldsymbol{\theta}) = -2\Big(\sum_{i=1}^{N} I(\mathbf{x}_i;\boldsymbol{\theta}) - \int I(\mathbf{x};\boldsymbol{\theta})\eta(\mathbf{x})d\mathbf{x}\Big) + c_1 \tag{4.4}$$

Any dependence of the likelihood L on a quantity other than $\boldsymbol{\theta}$ is absorbed in the constant c_1. The right hand side of equation 4.4 is what is computed by the AMPTOOLS framework and is supplied to the minimizing algorithm MINUIT [2] for minimization. More details can be found in reference [1]. We need the intensity model $I(\mathbf{x};\boldsymbol{\theta})$ for the reaction $\gamma p \to \eta'\pi^0 p$ to perform the likelihood fits which is discussed next.

4.2 The Intensity Model

An intensity model developed for the reaction $\to \eta\pi^0 p$ in reference [3]. The model focuses on the reaction of the GlueX experiment where a linearly polarized photon beam is used. Since the $\eta'\pi^0$ is also a system of two pseudoscalar mesons, the model is equally valid for the reaction $\gamma p \to \eta'\pi^0 p$. Following the reference [3], a

brief summary describing the steps leading to an intensity model for the reaction $\gamma p \to \eta'\pi^0 p$ is discussed below. The same notation is used as is in the reference.

Consider the nuclear reaction

$$\vec{\gamma}(\lambda, p_\gamma)\, p(\lambda_1, p_N) \to \pi^0(p_\pi)\eta'(p_{\eta'})p(\lambda_2, p'_N)$$

Here $\lambda' s$ are the respective helicities of the particles defined in the helicity frame discussed in section 1.7. If $A_{\lambda;\lambda_1,\lambda_1}(\Omega)$ is the amplitude of the reaction, where $\Omega \to (\theta, \phi)$ are the polar and azimuthal angles of the decaying η' in the helicity frame, and Φ being the angle between the polarization plane and the production plane of the $\eta'\pi^0$, then the intensity can be described in terms of the amplitude as,

$$I(\Omega, \Phi) = \frac{d\sigma}{dt dm_{\eta'\pi^0}\, d\Omega d\Phi} = \kappa \sum_{\lambda,\lambda',\lambda_1,\lambda_2} A_{\lambda;\lambda_1,\lambda_2}(\Omega)\rho^\gamma_{\lambda\lambda'}(\Phi)A^*_{\lambda';\lambda_1,\lambda_1}(\Omega) \tag{4.5}$$

Here ρ^γ is the spin density matrix which contains the dependence on the polarization direction. This can be explicitly written as,

$$I(\Omega, \Phi) = I^0(\Omega) - P_\gamma I^1(\Omega)\cos 2\Phi - P_\gamma I^2(\Omega)\sin 2\Phi \tag{4.6}$$

the degree of linear polarization being $0 < P\gamma < 1$, further one can write individual intensity contributions as,

$$I^0(\Omega) = \frac{\kappa}{2} \sum_{\lambda,\lambda_1,\lambda_2} A_{\lambda;\lambda_1,\lambda_2}(\Omega)A^*_{\lambda;\lambda_1,\lambda_2}(\Omega) \tag{4.7}$$

$$I^1(\Omega) = \frac{\kappa}{2} \sum_{\lambda,\lambda_1,\lambda_2} A_{-\lambda;\lambda_1,\lambda_2}(\Omega)A^*_{\lambda;\lambda_1,\lambda_2}(\Omega) \tag{4.8}$$

$$I^2(\Omega) = i\frac{\kappa}{2} \sum_{\lambda,\lambda_1,\lambda_2} \lambda A_{-\lambda;\lambda_1,\lambda_2}(\Omega)A^*_{\lambda;\lambda_1,\lambda_2}(\Omega) \tag{4.9}$$

The partial wave amplitudes T^l are defined as

$$A_{\lambda;\lambda_1,\lambda_2}(\Omega) = \sum_{lm} T^l_{\lambda m;\lambda_1,\lambda_2} Y^m_l(\Omega) \tag{4.10}$$

A linear combination of the two $\lambda = \pm 1$ photon helicities can be used to change the basis set from helicity to so called reflectitivity basis as,

$$T^l_{m;\lambda,\lambda_1} = \frac{1}{2}[T^l_{+1m;\lambda,\lambda_1} - \epsilon(-1)^m T^l_{-1-m;\lambda,\lambda_1}] \tag{4.11}$$

$m = -l, ..., l$. Here $\epsilon = \pm 1$ is the reflectivity index. Parity invariance implies,

$$T^l_{m;-\lambda_1,-\lambda_2} = \epsilon(-1)^{\lambda_1-\lambda_2\ (\epsilon)} T^l_{m;\lambda_1,\lambda_2} \tag{4.12}$$

Using this one can define a set of partial waves,

$$[l]^\epsilon_{m;0} = {}^{(\epsilon)}T^l_{m;+,+} \qquad [l]^\epsilon_{m;1} = {}^{(\epsilon)}T^l_{m;+,-} \tag{4.13}$$

corresponding to nucleon non-flip and flip respectively. To generalize, $[l]^\epsilon_{m;k}$ are the complex numbers which are the partial waves we would like to extract from the fit. To emphasize $[l] = S, P, D$ are the first 3 lowest partial waves corresponding to $l = 0, 1, 2$. For each l, there are $2 \times 2 \times (2l + 1)$ complex partial waves $[l]^\epsilon_{m;k}$, with $\epsilon = \pm$, $k = 0, 1$ and $m = -l, ...l$. For example, in this notation, $[0]^+_{0;1}$ would be an S wave with a spin projection $m = 0$, positive reflectivity $\epsilon = +$ and spin flip $k = 1$ represented by $S^+_{0;1}$. Since the GlueX target is not polarized, the kinematic factor k which corresponds to the spin flip and non-flip of the nucleon is not relevant. And so we can refer to $S^+_{0;1}$ simply as S^+_0. The same notation can be extended to P and D waves as well. A complete set of partial waves can be listed as $\{S^-_0, S^+_0, P^-_{-1}, P^-_0, P^-_1, P^+_{-1}, P^+_0, P^+_1, D^-_{-2}, D^-_{-1}, D^-_0, D^-_1, D^-_{-2}, D^+_{-2}, D^+_{-1}, D^+_0, D^+_1, D^+_{-2}\}$. It is important to remember that each of these waves are complex numbers with

a real and an imaginary part, that are the fit parameters that will be varied to minimize the left hand side of equation 4.4.

To simplify the intensity further, we define the phase rotated spherical harmonics as

$$Z_l^m(\Omega, \Phi) = Y_l^m(\Omega) e^{-i\Phi} \tag{4.14}$$

where Φ is the angle between the polarization plane and the production plane of $\eta'\pi^0$. Then the intensity described in equation 4.6 can then be written as four coherent sums of nucleon spin using equations from 4.7 to equations 4.13 as,

$$I(\Omega, \Phi) = 2\kappa \sum_{\kappa} \Bigg\{ (1-P_\gamma) \Bigg| \sum_{l,m} [l]^-_{m;k} \mathrm{Re}[Z_l^m(\Omega, \Phi)] \Bigg|^2 + (1-P_\gamma) \Bigg| \sum_{l,m} [l]^+_{m;k} \mathrm{Im}[Z_l^m(\Omega, \Phi)] \Bigg|^2 +$$
$$(1+\mathrm{P}_\gamma) \Bigg| \textstyle\sum_{l,m} [l]^+_{m;k} \mathrm{Re}[Z_l^m(\Omega, \Phi)] \Bigg|^2 + (1+P_\gamma) \Bigg| \textstyle\sum_{l,m} [l]^-_{m;k} \mathrm{Im}[Z_l^m(\Omega, \Phi)] \Bigg|^2 \Bigg\} \tag{4.15}$$

The details of the derivation of this equation can be found in reference [4]. By using this intensity formula, we would fit the negative log likelihood as expressed in equation 4.4 to extract $[l]^{\pm}_{m;k}$ coefficients in the four separate coherent sums.

.

4.3 The Fit Setup

The challenging part is to choose a wave set for the partial wave analysis fits. There are three main control variables that can be varied in the input to the partial wave analysis fits. The first is the order of the wave set. We look at the past results from COMPASS [5] where the results suggest that the invariant mass of the $\eta'\pi^0$ in the window of $(1, 2)\,\mathrm{GeV/c^2}$ is dominated by the lowest 3 waves $l = 0, 1$ and 2.

Hence we use only S, P and D waves in our wave set corresponding to $l = 0, 1$ and 2. The second one is the reflectivity (ϵ). The reflectivity ϵ is the eigen value of the reflectivity operator. In the reference [3], it is discussed that in the high energy limit the amplitudes with $\epsilon = +1$ and $\epsilon = -1$ are dominated by the t-channel exchanges with naturality, $\eta = +1$ and $\eta = -1$ respectively. The naturality is defined as $\eta = P(-1)^J$ for the exchange of spin J and parity P [3]. Currently we have no information to indicate either natural or unnatural exchane dominates in our analysis. Hence we include both positive and negative reflectivities in our fits. The third one is the choice of spin projections $m = -l, ..., +l$. In the photoproduction both negative and positive values of m are allowed [6]. Only using either positive or negative spin projections would reduce the number of parameters but since both are allowed in a photon beam, that would introduce a bias in our method. Hence we allow both positive and negative spin projections and both negative and positive reflectivities in S, P and D waves in the choice of wave set for fitting.

The $\eta'\pi^0$ invariant mass is divided into 12 bins from 1 to 2 GeV/c^2. For the momentum transfer t discussed in chapter 3, we used a single bin from 0.1 to 0.7 (GeV/c)^2. 100 different fits were performed in each mass bins with random initial parameters. Out of the 100 fits, the fit with the minimum likelihood value was used to calculate the intensities in different waves.

4.4 The Fit Results

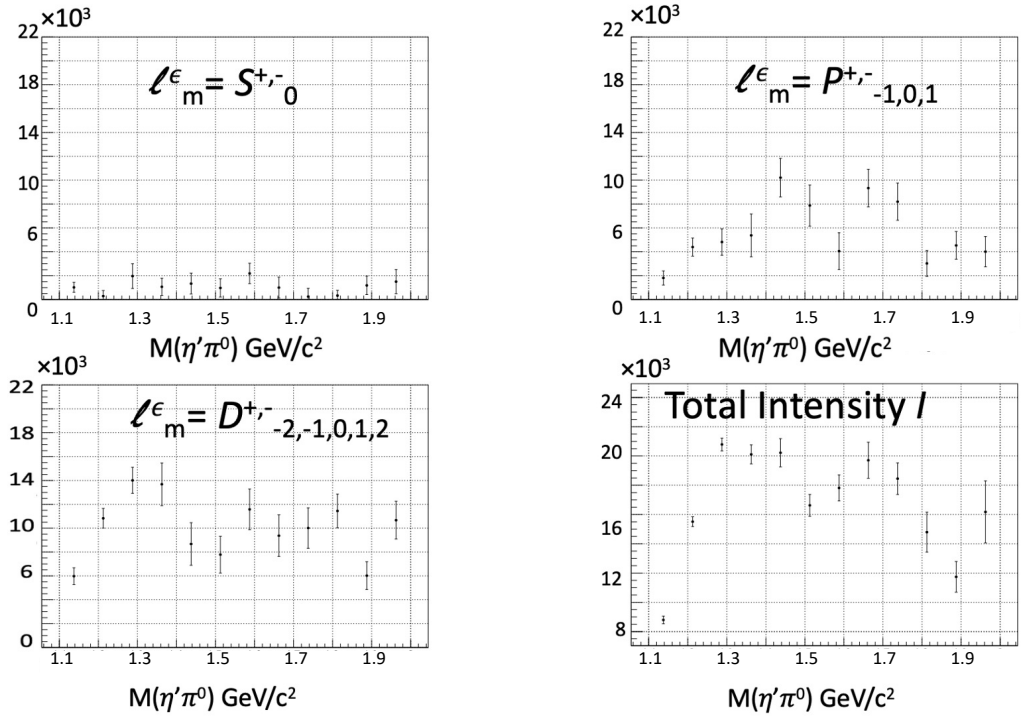

Fig. 4.1. Intensities for different waves, top left: total S-wave, top right: total P-wave, bottom left: total D-wave, bottom right: total Intensity. Each wave includes both positive and negative reflectivities.

Figure 4.1 shows the distribution of total intensities among S, P and D waves. The histograms are corrected for acceptance and errors in each mass bin are extracted from the bootstrap method described later in section 4.5. The double peak structure in the D wave could be due to $a_2(1320)$ and $a_2'(1700)$ and there could be potential $\pi_1(1600)$ evidence in the P wave but large uncertainties and ambiguities in the amplitude determination make it difficult to interpret the results as the large error bars suggest that the current statistics presents any firm conclusion to be drawn from these histograms.

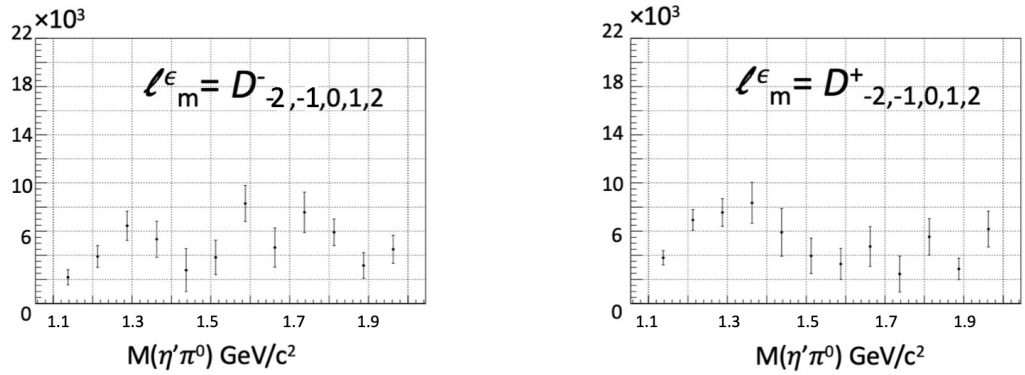

Fig. 4.2. Comparison of negative(left) and positive(right) reflectivities in total D-wave. The comparison is for studying the production mechanisms. With the current statistical uncertainty, one production mechanism dominating over the other can't be concluded.

In figure 4.2, we compare the negative and positive reflectivities in all spin projections of the D-wave. We want to learn about the production mechanism of the resonances contributing to the D wave by comparing negative and positive reflectivity contributions that correspond to the naturality of the exchanged particle. We see bin-by-bin fluctuations but there is no indication of either of these reflectivities dominating over the other.

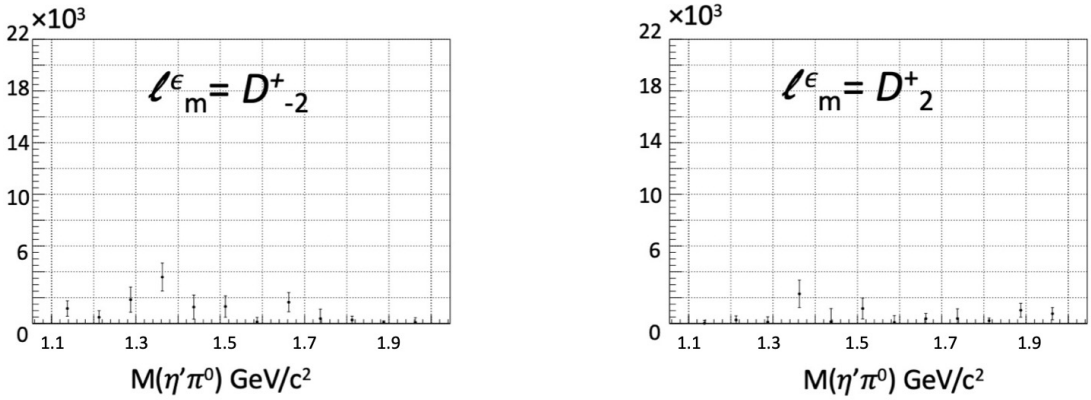

Fig. 4.3. Comparison of $m = -2$ (left) and $m = 2$ (right) spin projections of D-waves with positive reflectivities.

In figure 4.3, we compare $m = -2$ (left) vs $m = 2$(right) for D-wave in positive reflectivity. Clearly, the intensities are too low to make any conclusions.

Since the partial wave amplitudes are complex numbers, a phase difference between different amplitudes might also indicate interfering resonant states since interfering resonant states, if present, should be reflected as rapid changes in the phase difference as a function of invariant mass. Random phase differences scattered around 0 would indicate the absence of resonant states. In figure 4.4 the phase difference between the D_0^- and P_0^- (left) and D_2^- and P_0^- (right) amplitudes as a function of the $\eta'\pi^0$ invariant mass are shown. We found that the probability for a random set of phase difference data points scattered around 0 to result in a χ^2 value smaller than the one of obtained from the data point is 64%. This is a strong evidence that the experimental data points show no phase difference. For the $D_2^- - P_0^-$ phase difference, the same comparison to 0 gives a probability of a getting a smaller χ^2 for next sample is about 90% corresponding to a small probability for a potential signal. Assuming that the D-wave is dominated by a resonance like an $a_2(1320)$, its phase should be same for all spin projections m. One can then check the resemblance between the two histograms. If both phase differences are drawn from the same underlying distribution, their difference should be scattered around 0. Performing the same analysis as previously described we find a probability of 70% for a smaller χ^2 value indicating that the two data set are the same. Although the phase difference $D_2^- - P_0^-$ has a better chance of being a non-random distribution when compared to the phase difference of $D_0^- - P_0^-$, these numbers overall indicate no exotic signal in the P0 wave. It is crucial to repeat the phase difference study with increased statistics as these probabilities are highly sensitive to statistical uncertainties.

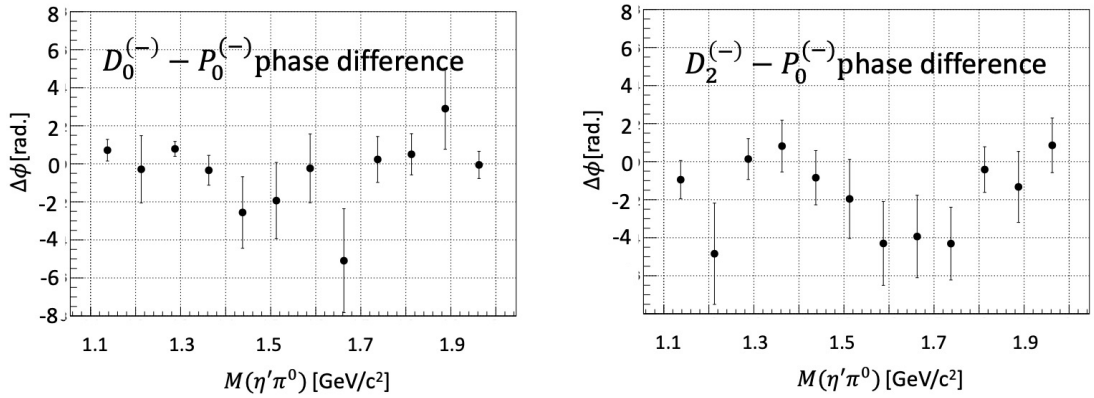

Fig. 4.4. Phase difference between D_0^- and P_0^- (left) and D_2^- and P_0^- (right) as a function of the $\eta'\pi^0$ invariant mass. If the D-wave is by a resonance (eg. $a_2(1320)$) these two data sets should be identical

4.5 Errors Estimation from Bootstrapping

The intensity uncertainty extracted from the minuit fits are not reliable. The reaosn is that the calculation assumes that the derivatives of the normalization integrals with respect to the parameters are equal to zero which is not the case as and we are calculating an intensity that depends on these parameters that were varied during the fit.

In order to correctly estimate the statistical uncertainty, we used a method called bootstrapping. In each bin of $\eta'\pi^0$ invariant mass, we resample the events from the original sample to produce the same sample size as the original sample but with repetitions allowed. So for each bootstrap sample, some of the events were repeated while some were excluded. Then using the best value of the parameters from the regular fits to initialize the bootstrap fits, in each $\eta'\pi^0$ invariant mass bin, 100 bootstrap fits were performed. From the distribution of the $\eta'\pi^0$ invariant mass of these 100 fits for each bin, we inferred a (σ) resolution, assuming the distribution

is a Gaussian. The statistical errors shown in the intensity histograms are thus extracted $\sigma's$. That means for each $\eta'\pi^0$ invariant mass bin, the values reported are the bin content $\pm\sigma$.

4.6 Fit Quality

The fitted angular distributions can be compared to the experimental angular distributions from data as a qualitative measure of the quality of fit. Figure 4.5 shows a comparison of the $cos\theta$ dependence of the decaying η' intensity in the helicity frame for data and fit. Similarly fig. 4.6 shows the azimuthal angular distributions in radians. The data points are shown with error bars and the fitted distributions are shown in green. The left histograms are for the first $\eta'\pi^0$ invariant mass bin and the right histograms are for last $\eta'\pi^0$ invariant mass bin. The histograms clearly show that the angular distributions vary as a function of the $\eta'\pi^0$ invariant mass. The error bars correspond to the statistical uncertainty in the data and demonstrate limited statistical precision.

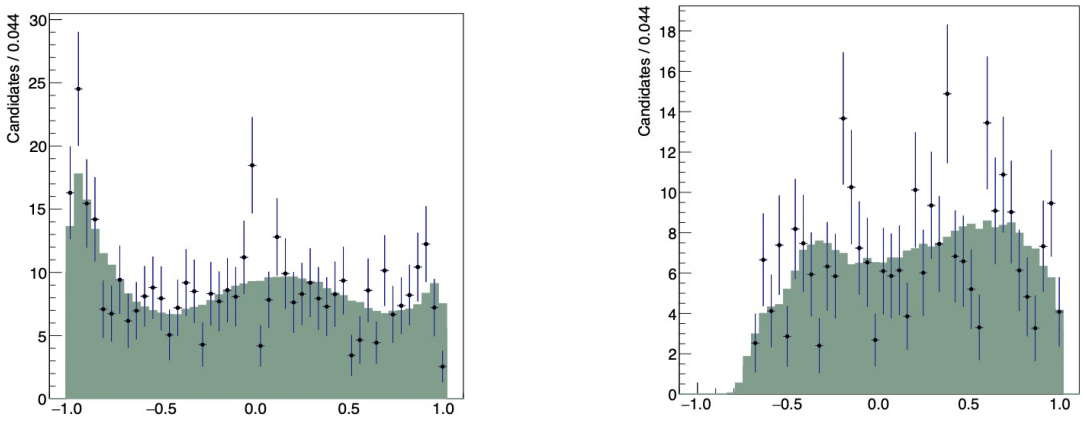

Fig. 4.5. $cos\theta$ of the decaying η' in the helicity frame for the first (left) and the last(right) $\eta'\pi^0$ invariant mass bins. The data points are indicated with error bars. The green distributions are the fitted distribution. The error bars correspond to statistical uncertainty in data and show that the statistics is small.

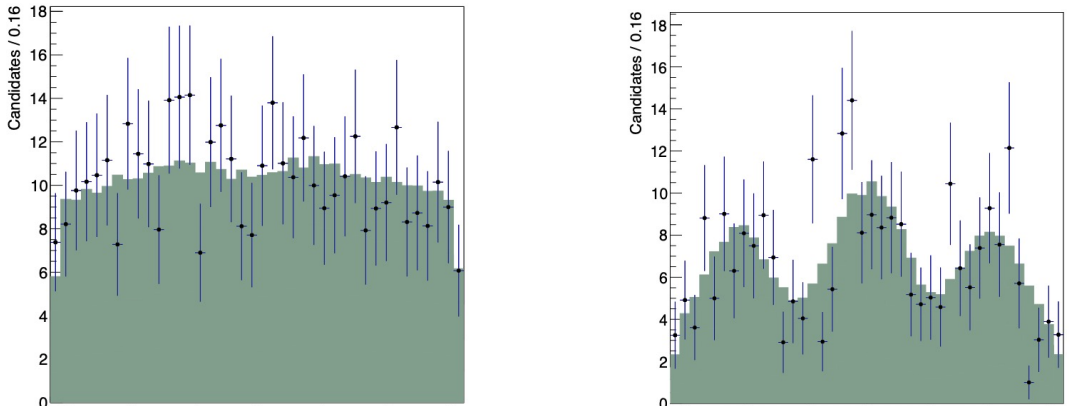

Fig. 4.6. ϕ in radians of the decaying η' in the helicity frame for the first (left) and the last(right) $\eta'\pi^0$ invariant mass bins. These histograms indicate that we are limited by statistics to evaluate the goodness of fit.

Bibliography

[1] Matthew Shepherd. Amptools user guide. https://github.com/mashephe/AmpTools/blob/master/AmpTools_User_Guide.pdf.

[2] F. James (CERN Geneva Switzerland). Minuit reference manual. https://root.cern.ch/download/minuit.pdf.

[3] Vincent Mathieu, M Albaladejo, C Fernández-Ramírez, AW Jackura, M Mikhasenko, A Pilloni, Adam P Szczepaniak, Joint Physics Analysis Center Collaboration, et al. Moments of angular distribution and beam asymmetries in $\eta\ \pi\ 0$ photoproduction at gluex. *Physical Review D*, 100(5):054017, 2019.

[4] Matthew Shepherd. Amptools implementation of polarized production. https://halldweb.jlab.org/DocDB/0040/004094/003/amptools_polarization.pdf.

[5] C Adolph, R Akhunzyanov, MG Alexeev, GD Alexeev, A Amoroso, V Andrieux, V Anosov, A Austregesilo, B Badełek, F Balestra, et al. Odd and even partial waves of $\eta\pi^-$ and $\eta'\ \pi^-$ in π^- p$\rightarrow\ \eta^{(\prime)}\ \pi^-$ p at 191 gev/c. *Physics Letters B*, 740:303–311, 2015.

[6] SU Chung and TL Trueman. Positivity conditions on the spin density matrix: A simple parametrization. *Physical Review D*, 11(3):633, 1975.

CHAPTER 5

DISCUSSIONS AND CONCLUSIONS

We analysed the $\eta'\pi^0$ via photoproduction, a part of the search for an exotic hybrid meson $\pi_1(1600)$ previously identified in pion-production. The analysed sample was taken from the GlueX Phase-I data set. The background analysis proved challenging. About 30% of the background underneath the η' peak remain unidentified and we executed a probabilistic method on an event-by-event basis for signal to background separation. The $\eta'\pi^0$ invariant mass distribution for the signal region was almost flat when the acceptance correction was applied. Only about 7000 signal events were left for a partial wave analysis in the $\eta'\pi^0$ invariant mass between 1 and 2 GeV/c^2.

A mass independent fit was done for a partial wave analysis for the extracted signal angular distributions was carried out using an intensity model developed for this channel. We found no statistically significant evidence for an exotic hybrid or any other signal in the $\eta'\pi^0$ invariant mass between 1 and 2 GeV/c^2. A comparison for the positive and negative reflectivities in the D-wave also showed no preference for one over the other. A comparison of positive and negative spin projections $m = 2$ and $m = -2$ in D-wave for the positive reflectivities was also not useful due to the lack of statistics.

An important aspect for future analysis work would be to include the double-regge processes (discussed in the section 3.5.5) in the amplitude analysis. Although the double-regge processes were predicted to dominate in a region above 2 GeV in the $\eta'\pi^0$ invariant mass, for the current analysis, we assumed such processes were neglegible during the partial wave analysis. Another important aspect is resolving the ambiguities in the amplitude fits. There can be multiple amplitude fits with the

same final likelihood values but different amplitudes. Future theory input will be important to understand these aspects for this analysis.

VITA

RUPESH DOTEL

2009-2011	B.S., Physics Tri-Chandra College Kathmandu, Nepal
2012-2013	M.S., Physics Tribuvan University Kathmandu, Nepal

PUBLICATIONS AND PRESENTATIONS

2021 American Physical Society meeting: Background study for $\gamma p \to \eta' \pi^0 p$; Virtual, April 17-20, 2021.

2020 American Physical Society DNP meeting: Analysis of the $\eta' \pi^0$ system in GlueX; Virtual, Oct 29 - Nov 1, 2020.

2019 34^{th} Hampton University Graduate Studies Program (HUGS 2019 summer school) : GlueX and exotic mesons; May 28 - June 14, 2019.

Talks on several GlueX collaboration meetings from February 2019 - present.